The Thesis committee for Jan-Michael Cabrera
certifies that this is the approved version of the following thesis:

Novel Suppression Methods in Fire Protection

APPROVED BY

SUPERVISING COMMITTEE:

Supervisor: _____
Ofodike A. Ezekoye

_____
Matthew J. Hall

Novel Suppression Methods in Fire Protection

by

Jan-Michael Cabrera, B.S.M.E.

THESIS

Presented to the Faculty of the Graduate School of

The University of Texas at Austin

in Partial Fulfillment

of the Requirements

for the Degree of

MASTER OF SCIENCE IN ENGINEERING

The University of Texas at Austin

December 2013

Dedicated to my family.

Acknowledgments

I would like to thank Professor O.A. Ezekoye for his encouragement, guidance, and support in the growth I have experienced over the past couple of years. Dr. Ezekoye's emphasis on mastering and applying the fundamental skills in heat transfer and other physical problems is something that will stay with me for the rest of my career.

I would also like to thank Dr. Kristopher Overholt for his constant support and sharing of tools necessary to tackle hard problems systematically. Dr. Overholt's passion for fire research and sharing knowledge has definitely had a huge impact on me as a person.

I would also like to thank my fellow labmates at UT Fire Research Group, Andrew Kurzawski, Austin Anderson, and Mustafa Abasi for their support and guidance through complicated topics in a number of areas outside of Thermal/Fluid Systems.

Finally I would like to acknowledge the support of Los Alamos National Laboratories for providing funding for the fire suppression activation tests, and Mudeer Habeeb and Oscar Barajas for their help throughout the process of setup and experimentation of the fire suppression system.

Novel Suppression Methods in Fire Protection

Jan-Michael Cabrera, M.S.E.
The University of Texas at Austin, 2013

Supervisor: Ofodike A. Ezekoye

The onset of fire within a compartment can pose a hazard to the occupants and the structure containing the compartment. Fire suppression systems aim to either extinguish or suppress an incipient fire before loss of life or damage to the structure can occur. The geometry and use of the compartment as well as the fuel packages within must be taken into account when choosing an appropriate fire suppression system. This thesis explores novel suppression methods inside of compartments.

Los Alamos National Laboratories came to the University of Texas Fire Research Group (UTFRG) to characterize and investigate the fire danger inside of nuclear gloveboxes. The first suppression method discussed explores activation tests of a commercial automatic fire suppression system (Fire Foe^{TM}) containing heptaflouropropane (FE-36) fire suppressant conducted within a glovebox at the UTFRG's burn structure. Temperature and time to activation data of ten tests at four different fire sizes, three 13 kW, one 20 kW, three 25 kW, and three 50 kW, was taken. Gas temperatures from experiments were compared against NIST's Fire Dynamics Simulator (FDS) gas temperatures with good agreement. The time and spatially averaged net heat flux on a virtual Fire Foe^{TM} tube from the FDS simulations were passed to a thermo-physical, semi-empirical, sub-model to predict activation with poor agreement from experimental activation times. A Bayesian parameter inference was later

run on the sub-model. While the Bayesian inference approach is able to match sub-model temperatures to experimental temperatures, some non-physical values for heat transfer coefficients and view factors were observed at the lower heat release rate fires.

Micro combustion calorimetry (MCC) was used to determine heat of combustion of glovebox glove material and cone calorimetry tests were run to find ignition time versus incident heat flux. Using standard ignition time models, effective model parameters were calibrated. Thermal characterization of the glove material showed that the heat of combustion found from MCC was within the range of heats of combustion for other non-halogenated materials found in the literature. Analysis of the time to ignition tests showed that the glove material should be modeled as thermally thick when one would expect thin behavior. This behavior was attributed to possible heat losses from the back of the glove material.

Dry water is expected to have similar suppression characteristics as water mist systems because the dry water particle sizes are on the order of water mist droplet sizes. The major benefit with dry water is the low pressures needed to drive the aerosol. An issue encountered with the dry water was flowing it in the way one would flow normal water. It was found that at low normal and shear stresses, the dry water clathrates would release the water held inside. A possible low shear delivery mechanism was discussed that avoids the ratholing effect. A continuous dry water production system was also designed. Filter loading tests were conducted to determine the quality of the dry water collected from the batch and continuous cases. It was observed that the ratio of water to silica for the continuous case reaches the batch value and is similar to results found in the literature. For the batch dry water it was observed that the particle size of the dried clathrates does vary with rotational speed of the blender and is independent of the type of water used (tap or deionized).

Table of Contents

Acknowledgments v

Abstract vi

List of Tables x

List of Figures xi

Chapter 1. Introduction: Fire Suppression in Compartments 1

Chapter 2. Fire Safety in Gloveboxes 8

2.1 Introduction . . . 8
2.2 Fire Foe Activation . . . 10
2.2.1 Test Facility . . . 11
2.2.2 Test Specimen . . . 14
2.2.3 Test Matrix . . . 14
2.2.4 Experimental Procedure . . . 16
2.2.5 Failure Model . . . 17
2.2.5.1 Fire Dynamics Simulator Glovebox Model . . . 17
2.2.5.2 Fire Foe^{TM} tube sub-model . . . 19
2.2.6 Test Observations . . . 21
2.2.6.1 Comparison of Predicted Values to Experimental Measurements . . . 21
2.2.7 Fire Foe Bayesian Parameter Inference . . . 51
2.3 Glove Experiments . . . 58
2.3.1 Experimentation . . . 58
2.3.1.1 Micro Combustion Calorimetry . . . 58
2.3.1.2 Time to Ignition . . . 59
2.3.2 Ignition Model . . . 61
2.3.2.1 Model Equations . . . 61
2.3.3 Results . . . 62
2.3.3.1 Micro Combustion Calorimetry . . . 62

2.3.3.2 Time to ignition 63
2.3.3.3 Thick Ignition Model Calibration 63
2.4 Conclusions 64

Chapter 3. Dry Water: Delivery for Fire Suppression 67
3.1 Introduction 67
3.2 Dry Water Delivery Prototypes 67
3.3 Development of a Continuous Dry Water Production System 75
3.3.1 Components and component characterization 75
3.4 A Framework for Dry Water Characterization 88
3.4.1 Physical Characterization of the Dry Water 88
3.4.2 Micrographs 91
3.4.3 Histograms 94
3.5 Conclusions 97

Chapter 4. Conclusion and Future Work 101

Appendix A. Scoping Water Mist Tests 103
A.1 Water Mist 103

Bibliography 107

Vita 112

List of Tables

2.1 Test matrix for glovebox experiments 16
2.2 Thermal properties of FDS materials 18
2.3 Nylon yield strength as a function of temperature 21
2.4 Fire Foe^{TM} activations time and associated HGL temperatures 22
2.5 Time and spatially averaged net heat flux to suppression system . . . 45
2.6 Convection model calibration inputs 54
2.7 Conduction model calibration inputs 54
2.8 Bayesian parameter inference results for the outside heat transfer coefficient, inside heat transfer coefficient, and view factor for the convection cases 55
2.9 Bayesian parameter inference results for the outside heat transfer coefficient and view factor for the conduction cases 55
2.10 Model Results 57
2.11 Test matrix and sample properties for time to ignition tests 59
2.12 Micro combustion calorimetry tests and results 62
2.13 Ignition test results 63
2.14 Model calibration inputs 64
2.15 Model calibration results 66

3.1 Geometry of cyclone separator of D=5 cm 78
3.2 Dry water densities for various testing conditions 88
3.3 Filter loading mass loss for continuous case at 19,500 RPM 91
3.4 Conversion factors from pixels to micrometers 96
3.5 Dry water particle size distributions for deionized and tap water . . . 99
3.6 Modes of the particle size distributions for deionized and tap water . 100

List of Figures

1.1 Stages of fire growth inside of a compartment, adapted from [1] . . . 2
1.2 Fire extinguishment and suppression within a compartment, adapted from [1] . . . 3

2.1 Glovebox provided by LANL for suppression system activation tests . 12
2.2 LANL glovebox dimensions . . . 12
2.3 LANL glovebox thermocouple locations front view . . . 13
2.4 LANL glovebox thermocouple locations top view . . . 13
2.5 Charged Fire Foe^{TM} tube . . . 14
2.6 FDS model of LANL glovebox . . . 25
2.7 Simple heat transfer model to the Fire Foe^{TM} tube . . . 26
2.8 Approximation for the constant volume pressure increase of the fire suppressant . . . 26
2.9 Force balance on a thin walled tube . . . 27
2.10 Experimental suppression system temperatures for the 13 kW, 20 kW, and 50 kW cases . . . 27
2.11 Flame heights for 25 kW Fire Foe^{TM} activation test . . . 28
2.12 Temperatures for Fire Foe^{TM} activation tests, 13 kW test 1 . . . 30
2.13 Temperatures for Fire Foe^{TM} activation tests, 13 kW test 2 . . . 31
2.14 Temperatures for Fire Foe^{TM} activation tests, 13 kW test 3 . . . 33
2.15 Temperatures for Fire Foe^{TM} activation tests, 20 kW test 1 . . . 34
2.16 Temperatures for Fire Foe^{TM} activation tests, 25 kW test 1 . . . 36
2.17 Temperatures for Fire Foe^{TM} activation tests, 25 kW test 2 . . . 37
2.18 Temperatures for Fire Foe^{TM} activation tests, 25 kW test 3 . . . 38
2.19 Temperatures for Fire Foe^{TM} activation tests, 50 kW test 1 . . . 40
2.20 Temperatures for Fire Foe^{TM} activation tests, 50 kW test 2 . . . 41
2.21 Temperatures for Fire Foe^{TM} activation tests, 50 kW test 3 . . . 43
2.22 Fire Foe^{TM} temperatures for all tests . . . 44
2.23 Net heat flux from FDS to the Fire Foe^{TM} tube for 13 kW (top left), 20 kW (top right), 25 kW (bottom left), and 50 kW (bottom right) cases 46

2.24 Sub-model Fire Foe™ tube wall and fluid temperatures for 13 kW (top left), 20 kW (top right), 25 kW (bottom left), and 50 kW (bottom right) cases 47
2.25 Sub-model fluid pressures for 13 kW (top left), 20 kW (top right), 25 kW (bottom left), and 50 kW (bottom right) cases 49
2.26 Sub-model hoop (solid) and yield (dashed) stresses for 13 kW (top left), 20 kW (top right), 25 kW (bottom left), and 50 kW (bottom right) cases 50
2.27 Fire Foe™ activation times. 50
2.28 Experimental and Model Fire Foe™ activations time vs. fire size . . 51
2.29 Spatially averaged top thermocouple temperatures from experiment and FDS 53
2.30 Ignition test samples. From top to bottom: untested, 60 kW no ignition, 60 kW after ignition 60
2.31 UTFRG Mass loss calorimeter 61
2.32 Best fit to thick ignition for data observed 65

3.1 A syringe was first used to attempt to flow dry water. 68
3.2 Schematic of a plunger used to attempt to deliver dry water 69
3.3 Schematic of using a vibrating motor to deliver dry water 69
3.4 Schematic of a rolling, agitating cage used to deliver dry water 70
3.5 Schematic of an apparatus used to fluidize dry water 71
3.6 Schematic of dry water delivery mechanism using a rigid container . . 72
3.7 The ratholing effect causes the air flow to short circuit 73
3.8 Schematic of the attempt to flow dry water using a flexible membrane 74
3.9 Schematic of a successful dry water delivery mechanism 74
3.10 Blender with quarter inch outer diameter pipe fittings 76
3.11 Bag used to measure the ratio of air to dry water 77
3.12 Schematic of cyclone separator 77
3.13 Cyclone geometry, taken from [2] 78
3.14 Pipe fittings for cyclone separator 78
3.15 Modified blender which allows water and silica to flow into it 79
3.16 Schematic of water reservoir used to flow water into the blender . . . 79
3.17 A syringe was first proposed as a means to deliver silica to the blender. 80
3.18 A rotating circular brush was originally used to fluidize silica. 81
3.19 Continuous dry water setup with the agitating seeder 81
3.20 Schematic of a percolating seeder where air flows into a bed of silica for fluidization 82

3.21 Seeder characterization 83
3.22 Schematic of blender with variable transformer 84
3.23 Rotational position of blender and strobe frequency 85
3.24 Rotational speed of blender plotted versus the setting on the variable transformer 86
3.25 Continuous dry water setup 87
3.26 Cyclone setup for collecting dry water via a laboratory filter for the batch (left) and continuous (right) cases 89
3.27 Silica aglomerates at 4x magnification 92
3.28 Batch dry water produced at a blender speed of (a) 12,500 RPM and (b) 19,500 RPM at 4x magnification 93
3.29 Traced particle, in yellow, for measuring purposes. Batch dry water made from tap water at 12,500 RPM 94
3.30 Evaporating dry water made at 19,500 RPM at 10x magnification, top at 0.0 s, middle at 0.7 s, bottom at 1.4 s. 95
3.31 Particle size distribution of silica agglomerates 97

A.1 Water mist setup 104
A.2 Mass loss of 6 g of 7 cm diameter heptane pool fire burning freely . . 105
A.3 Water mist experimental temperatures for 100 psi pressure. Vertical line indicates activation of water mist 106

Chapter 1

Introduction: Fire Suppression in Compartments

A compartment fire can be described as having three different phases, shown schematically in Figure 1.1. The first phase is fire growth from an incipient fire, in which the fire is not immediately influenced by its being inside of an enclosure, to the second phase where the fire has reached a maximum, fully developed state. The maximum fire can be either fuel controlled (well ventilated) or ventilation limited. Following the maximum fire size is a cooling phase in which all the fuel has been consumed [1]. The section that is between the incipient fire and maximum fire size is known as flashover. The transition through flashover, which usually progresses to involving all the fuel in the compartment, also marks a difference between the fuel controlled fire and the ventilation limited fire. Thomas describes flashover in compartments being attributed to an unstable fuel controlled regime or a kind of thermal instability [3]. Early work by Thomas et al. involved characterization of fuel elements in the compartment such as wooden cribs before looking at global compartmental effects of the fire. Thomas et al. then looked at the quasi-steady fully developed fire within the compartment [4]. Bullen and Thomas were some of the first to look at burning characteristics of non-cellulosic materials including ethanol, polymethyl methacrylate (PMMA), and polyethylene (PE) within fire compartments [5].

The onset of fire within a compartment can pose a hazard to the occupants and the structure containing the compartment. Fire suppression systems aim to either extinguish or suppress an incipient fire before loss of life or damage to the structure

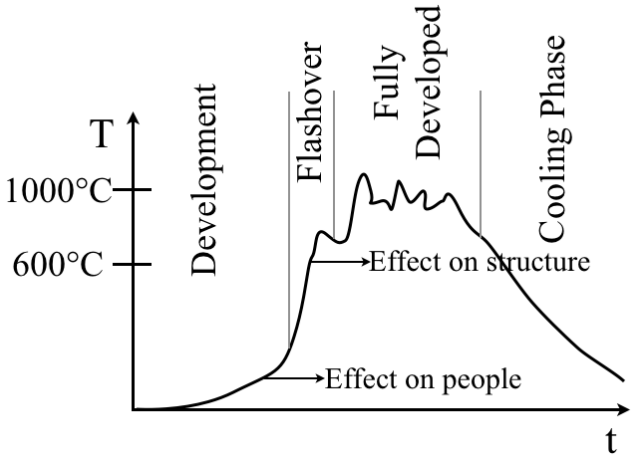

Figure 1.1: Stages of fire growth inside of a compartment, adapted from [1]

can occur, Figure 1.2. The geometry and use of the compartment as well as the fuel packages within must be taken into account when choosing an appropriate fire suppression system. A fire classification specified by NFPA 10 was developed that groups common fuel packages into a specific class [6]. There are four common classes including type A, B, C and D classes. Class A fires are ordinary cellulosic combustible materials such as paper, wood, fabrics, rubber, etc. Class B fires involve flammable liquids and gases. Class C fires involve live electrical equipment such as motors and generators. Class D fires include combustion of combustible metals including magnesium, sodium, etc.

Many compartments rely on an automatic fire suppression system that will activate without an operator in contrast to manned firefighting tactics. For many types of fires, water would be an ideal candidate for fire suppression due to it's high heat capacity, low cost, and availability. Water is, however, most ideal for only class A type fires. The most common way to deliver water automatically is through a sprinkler type system. There are different sprinkler systems that are used in compartment fires

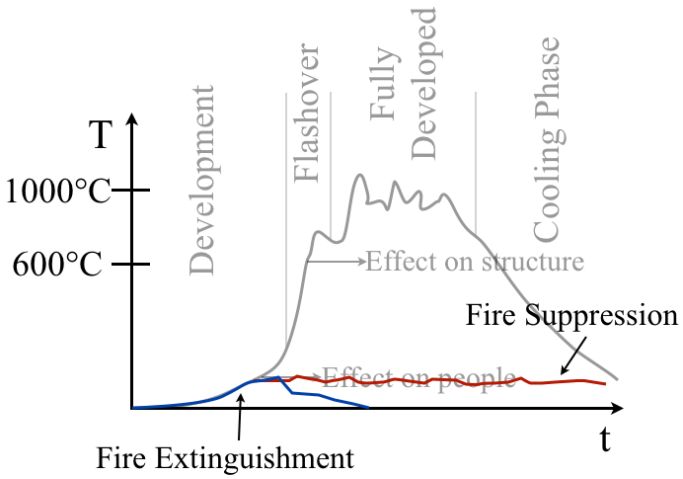

Figure 1.2: Fire extinguishment and suppression within a compartment, adapted from [1]

which include wet pipe, dry pipe, deluge, and preaction systems. Wet pipe systems are the most common and usually contain a system of sprinkler heads with fused elements which hold back pressurized water until a particular fused element degrades due to a source of heat. A dry pipe system is similar to a wet pipe system however an inert gas is used to keep water away from the fused element and piping in the vicinity of the sprinkler head. Dry pipe systems are generally used in environments in which the water in the pipe in the vicinity of the sprinkler head could possibly freeze. A deluge system relies on an active detector to detect a fire within a compartment. Should a fire be detected, all of the sprinklers are simultaneously activated extinguishing or suppressing the fire. Preaction systems are similar to deluge systems in that an active detector is used to detect a fire. Preaction systems are generally used where there is concern for accidental discharge in compartments housing computer and server racks, rare items as one would find in a museum, etc [7].

Other fire suppression systems are available to suppress fires where water cannot be used. These systems include foaming fire suppression systems, halogenated

agents, and clean fire suppressant agents meant to replace halogenated agents. Foam fire suppression systems are ideal for combating class B type fires when compared to sprinklers. The density of water does not make for a good suppressant of the less dense hydrocarbon fuels. Low density fire suppressing foams, on the other hand, will produce a film atop the liquid hydrocarbon fuel smothering the fire. Foaming fire suppressants are generally created with aerated water containing an amount of protein or surfactant to stabilize the formation of bubbles. Halogenated agents or chlorofluorocarbons (CFCs) showed promise as a fire suppression technology especially in combating class C type fires where a non-conductive fire suppressant was needed. In Jan of 1994 the Montreal Protocol declared that production of these agents should cease because of the stratospheric ozone layer depletion issue [8]. Halogenated agents were generally used as a total flooding agent. So-called "clean agents" are Halon replacement fire suppression agents. These clean fire suppression agents vaporize readily at atmospheric pressures and do not leave behind any residues. Clean agents are also non-conductive and use nitrogen super pressurization in most applications. Like the Halon forerunners, clean agents are also used as a total flooding agent and are ideal for extinguishing class C fires [7].

Water mist suppression systems are another type of suppression system. Water mist suppression technologies include sprays for which 99% of the water droplets diameter size distribution is less than 1000 µm in size. Interest in water mist suppression systems has lately increased because of the ban of production of halogenated suppression agents. The largest obstacle in using water mist systems is the high pressures needed to create the small droplets. NFPA 750 describes different kinds of water mist systems depending on the operating pressure [9]. Low pressure systems operate below 12.0 bar (175 psi), intermediate systems are between 12.0 bar and 34.0 bar (175 psi and 500 psi), high pressure systems operate at pressures above

34.0 bar (500 psi). Water mist systems are best applied to type A fires but can also suppress type B fires. Suppression mechanisms include gas phase cooling, oxygen displacement, fuel cooling, and radiation attenuation [10]. The radiation attenuation of water mist has been explored by authors such as Ravigururajan and Beltran [11] as well as Coppalle [12]. According to their models, maximum attenuation is achieved when the droplet size is on the order of the wavelength of the emitted radiation. While smaller droplets are better at attenuation of radiation and have a larger surface area than larger droplets, smaller droplets are more likely to be affected by the buoyant plume created by the fire. Fire protection with water mist is also sensitive to spray characteristics, spray direction, and physical arrangement of obstructions. Water mist systems will perform well in enclosures due to oxygen displacement, upon evaporating the water droplets will expand three orders of magnitude. This means that in compartments even low-momentum sprays can suppress obstructed fires. For more information on water mist systems, Liu and Kim give an excellent review [13].

Fire suppression systems are not limited to those described above. New technologies are continuing to be developed in an attempt to advance conventional suppression tactics. Adiga et al. explore a low momentum ultra fine mist as a possible total flooding agent. These ultra fine mists, produced by NanoMist®, have particle sizes that are less than 10 µm. This low momentum dense fog is not discharged through nozzles but is pumped into the bottom of a fire compartment at velocities of approximately 1 m/s. The buoyant flame and product plume is meant to entrain this low momentum fog, cool the flame sheet, displace oxygen, and put out the fire. In the Adiga et al. study this was done successfully in all fire suppression tests, however suppression times were greater than 5 min [14]. Another new suppression system utilizes an ignitable solid pellet that produces aerosolized potassium nitrate. The aerosolized potassium nitrate disrupts the combustion process by scavenging flame

radicals, extinguishing the fire [15].

A potential alternative to water mist and other fine mist generating systems for fire suppression is dry water. Allan was the first to create dry water in the 1970s [16]. Generally made in a batch process, it can be considered an inverse foam in which water droplets are encapsulated by hydrophobic fumed silica. The ratio of water to hydrophobic fumed silica was generally above 1:9 with reported ratios as high as 1:29 (90% and 97% by mass water, respectively) [17] . These encapsulations, or clathrates, prevent droplet coalescence and gives the resultant product a powder-like appearance. Reported blending speeds for creating dry water range from 12,000 RPM to 25,000 RPM [17–19]. Forny et al. produced dry water by high shear mixing in a blender at speeds varying from 4,000 RPM to 25,000 RPM and in a low shear planetary mixer. Forny also found that blending at speeds below 12,000 RPM did not produce dry water. Two conditions must be met for dry water formation. The first being that the bulk water should be in droplet form, and the second being that the silica must have the opportunity to encapsulate the water droplets [17]. Batches made by the authors varied from 20 g of dry water up to 2 kg using a low shear planetary mixer [17, 18, 20]. Binks et al. found that the stability of dry water was dependent on the contact angle between the fluid and the silica particles. At low contact angles, the resultant blended water-silica mixture forms an aerated foam. At high contact angles normal powder-like dry water is formed [19]. Mean dry water particle sizes have been reported to be 50 µm by Carter et al., and up to 112 µm by Forny et al. [17,18]. The reported values for dry water mean diameters are below the water mist designation of 1000 µm [9]. Taylon and Berberoglu performed a numerical study of radiation transport in a cloud of dry water. Radiation attenuation was looked at for particles ranging in 25 µm to 75 µm. It was found that the core size and volume fraction of the dry water were important to radiation attenuation with the

smallest particle sizes performing the best [20]. Dry water has the potential to have the same fire suppression characteristics of water mist systems. The small particle diameters with the advantage that the dry water can be flowed like a powder at much lower pressures when compared to conventional water mist systems makes it an ideal candidate for fire suppression.

The current work discusses use and development of two relatively unconventional fire suppression systems. Chapter 2 describes suppression experiments inside of gloveboxes (an enclosure designed to protect personnel from the hazardous materials they are working with) using a commercial fire suppression system known as Fire Foe^{TM} developed by Quickfire^{TM} technologies. Suppression tests were done at varying fire heat release rates inside of an instrumented glovebox. A computational fluid dynamics code, Fire Dynamics Simulator (FDS), was then used to describe the thermal environment around the fire protection system. Heat flux data taken from FDS was transferred to a semi-empirical thermo-physical sub-model that described activation of the Fire Foe^{TM}. Glovebox glove material thermo-physical characterization and degradation experiments were also conducted. Chapter 3 describes how a dry water delivery system was developed and the thought process used to develop a continuous dry water production system.

Chapter 2

Fire Safety in Gloveboxes

2.1 Introduction

When working with hazardous materials and chemicals, a level of safety measures must be put into place. In many testing and manufacturing communities it is common to use an apparatus such as a glovebox to ensure the safety of personal working with hazardous chemicals. The integrity of the glovebox comes into question under certain accidental conditions and natural disasters including earthquakes and fires. The increasing complexity of material manufacturing processes in turn makes the need for more complex gloveboxes. Bartlett reports on the evolution of glovebox design and complexity over the past half century. He notes that gloveboxes are continuing to be used to aid in the production of lithium batteries, film batteries, photo-voltaic cells, and others [21]. Recently, the thermal runaway hazard of large lithium-ion batteries has come into view. Hammami et al. comment on what could happen should the 10-50 nanometer protective coating on electrodes be destroyed [22]. Lithium-ion and other materials pose fire risks and for this reason adequate suppression systems must be put into place inside of gloveboxes.

In the past half century there have been many accidents that occured within these gloveboxes. Factory Mutual prepared a report that presented many issues concerning the risk of fire in gloveboxes and investigated twenty four fires and nineteen explosions involved in gloveboxes from 1956 to 1965. Total losses due to damages and contamination clean up efforts were reported at $1,232,000 ($8.5 million in 2012

dollars). They also reported that should a fire occur in a glovebox, soot from the combustion products can clog the filter causing the pressure in the glovebox to go from negative to positive. This switch in pressure could lead to transport of contaminants outside of the glovebox [23]. It is important that safety measures be put into place in order to address similar events that could occur in the future.

While water is widely used as a fire suppressing agent there are some concerns in using water in certain conditions inside of gloveboxes. Panesko reports a concern for using water based fire suppression systems inside glovebox environments. Experiments were conducted on the mobility of plutonium by water. It was found that water can potentially transport plutonium powder and other compounds out of gloveboxes and into areas such as sump tanks. This poses a potential contamination hazard [24]. In the past suppression schemes sometimes use chemical suppressants such as Halon suppression systems. Hill reports on an automatic fire extinguisher using extinguishing agent Halon 1301 [25]. Halon has been phased out due to its potential to deplete ozone [26]. New chemical agents such as heptaflouropropane (FE-36) have since been introduced. These chemicals extinguish fire by physical cooling of the flame region, cooling of the solid fuel, and chemical reactions that take out key atoms and radicals. Chow et al. comment on the necessity of studying the chemical reactions that take place at the flame sheet during use of clean agents, specifically FE-36 [27].

As new fire suppression technologies emerge it becomes useful to create models to predict the characteristics of these technologies. In these models, representing the correct heat and mass transfer mechanisms inside the system becomes important. Fire Accident (FIRAC) is an early computational model based on the lumped-parameter method developed by the Nuclear Regulatory Committee (NRC). It deals with the heat and mass transport of fire induced flows in ventilation systems of nuclear testing

facilities. Burkett et al. couple the FIRAC code with a zone compartment model, FIRIN. A detailed example of fire propagation in a nuclear facility is clearly carried out in their paper [28].

This chapter presents a discussion of ten Fire Foe^{TM} Automatic Fire Extinguishers developed by QuickFire Fire Suppression Technology that were tested at The University of Texas Fire Research Group (UTFRG) burn structure. A computational fluid dynamics model (CFD) model of the experimental system was created using NIST's Fire Dynamics Simulator (FDS). A sub-grid, thermo-physical, semi-empirical model for failure of the Fire Foe^{TM} tube was coupled with the FDS model. Experimental gas temperatures and FDS temperatures are compared and experimental activation times are compared to the sub-grid model activation times. Following testing of the suppression system, the integrity of glovebox gloves was also tested and physically characterized.

2.2 Fire Foe Activation

Los Alamos National Laboratories came UTFRG to characterize and investigate the fire risks associated with nuclear gloveboxes. UTFRG began work on glass break experiments in which a potential fire inside of a glovebox could break the glass viewing windows due to thermal stresses. Small scale tests of a proposed fire suppression system, Fire Foe^{TM} developed by Quickfire^{TM} technologies, were also done. LANL wanted to ensure that this fire suppression system would activate before the glovebox could be breached by thermal stresses in the glass or degradation of what could be the weakest component, the glovebox gloves. Following these small scale experiments, full scale experiments were conducted by UTFRG at J.J. Pickle Research Campus at the University of Texas at Austin. The following sections describe

in detail the suppression tests conducted.

2.2.1 Test Facility

Fire Foe^{TM} activation tests were conducted within a glovebox, Figure 2.1, provided by LANL at the UTFRG's burn structure, which is located at the J.J. Pickle Research Campus at The University of Texas at Austin (UT Austin). The glovebox dimensions were 0.91 m by 0.71 m by 0.94 m. The glovebox walls were constructed with stainless steel, and there were viewing windows located on the front and top. An electric fan/blower (Ametek Model 116520-50) was used to provide a volumetric flow rate of air at 0.011 m^3/s (1 air change per minute) into the glovebox. The inlet ventilation orifice for the blower was located on the rear wall of the glovebox and had a diameter of 1.25 cm. The exhaust vent was located on top of the glovebox and had a diameter of 20 cm. To minimize flow disturbance of the flame an obstruction constructed of a gypsum board panel measuring 14 cm by 21 cm was located 4 cm from the inlet ventilation hole. The gloveports of the glovebox were also obstructed using a gypsum board panel. The fire source was a propane sand burner in the center of the glovebox with dimensions of 0.3 m by 0.3 m. The sand within the burner was level with the bottom of the glovebox. Fuel was delivered to the sand burner from a propane tank located outside of the burn structure. A variable area flowmeter (Cole-Parmer) with a scale ranging from 10 LPM to 100 LPM was used to control the fuel flow rate of propane to the sand burner. A schematic of the glovebox with it's dimensions is shown in Figure 2.2.

Five thermocouple trees were placed in the glovebox as shown in Figs. 2.3 and 2.4. Thermocouple trees A, B, C, and D each contained three thermocouples at heights of 0.34 m, 0.64 m, and 0.94 m. The centerline tree contained six thermocouples at heights of 0.18 m, 0.34 m, 0.49 m, 0.64 m, 0.79 m, and 0.94 m. The

Figure 2.1: Glovebox provided by LANL for suppression system activation tests

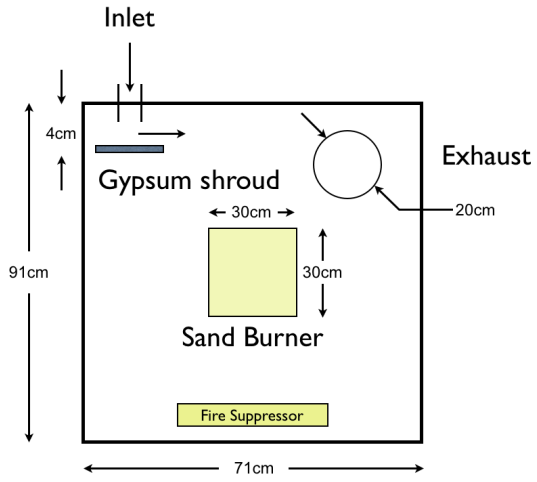

Figure 2.2: LANL glovebox dimensions

centerline thermocouples were nominally centered above the burner. An additional five thermocouples were placed on the Fire Foe™ to measure its surface temperature. The measurements were recorded using a National Instruments USB-6225 M-series Multifunction data acquisition system. A digital recording system was used to record video of the Fire Foe™ activation tests.

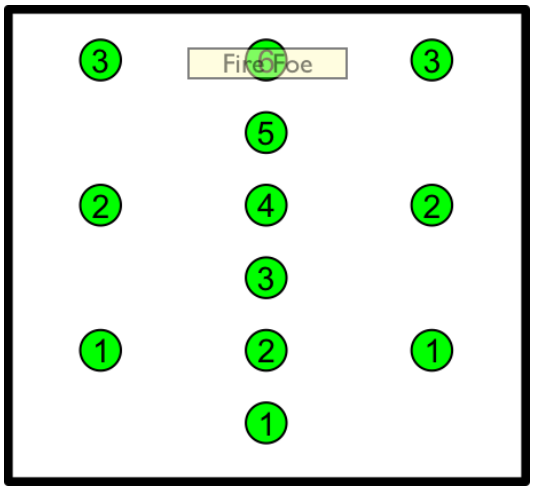

Figure 2.3: LANL glovebox thermocouple locations front view

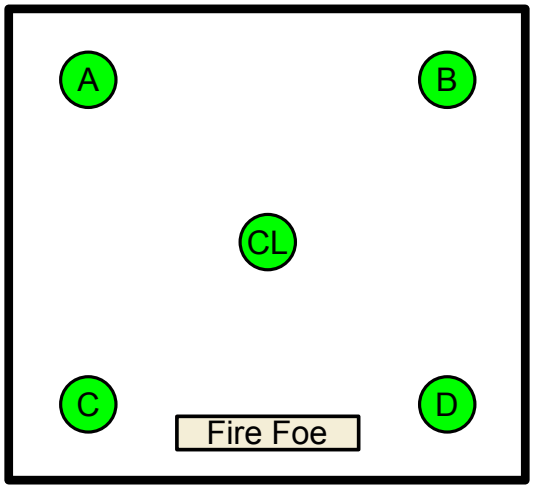

Figure 2.4: LANL glovebox thermocouple locations top view

2.2.2 Test Specimen

Ten Fire Foe^{TM} Automatic Fire Extinguishers, developed by QuickFire Fire Suppression Technology, were tested at UTFRG's burn structure. Per the manufacturer's specifications, Fire Foe^{TM} tubes of different lengths are available to best protect compartments of different sizes. The Fire Foe^{TM} model FT 30 was used in these tests, as shown in Fig. 2.5 [29]. The manufacturer states that this particular tube length is able to protect a maximum volume of 8.5 m^3. For comparison, the volume of the LANL glovebox was approximately 0.6 m^3. The system is comprised of a Nylon 6,6 tube of length 28 cm and diameter 3.8 cm that contains Envirogel^{TM} fire suppression agent. The Envirogel^{TM} suppressant agent is composed of 70% by volume FE-36 and 30% by volume sodium bicarbonate and charged with a small amount of nitrogen to 690 kPa (100 psi). The weight of each FT 30 tube is approximately 0.77 kg.

For each of the ten tests the Fire Foe^{TM} was located in the top region of the glovebox 2.5 cm from the front wall, 2.5 cm from the ceiling, and centered between the glove ports, Figures 2.3 and 2.4.

Figure 2.5: Charged Fire Foe^{TM} tube

2.2.3 Test Matrix

A total of ten tests were performed: three 13 kW fire tests, one 20 kW fire test, three 25 kW fire tests, and three 50 kW fire tests. Table 2.1 shows the test

matrix for the full-scale glovebox fire tests, their corresponding propane flow rates, and their corresponding global equivalence ratios. The expected HRR uncertainty was approximately 3.7 kW with an uncertainty of 2 LPM in propane flow rate. A global adiabatic flame temperature can then be described by

$$T_{AD} = T_0 + \frac{\dot{m}_f \Delta h_c}{\dot{m}_T c_p} \tag{2.1}$$

where T_{AD} is the adiabatic flame temperature, T_0 is the initial temperature of the products, $\dot{m}_f$ is the uncertainty in the mass flow rate of propane, Δh_c is the heat of combustion of propane, $\dot{m}_T$ is the total mass flow into the compartment, and c_p is the constant pressure specific heat of air. The uncertainty in the temperature can then be described by

$$dT_{AD} = \frac{\rho_{propane} \Delta h_c}{\dot{m}_T c_p} d\dot{V}_{propane} \tag{2.2}$$

where dT_{AD} is the uncertainty in the temperature, $\rho_{propane}$ is the density of propane, and $d\dot{V}_{propane}$ is the uncertainty in propane flow rate. dT_{AD} for the 2 LPM uncertainty in propane flow was found to be 282 °C. This gives a measure of the maximum uncertainty expected from the experimental conditions.

For the 50 kW tests it is expected that the glovebox will go underventilated because these tests were globally rich. An example from NUREG 1934 ventilation effects was reworked to find the time to oxygen depletion in the glovebox for the 50 kW case and was calculated to be 260 s, well after suppression system activation [30]. The experimental procedure used for testing of the Fire Foe™ suppression system is outlined in the next section.

Table 2.1: Test matrix for glovebox experiments

Fire Size	Number of Tests	Propane Flow Rate (LPM)	$\phi_{eq,global}$
13 kW	3	12 ± 2	0.29
20 kW	1	16 ± 2	0.38
25 kW	3	23 ± 2	0.53
50 kW	3	46 ± 2	1.11

2.2.4 Experimental Procedure

Before testing of the suppression system, the right side wall of the glovebox was removed to allow placement of the Fire Foe^{TM} tube. With the tube in place, thermocouples were attached to the outer tube wall for all cases except the 25 kW cases. The wall was replaced and the blower was powered on to provide air flow into the glovebox. At the same time a spark igniter generating 10 kV at 80 Hz was turned on [31]. The spark ignitor was used only for the 13 kW, 20 kW, and 25 kW cases. For the 50 kW cases, small candles were fixed to the side of the sand burner and lit just after activation of the blower. The data acquisition system was also started around the time the igniter was activated. With the igniters in place, the burn structure was cleared of people and the okay was given to flow propane into the glovebox at a specified rate. Temperature data was taken up to 5 min after activation of the suppression system. The suppressant successfully extinguished the fire immediately after activation for all tests.

The glovebox was allowed to cool for about 10 min after activation of the Fire Foe^{TM} tube before the side wall was again removed. When the Fire Foe^{TM} activated the fire suppressant agent coated the entirety of the space. The excess sodium bicarbonate within the glovebox was vacuumed out after each test before a new Fire Foe^{TM} was installed.

2.2.5 Failure Model

One of the objectives of this project was to develop an approach for predicting the activation time of the Fire Foe^{TM} system. The Fire Foe^{TM} activation process is essentially a thermomechanical failure. Heat transfer from the fire weakens the tube's nylon enclosure and thermodynamically expands the working fluid within it. This is a complex failure process that requires multiphysics and multiscale analyses to issue a reliable prediction of failure time. The prediction first requires a model to estimate the thermal environment produced by a fire of a specified heat release rate. Reliably predicting compartment fire thermal properties is an ongoing area of research. CFD codes are more routinely being used to issue such predictions. As the thermal environment enveloping the Fire Foe^{TM} tube evolves, it is necessary to couple the environmental changes to the tube's internal modifications. A sub-model is used with heat transfer physics and a simple, semi-empirical mechanical failure law to describe the failure process. In the next section the CFD model is discussed.

2.2.5.1 Fire Dynamics Simulator Glovebox Model

This CFD analysis was performed with Fire Dynamics Simulator (FDS) version 6.0.0, SVN revision number 12521 [32]. The computational domain was 2.0 m by 2.0 m by 2.0 m with a uniform grid cell size of 4 cm and the simulation was run for a total of 300 s simulation time. Propane was used as the fuel with a soot yield of 2% and a critical flame temperature, a parameter in FDS "that attempts to gauge whether or not combustion is viable", of 1554 K [7, 33]. Figure 2.6 shows the model geometry of the FDS LANL Glovebox as visualized in Smokeview. Five thermocouple trees were located in the FDS glovebox that corresponded to the experimental setup. The Fire Foe^{TM} tube was placed in the same location as in the experiment. The tube was modeled in FDS as a multi-layered surface with properties and thickness of

Nylon 6,6, and Envirogel^{TM} as the inner fluid. As previously noted, Envirogel^{TM} was composed of 70% by volume FE-36 and 30% by volume sodium bicarbonate. Density and specific heat of the inner fluid were approximated as the volume weighted average of the density and specific heat of FE-36, and sodium bicarbonate. Effective thermal conductivity of the inner fluid was calculated using the Maxwell-Eucken equation for particles dispersed within a continuous medium

$$k_{eff} = \frac{k_1 v_1 + k_2 v_2 \frac{3k_1}{2k_1+k_2}}{v_1 + v_2 \frac{3k_1}{2k_1+k_2}} \tag{2.3}$$

where k_1 and v_1 are the thermal conductivity and specific volume of the continuous phase respectively, and k_2 and v_2 are the thermal conductivity and the specific volume of the dispersed phase respectively [34].

The Fire Foe^{TM} was instrumented with four thermocouples and four devices to measure net heat flux. Table 2.2 shows the thermal properties of the materials used in the simulations [33].

Table 2.2: Thermal properties of FDS materials

Material	Conductivity (W/m-K)	Specific Heat (kJ/kg-K)	Density (kg/m^3)
AISI 302	15.1	0.48	8055
Plate Glass	1.4	0.75	2500
Gypsum	0.48	0.84	1440
Nylon 6,6	0.25	1.67	1140
Envirogel	0.07	1.32	1273

The FDS simulations were computed on a high-performance Linux computing cluster at UT Austin for the four different fire sizes tested: 13 kW, 20 kW, 25 kW, and 50 kW. Total CPU time for each simulation was on the order of 30 hrs. For these

four simulations, the net heat flux $\dot{q}''_{net}$ incident upon the Fire Foe^{TM} was time and spatially averaged over the surface of the tube. This net heat flux value was later used as an input into a sub-grid, thermo-physical, semi-empirical model of the Fire Foe^{TM} tube to predict activation time due to thermal degradation and working fluid expansion within the tube. The sub-grid, thermo-physical, semi-empirical model is described in the following section.

2.2.5.2 Fire Foe^{TM} tube sub-model

The Fire Foe^{TM} tube sub-model uses the net heat flux $\dot{q}''_{net}$ as an input and predicts Fire Foe^{TM} activation time. The net heat flux affects both tube-wall and working fluid temperatures, Figure 2.7. A simple lumped model is used to approximate the changes in tube wall temperature associated with the net heat flux. It is assumed that there is no phase change of the nylon or working fluid and that the thermo-physical properties of the nylon (i.e. specific heat, density, etc.) do not change greatly with increased temperature. Note that the heat transfer process between the tube wall and the working fluid are considered to be small relative to the net heat flux at this point.

The change in temperature of the wall over time is given by

$$\frac{dT_{wall}}{dt} = \frac{\dot{q}''_{net}}{(\delta \rho_{wall} c_{wall})} - \frac{2h_{in}}{R_{inner} \rho_{fluid} c_{fluid}} (T_{wall} - T_{fluid}) \tag{2.4}$$

where δ is the Fire Foe^{TM} tube thickness, and c_{wall} and ρ_{wall} are the specific heat capacity and density of Nylon 6,6, respectively.

The change in temperature of the inner fluid assuming no phase change or chemical reactions in the working fluid over time is given by

$$\frac{dT_{fluid}}{dt} = \frac{2h_{in}}{R_{inner}\rho_{fluid}c_{fluid}}(T_{wall} - T_{fluid}) \tag{2.5}$$

where h_{in} is the heat transfer coefficient between the working fluid and the tube wall, R_{inner} is the inner radius of the Fire Foe^{TM} tube, ρ_{fluid} and c_{fluid} are the density and specific heat capacity of the fluid, respectively, T_{wall} is the wall temperature, and T_{fluid} is the temperature of the working fluid within the Fire Foe^{TM}.

The pressure rise in the tube is assumed to be due to the FE-36 component within the Envirogel^{TM} fire suppression agent. The FE-36 is at a liquid state at ambient temperature and the pressure to which the Fire Foe ^{TM} tube is charged of 690 kPa. The change in pressure with change in temperature of the fluid is assumed to be a constant volume pressure increase approximated as

$$\frac{dP_{fluid,t}}{dT_{fluid,t}} = \frac{dP_{fluid,satliq}}{dT_{fluid,satliq}} \tag{2.6}$$

where dP_{fluid} and $dT_{fluid,t}$ are the change in pressure and temperature of the fluid at time t, and $dP_{fluid,satliq}$ and $dT_{fluid,satliq}$ are corresponding changes in pressure and temperature for saturated FE-36. These changes in saturated pressure and temperature are documented in the Material Safety Data Sheet (MSDS) provided by Dupont [35]. This process is shown schematically in Figure 2.8.

The hoop stress on the wall is approximated by a force balance on a thin walled tube ignoring axial stresses

$$\sigma = \frac{P_{fluid}R_{inner}}{\delta} \tag{2.7}$$

where σ is the hoop stress, P_{fluid} is the pressure of the fluid, R_{inner} is the inner radius of the Fire Foe^{TM} tube, and δ is the tube thickness, Figure 2.9.

Fire Foe^{TM} activation is assumed to occur when the inner hoop stress exceeds the Nylon 6,6 yield strength, which is a function of the tube wall temperature, as shown in Table 2.3 [36]. A parameter in the sub-model is used to reduce the nylon yield strength because of plastic deformation.

Table 2.3: Nylon yield strength as a function of temperature

Temperature (°C)	Yield strength (MPa)
23	80
77	62
130	25
200	10

2.2.6 Test Observations

The test observations are detailed in this section. First the gas temperature time evolution for the ten fire tests with four different fire sizes are presented, then predicted and measured Fire Foe^{TM} tube activation events and associated times are discussed.

2.2.6.1 Comparison of Predicted Values to Experimental Measurements

Table 2.4 shows a summary of the Fire Foe^{TM} activation times and associated HGL temperatures for the 10 tests. It is not surprising that the larger fires produced higher HGL temperatures and thus earlier activation times. The standard deviation in the activation time is 47 s, 7 s, and 2 s for the 13 kW, 25 kW, and 50 kW cases respectively. The large standard deviation for activation times at the lower fire heat release rates may be due to uncertainty in the flow of propane to the sand burner.

Fire Foe^{TM} wall temperatures for the 13 kW, 20 kW, and 50 kW cases are

Table 2.4: Fire Foe^{TM} activations time and associated HGL temperatures

Fire Size (kW)	Test No.	HGL Activation Temp (°C)	Fire Foe^{TM} Activation (s)
13	1	263	239
	2	197	188
	3	212	145
20	1	242	143
25	1	320	57
	2	335	66
	3	348	53
50	1	399	17
	2	421	20
	3		16

shown in Figure 2.10. In the first roughly 15 s of the three 13 kW tests and the 20 kW test, the initial temperature increase of the Fire Foe^{TM} tube wall looks like the temperature increase in the 50 kW tests. The reason for this initial large temperature increase is likely due to the ignition system used. For the 13 kW, 20 kW, and 25 kW cases, a spark igniter was used to ignite the propane sand burner. For each ignition, propane had been flowing into the glovebox for a short amount of time before ignition. This resulted in an initial high heat release rate. The flame heights for one of the 25 kW tests is shown in Figure 2.11 at ignition onset (top) and after the fire has relaxed to the desired heat release rate (bottom). For the 50 kW cases, again, small candles were fixed to the sand burner to allow ignition of the propane sand burner.

Data from the ten tests are summarized in Figures 2.12 through 2.21. For Figures 2.12 through 2.15 and Figures 2.19 through 2.21 corresponding to the three 13 kW tests, the 20 kW test, and the three 50 kW tests there are a total of eight subfigures. The subfigures, going from right to left, up to down, correspond to the

measured temperatures from the A, B, C, D and centerline thermocouple trees from both experiments and FDS. The following subfigure corresponds to Fire Foe^{TM} wall temperatures for both experiments and FDS. The seventh figure corresponds to the predicted peak temperature from FDS versus the measured peak temperatures for all thermocouple trees, and the eighth figure corresponds to the predicted peak temperature of the suppression system versus the measured peak wall temperatures of the Fire Foe^{TM} tube.

Figures 2.16 through 2.18 correspond to the three 25 kW tests in which Fire Foe^{TM} tube wall temperatures were not measured. The first five subfigures correspond to the measured temperatures from the A, B, C, D and centerline thermocouple trees from both experiments and FDS. The following subfigure corresponds to the predicted peak temperature from FDS versus the measured peak temperatures for all thermocouple trees. For all cases, the sudden drop off in experimental temperature indicates Fire Foe^{TM} activation.

For the first 13 kW test, Figure 2.12, for the A thermocouple tree FDS is predicting temperatures that are about 60°C higher than those measured. The B thermocouple shows good agreement between experiment and FDS predicted temperatures for the top two thermocouples, however, experimental temperatures are showing more stratification with almost a 100°C temperature difference in the bottom thermocouple. Thermocouple tree C shows about a 75°C temperature difference between the bottom thermocouples until about 80 s into testing. At this point the bottom thermocouple shows good agreement between experimentation and FDS. Thermocouples C1 and C2 show about a 50°C temperature difference throughout the test. Thermocouple tree D shows more pronounced stratification in the temperature measurements when compared to the FDS cases. Temperatures for the CL ther-

mocouple tree shows good agreement between the measured and FDS results. Fire Foe^{TM} experimental temperatures are higher than FDS temperatures by between 30 and 50°C throughout the experiment. Fire Foe^{TM} thermocouple FF5 (solid green) shows markedly higher temperatures than the rest of the thermocouples. This particular thermocouple detached itself from the Fire Foe^{TM} early on in experimentation and therefore is reading gas temperatures instead of Fire Foe^{TM} wall temperatures.

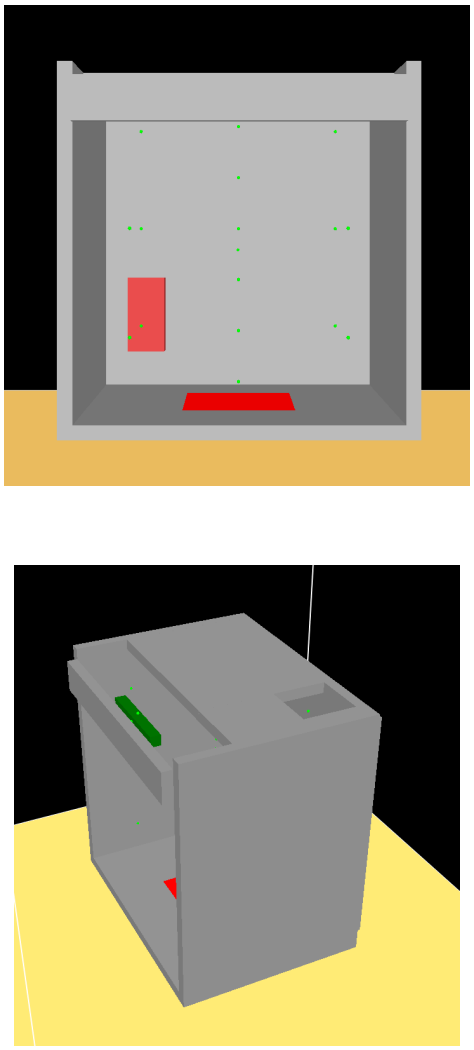

Figure 2.6: FDS model of LANL glovebox

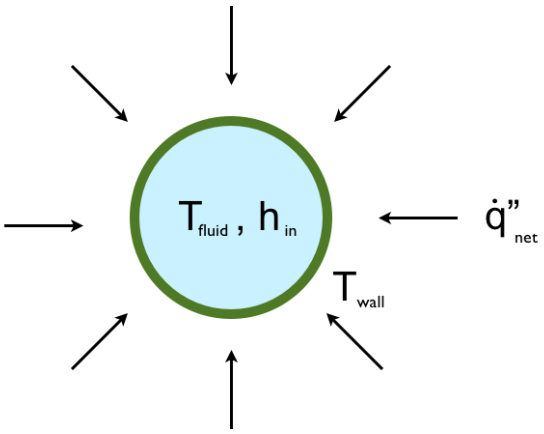

Figure 2.7: Simple heat transfer model to the Fire Foe^{TM} tube

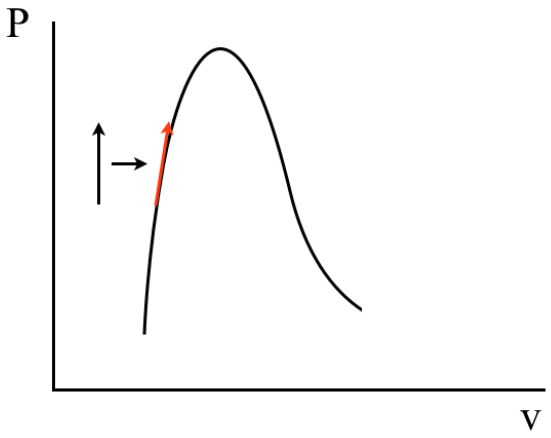

Figure 2.8: Approximation for the constant volume pressure increase of the fire suppressant

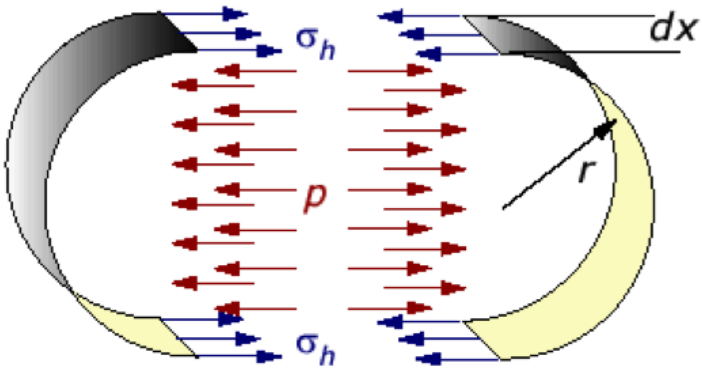

Figure 2.9: Force balance on a thin walled tube

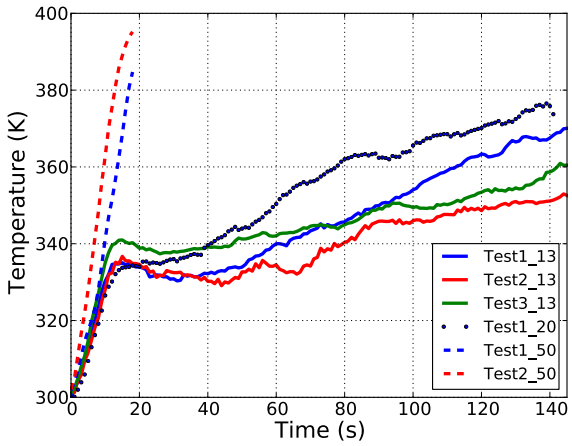

Figure 2.10: Experimental suppression system temperatures for the 13 kW, 20 kW, and 50 kW cases

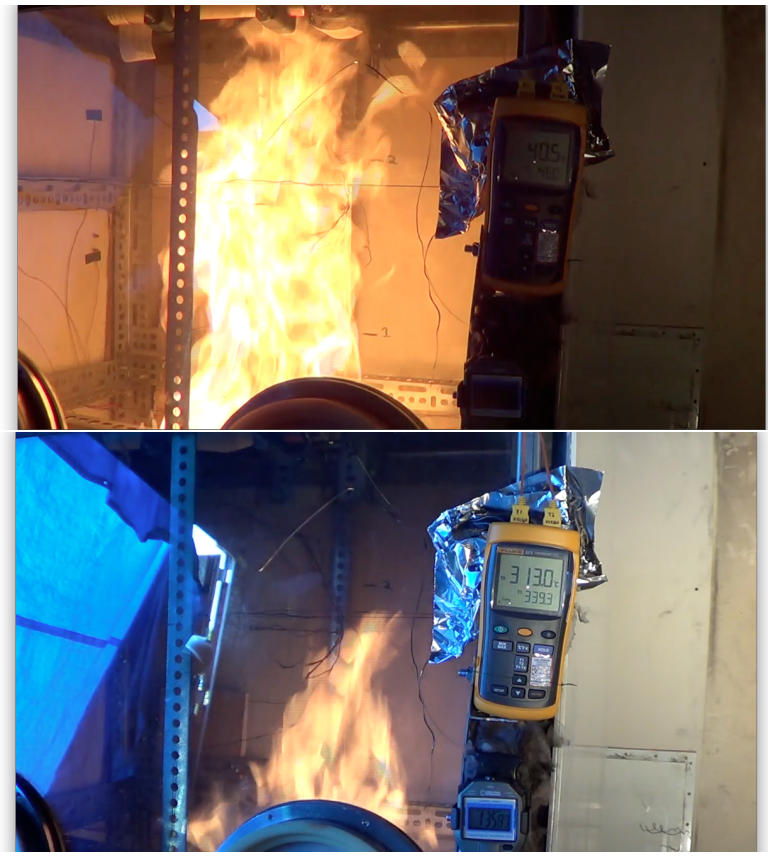

Figure 2.11: Flame heights for 25 kW Fire Foe^{TM} activation test

The A thermocouple tree in the second 13 kW test, Figure 2.13, is also showing more stratification in the experimental measurements. Between the measured temperatures and the FDS temperatures, there is roughly a 70°C to 100°C difference in the A thermocouple tree, with the most discrepancy occurring in the bottom most thermocouple, A1. The B thermocouple tree similarly also shows more stratification in the experimental data, however measured versus FDS temperature differences are on the order of 50°C to 70°C. For the C thermocouple tree there is less stratification in the measured temperatures and differences between the measured temperatures and FDS temperatures are around 30°C to 50°C. The D thermocouple tree follows the trend of thermocouple trees A and B with pronounced stratification in the measured temperatures and differences in measured temperatures and FDS temperatures on the order of 100°C. For the centerline thermocouples, the most discrepancies in measured temperatures and FDS temperatures are in thermocouple CL6. The other thermocouples show fairly good agreement. Measured Fire Foe^{TM} wall temperatures and FDS Fire Foe^{TM} wall temperatures agree fairly well.

For the third 13 kW test, Figure 2.14, there are large differences between the measured temperatures and the FDS predicted temperatures for the A thermocouple tree. The bottom most thermocouple, A1, is showing temperature differences on the order of 150°C to 200°C. The other two thermocouples are showing temperature differences at around 60°C to 70°C. For the B thermocouple tree, the bottom most thermocouple is showing the largest temperature discrepancies at around 90°C to 100°C. The other two thermocouples are showing temperature differences from 10°C to 50°C. For the C thermocouple tree FDS is overpredicting temperatures between 10°C at around 100 s and 100°C at around 40 s. FDS is also overpredicting temperatures for the D thermocouple tree with the largest discrepancies at around 60°C. The centerline temperatures agree fairly well between the measured temper-

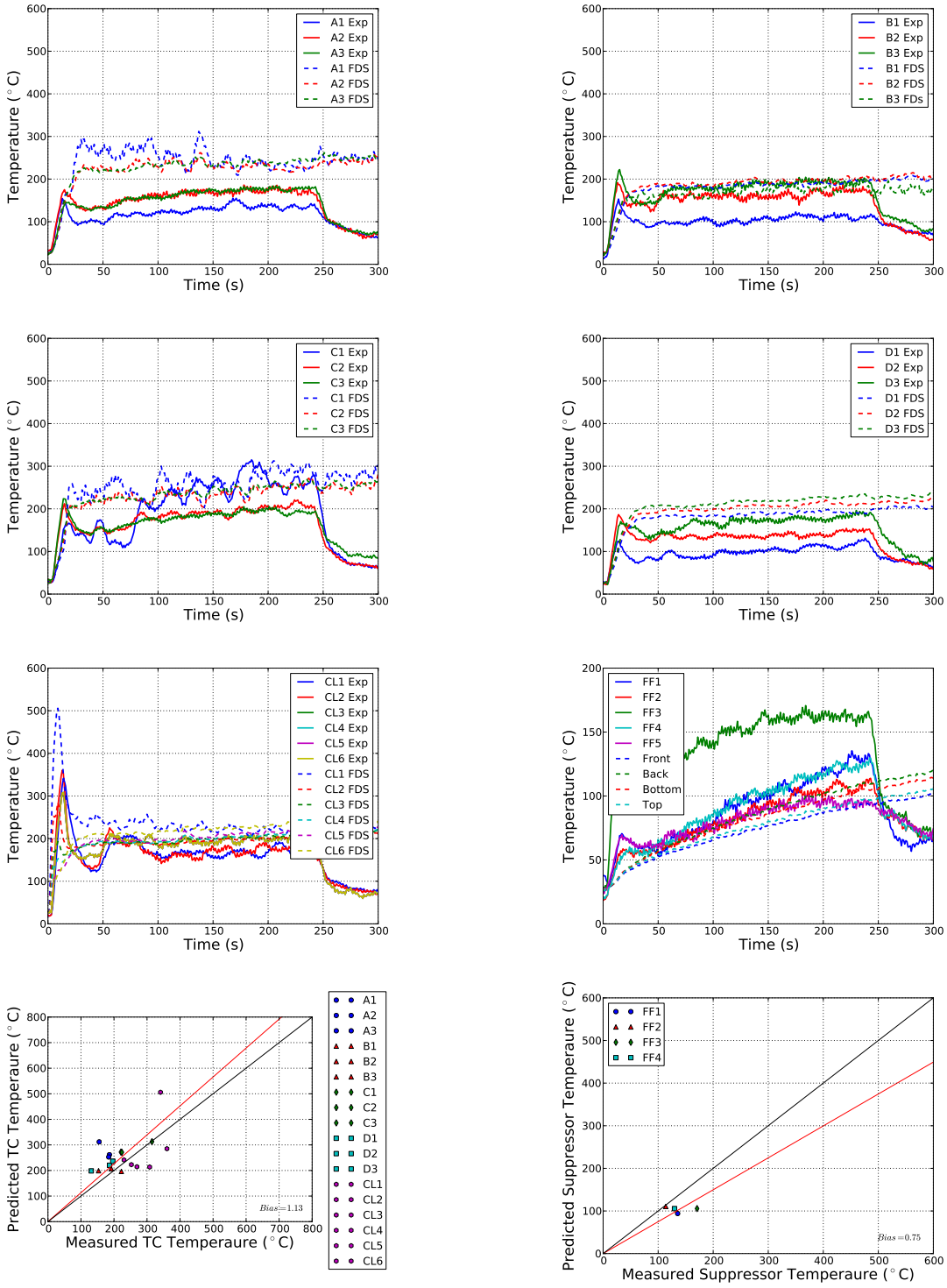

Figure 2.12: Temperatures for Fire Foe^{TM} activation tests, 13 kW test 1

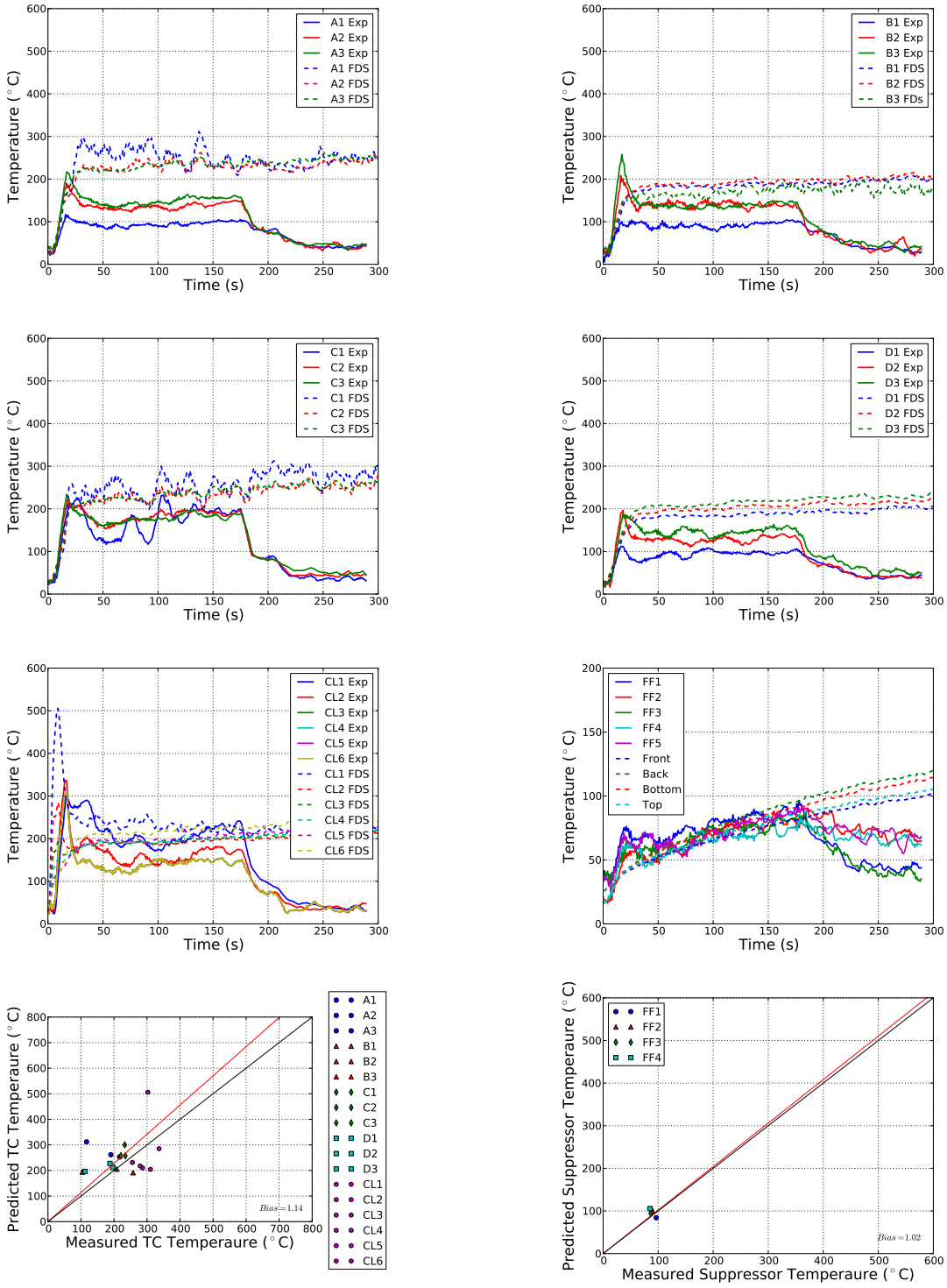

Figure 2.13: Temperatures for Fire Foe^{TM} activation tests, 13 kW test 2

atures and the FDS temperatures. Near the beginning of the test, measured Fire Foe^{TM} are higher than the FDS temperatures, however at activation (about 150 s) there is little difference in temperature.

The 20 kW test, Figure 2.15, shows a large difference between measured and predicted temperatures in the A thermocouple tree. FDS is overpredicting temperatures by nearly 200°C in thermocouple, A1, and roughly 150°C overall. The B thermocouple tree again shows more stratification in the measured temperatures with FDS overpredicting temperatures by roughly 100°C for the bottom most thermocouple, B1, 20°C to 50°C for the other two thermocouples. FDS is also overpredicting temperatures in the C and D thermocouple trees. The center line thermocouple tree initially shows good agreement between measured temperatures and FDS, however there is a large amount of noise at around 100 s. FDS is underpredicting Fire Foe^{TM} wall temperatures. Thermocouple FF3 (solid green) also seems to have detached from the Fire Foe^{TM} and is reporting temperatures much higher than the other thermocouples attached to the tube. The large discrepancies between the experimental temperatures and the FDS predicted temperatures could be a result of uncertainty in the flowrate of propane in the experimental tests. Recall that uncertainty in the HRR of the experimental fires was approximately 4 kW.

As in the 13 kW and 20 kW cases, the first 25 kW test, Figure 2.16, the measured temperatures are showing more stratification when compared to FDS temperatures. The largest temperature differences in the A thermocouple tree are again due to the A1 thermocouple at about 150°C. FDS tends to overpredict temperatures for the A thermocouple tree until roughly 15 s before Fire Foe^{TM} activation (about 45 s). For the B thermocouple tree, there is less stratification in the measured temperatures and FDS is now underpredicting temperatures by about 100°C to 150°C.

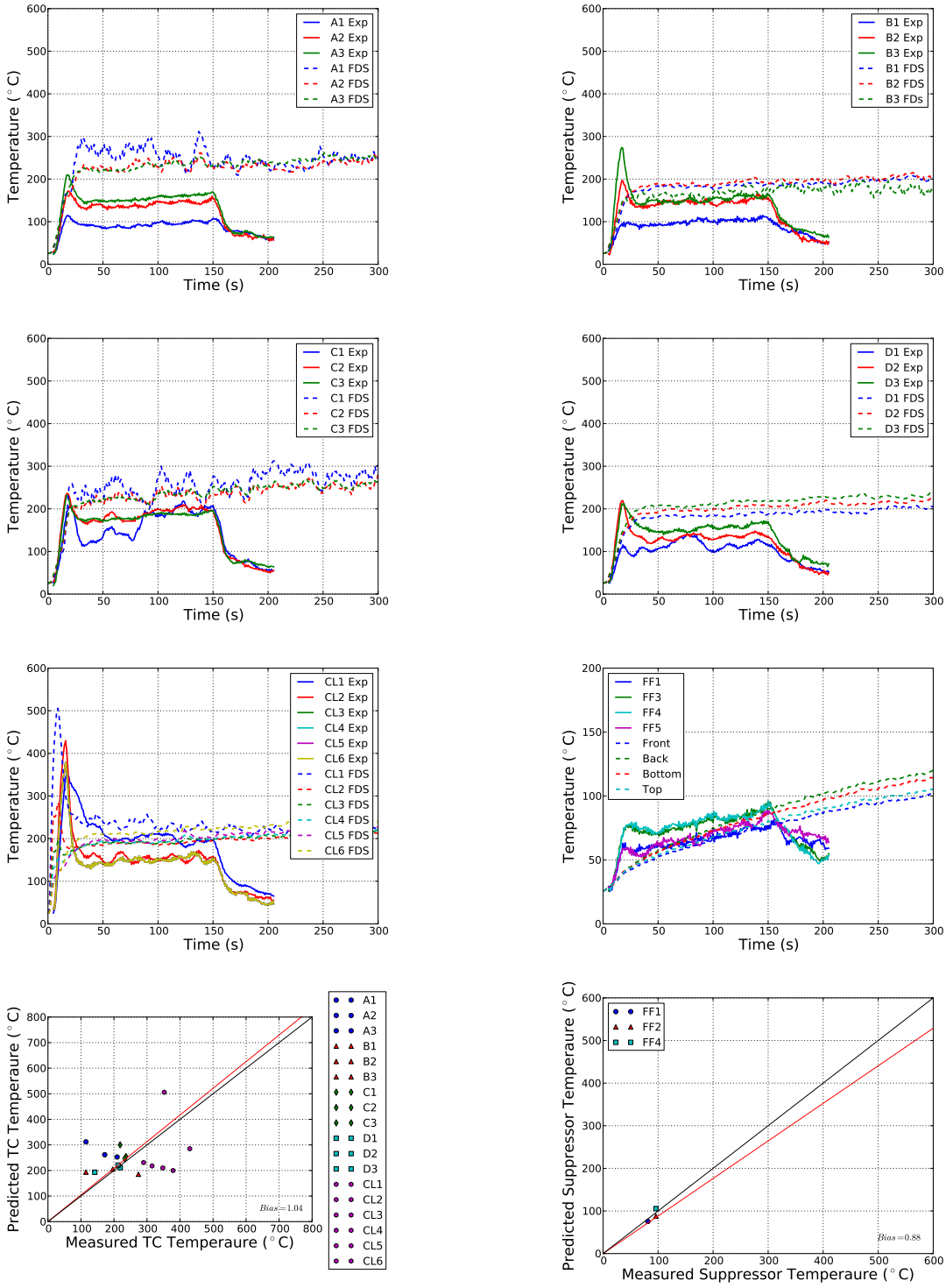

Figure 2.14: Temperatures for Fire Foe^{TM} activation tests, 13 kW test 3

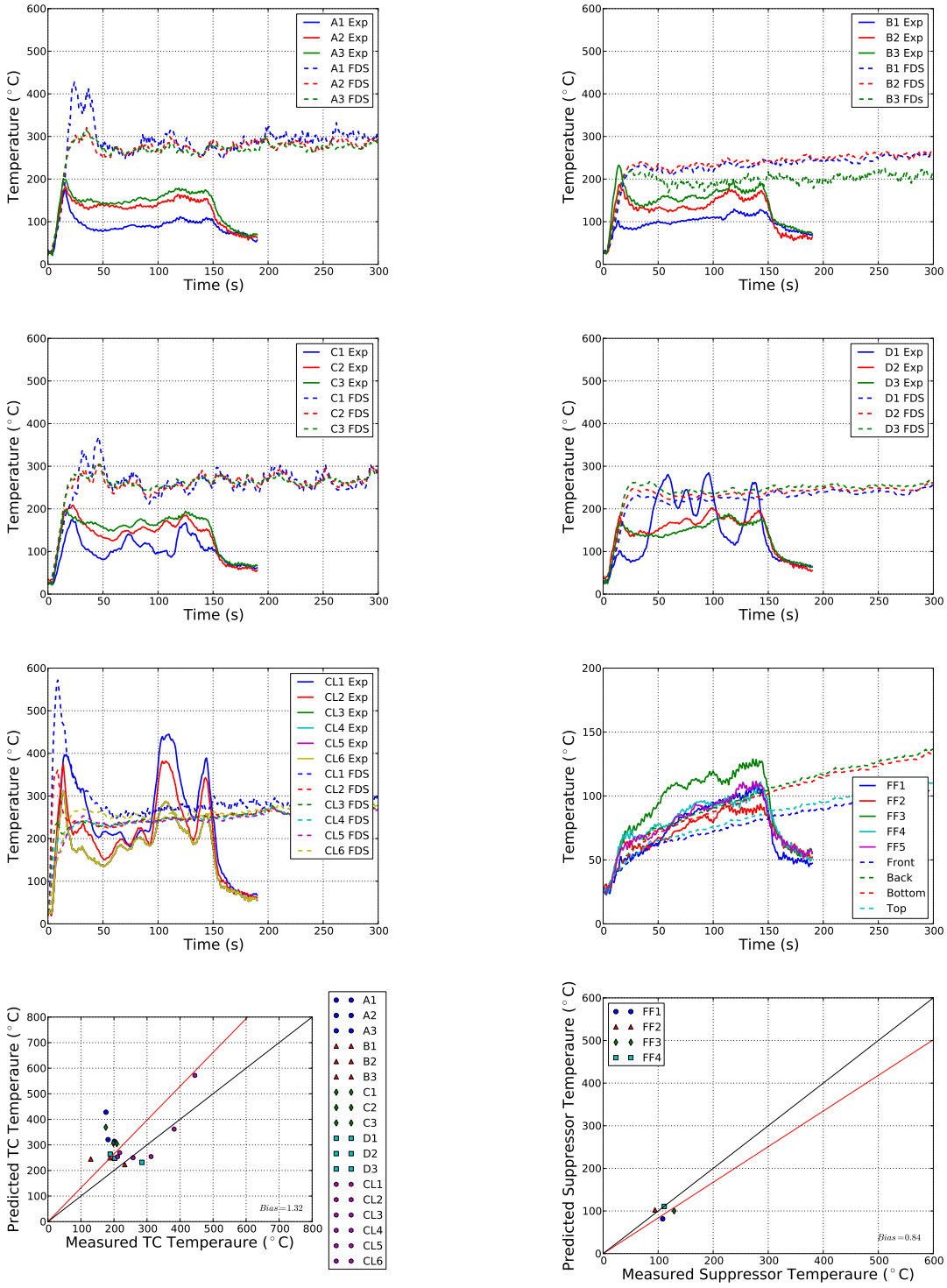

Figure 2.15: Temperatures for Fire Foe^{TM} activation tests, 20 kW test 1

For the C thermocouple tree there is good agreement between the measured and FDS temperatures after about 35 s. Before this, FDS is overpredicting temperatures by about 70°C to 180°C. There is also fairly good agreement in the D thermocouple tree, however FDS is overpredicting temperatures in the bottom most thermocouple, D1, by about 50°C. FDS is underpredicting temperatures in the centerline thermocouple tree by around 200°C.

The second 25 kW test, Figure 2.17, shows good agreement between measured temperatures and FDS temperatures in thermocouple tree A except for thermocouple A1. In thermocouple A1, FDS is overpredicting temperatures by about 100°C. In the B thermocouple tree, FDS is underpredicting temperatures and this time the larges discrepancies are in thermocouple B3 with temperature differences at about 150°C. For thermocouple trees C and , FDS is underpredicting the second and third temperatures and overpredicting first thermocouple temperatures. Again there is more stratification in the measured temperatures versus the FDS temperatures. FDS is also underpredicting center line temperatures.

25 kW test 3, Figure 2.18, also shows more pronounced stratification in the A thermocouple tree measured temperatures versus the FDS temperatures. The bottom most thermocouple, A1, is also showing temperature differences of about 150°C. FDS is underpredicting temperatures in thermocouple tree B, by about 150°C in the B3 thermocouple, and about 50°C in the B1 thermocouple. For the C thermocouple tree C2 and C3 temperatures agree well between those measured and FDS, however FDS is underpredicting C1 temperatures by nearly 250°C in some places. For thermocouple tree D, FDS is underpredicting temperatures for the D2 and D3 thermocouples and overpredicting temperatures for the D1 thermocouple by up to 80°C. FDS is also underpredicting centerline thermocouple temperatures by up to 200°C.

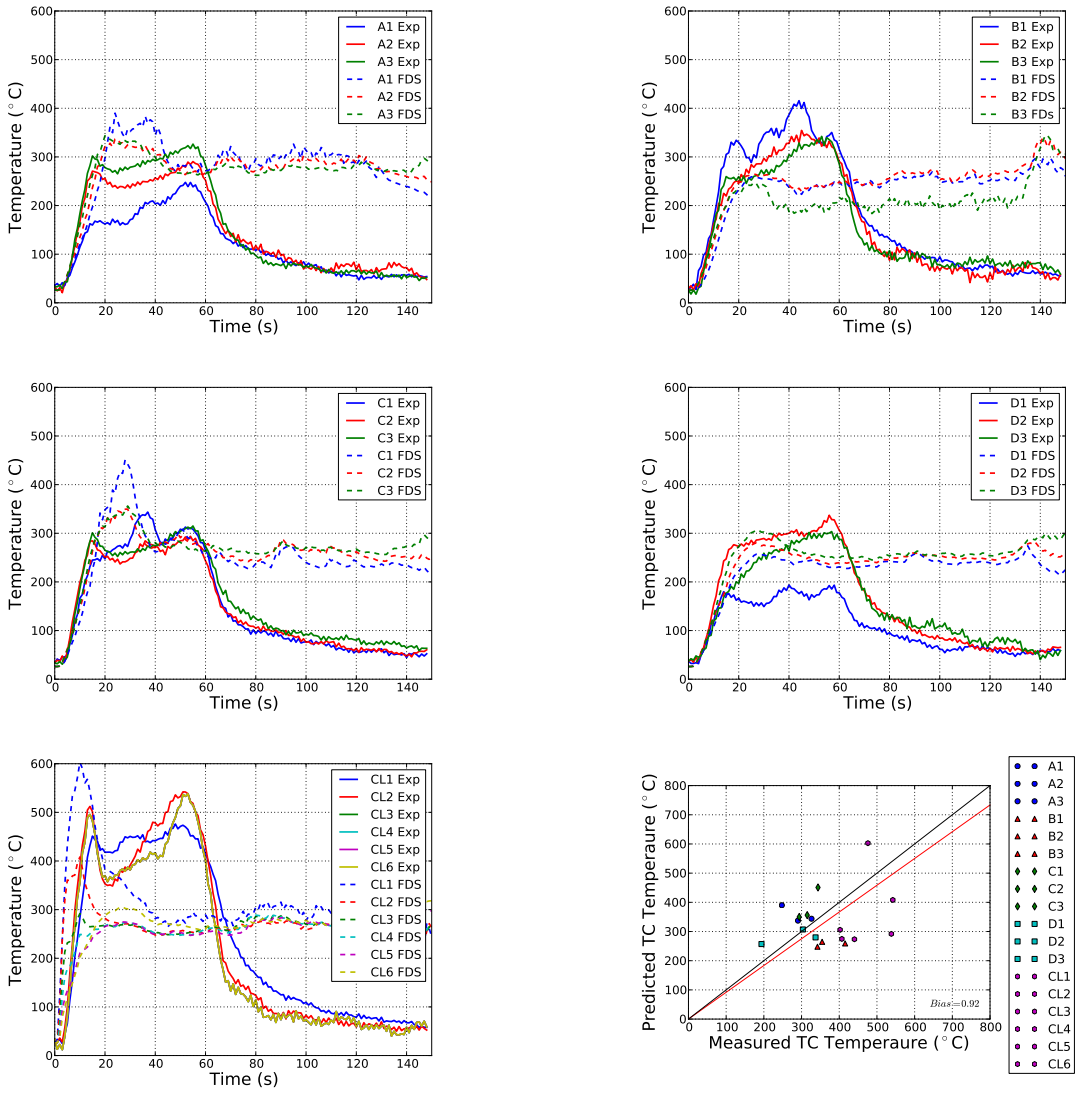

Figure 2.16: Temperatures for Fire Foe^{TM} activation tests, 25 kW test 1

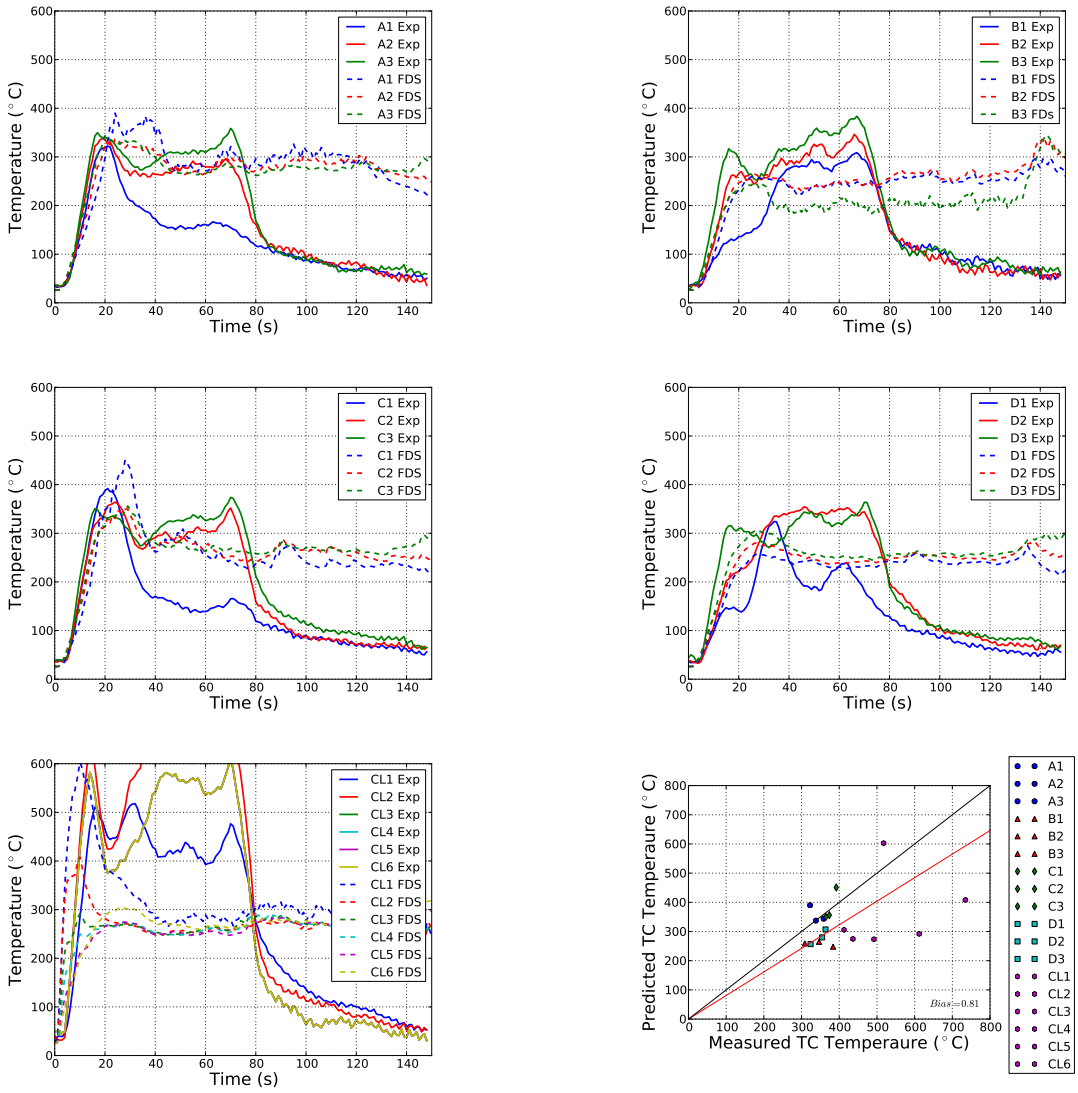

Figure 2.17: Temperatures for Fire Foe^{TM} activation tests, 25 kW test 2

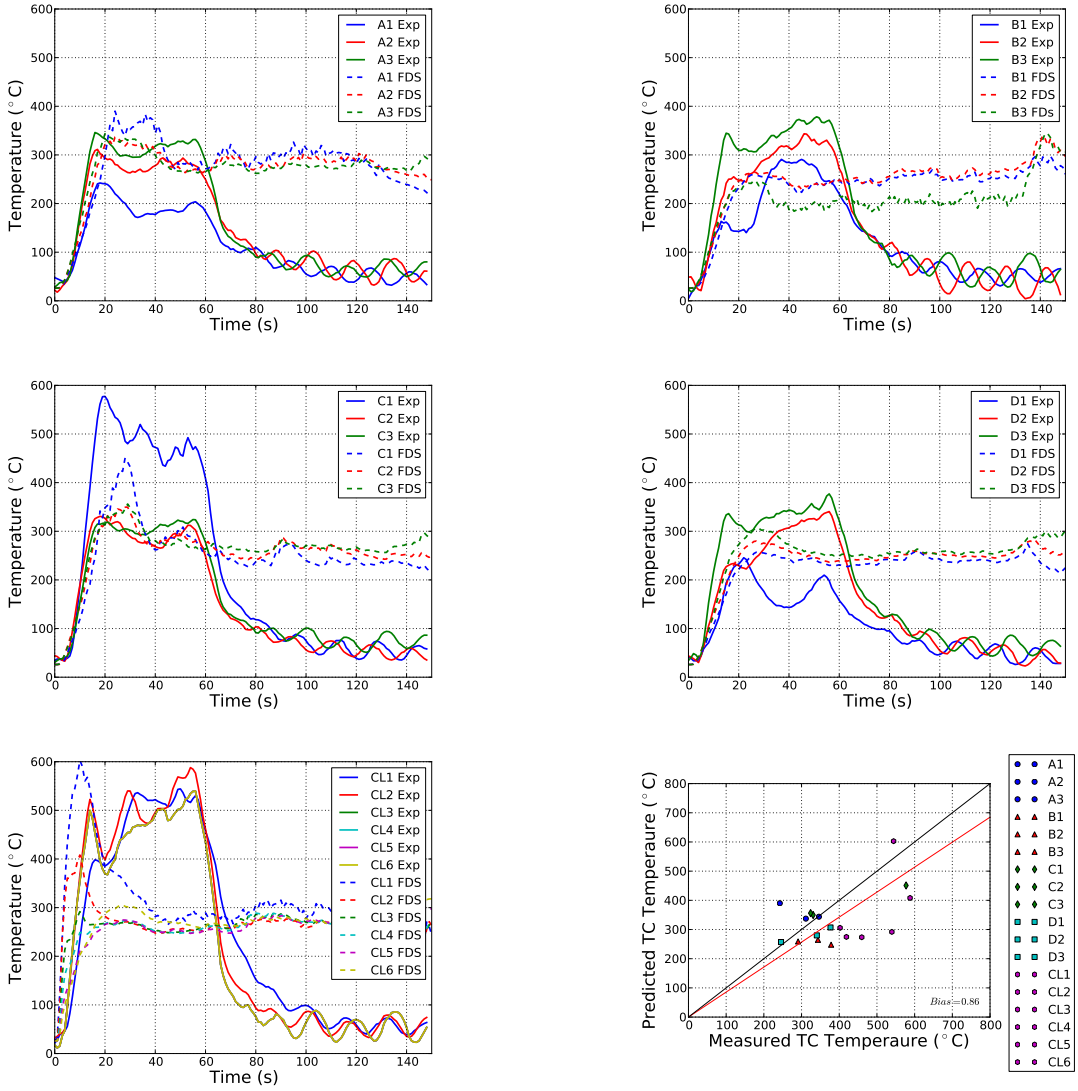

Figure 2.18: Temperatures for Fire Foe^{TM} activation tests, 25 kW test 3

Thermocouple tree A of the first 50 kW test, Figure 2.19, shows more stratification in the measured data versus the FDS temperatures. FDS is also overpredicting temperatures up to 300°C, thermocouple A1. For the B thermocouple tree, FDS is also overpredicting temperatures overall. For thermocouples B2 and B3, FDS is overpredicting by about 50°C, and for thermocouple B1, FDS is overpredicting temperatures by about 170°C. Like thermocouple tree A, FDS is greatly overpredicting temperatures in thermocouple tree C. For thermocouple tree D, FDS is underpredicting thermocouple D1, however thermocouples D2 and D3 agree reasonably well with experimental data. The centerline temperatures from FDS also agree well with measured experimental data. For the Fire Foe^{TM} tube wall temperatures, FDS is underpredicting peak temperatures by up to 80°C.

For the second 50 kW test, thermocouples A1 and B1 did not record experimental data. Looking at thermocouple tree A, FDS is still overpredicting temperatures by about 100°C to 120°C. For thermocouple tree B, FDS thermocouple B3 shows good agreement with measured temperatures, however, FDS is overpredicting thermocouple B2 temperatures by roughly 60°C. For thermocouple tree C, measured temperature data shows more stratification than FDS. The largest temperature differences in thermocouple C are due to thermocouple C1. FDS is overpredicting temperatures by roughly 160°C. Thermocouple tree D shows good agreement between FDS temperatures and measured temperatures, with temperature differences between the two on the order of 10°C for thermocouples D2 and D3. FDS is however underpredicting temperatures for thermocouple D1 by nearly 100°C. For the centerline thermocouples FDS is initially overpredicting temperatures until about 15 s into the test. FDS is underpredicting Fire Foe^{TM} wall temperatures up to 70°C.

For the last of the 50 kW tests, Figure 2.21, thermocouple tree A again shows

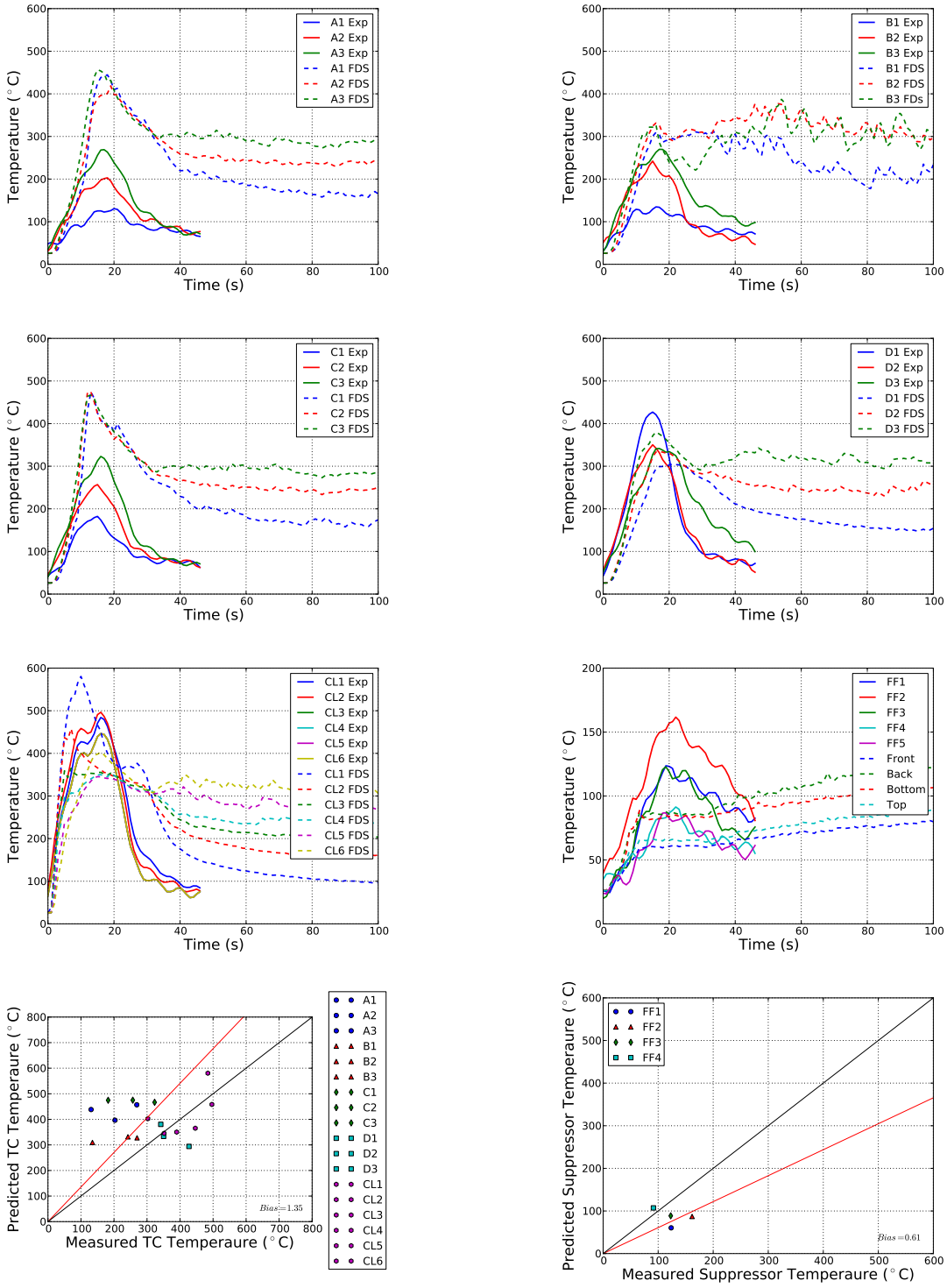

Figure 2.19: Temperatures for Fire Foe^{TM} activation tests, 50 kW test 1

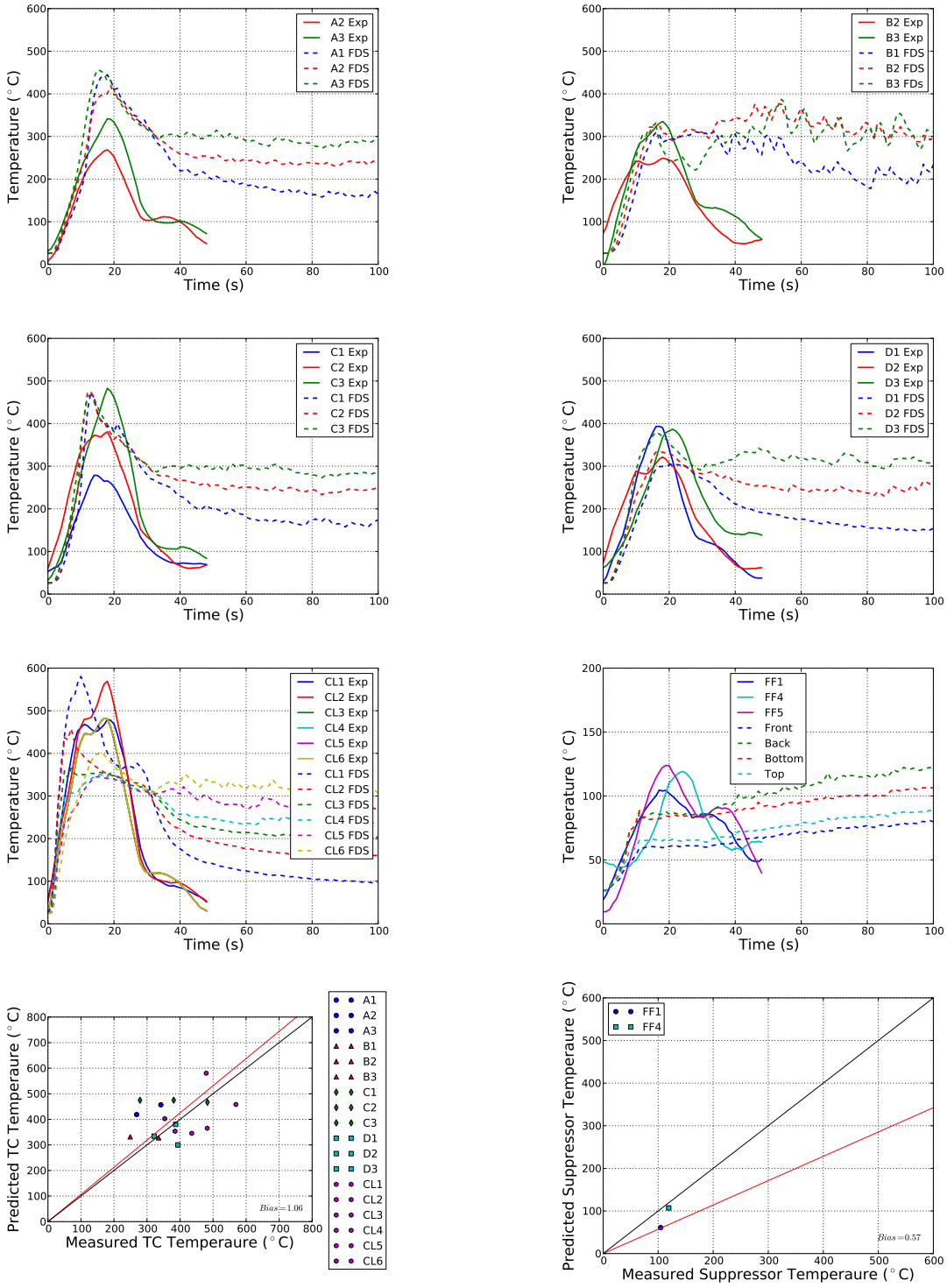

Figure 2.20: Temperatures for Fire Foe™ activation tests, 50 kW test 2

pronounced stratification in the measured temperatures. FDS continues to overpredict temperatures with the largest temperature differences of around 300°C being in the A1 thermocouple. For the B thermocouple tree, FDS temperatures for the B2 and B3 thermocouples agree will with the measured data, however there is nearly a 150°C difference in the B1 thermocouple. FDS is also overpredicting temperatures in thermocouple tree C with the largest temperature differences again arising in thermocouple C1, roughly 150°C. Thermocouple tree D shows good agreement between the FDS temperatures and the measured temperatures. Centerline temperatures also show good agreement. FDS, however, is underpredicting Fire Foe™ temperatures by up to 60°C.

For the three 13 kW tests FDS is overpredicting peak gas phase thermocouple temperatures overall. For 13 kW test 1 FDS is underpredicting peak Fire Foe™ wall temperatures by 25%, for test 2 FDS is slightly overpredicting peak wall temperatures by 2%, and for test 3 FDS is underpredicting peak wall temperatures by 15%. This is shown in the last subfigure of Figures 2.12 through 2.14. For the 20 kW case FDS is overpredicting gas temperatures by about 30% and underpredicting Fire Foe™ wall temperatures by 16%. FDS is underpredicting gas phase temperatures by 8%, 19%, and 14% for the 25 kW test 1, 2 and 3 cases respectively, Figures 2.16 through 2.14. For the three 50 kW cases, FDS is overpredicting gas phase temperatures by 35%, 5%, and 18% for tests 1, 2, and 3 respectively. FDS is also underpredicting Fire Foe™ wall temperatures by 39%, 43%, and 40% for tests 1, 2, and 3 respectively. Overall, the measured temperatures within the glovebox are showing more stratification in experimentation than the FDS predicted temperatures. FDS could possibly be predicting higher gas phase mixing than what occurred in experimentation. Fire Foe™ temperatures are generally being underpredicted by 19%, Figure 2.22.

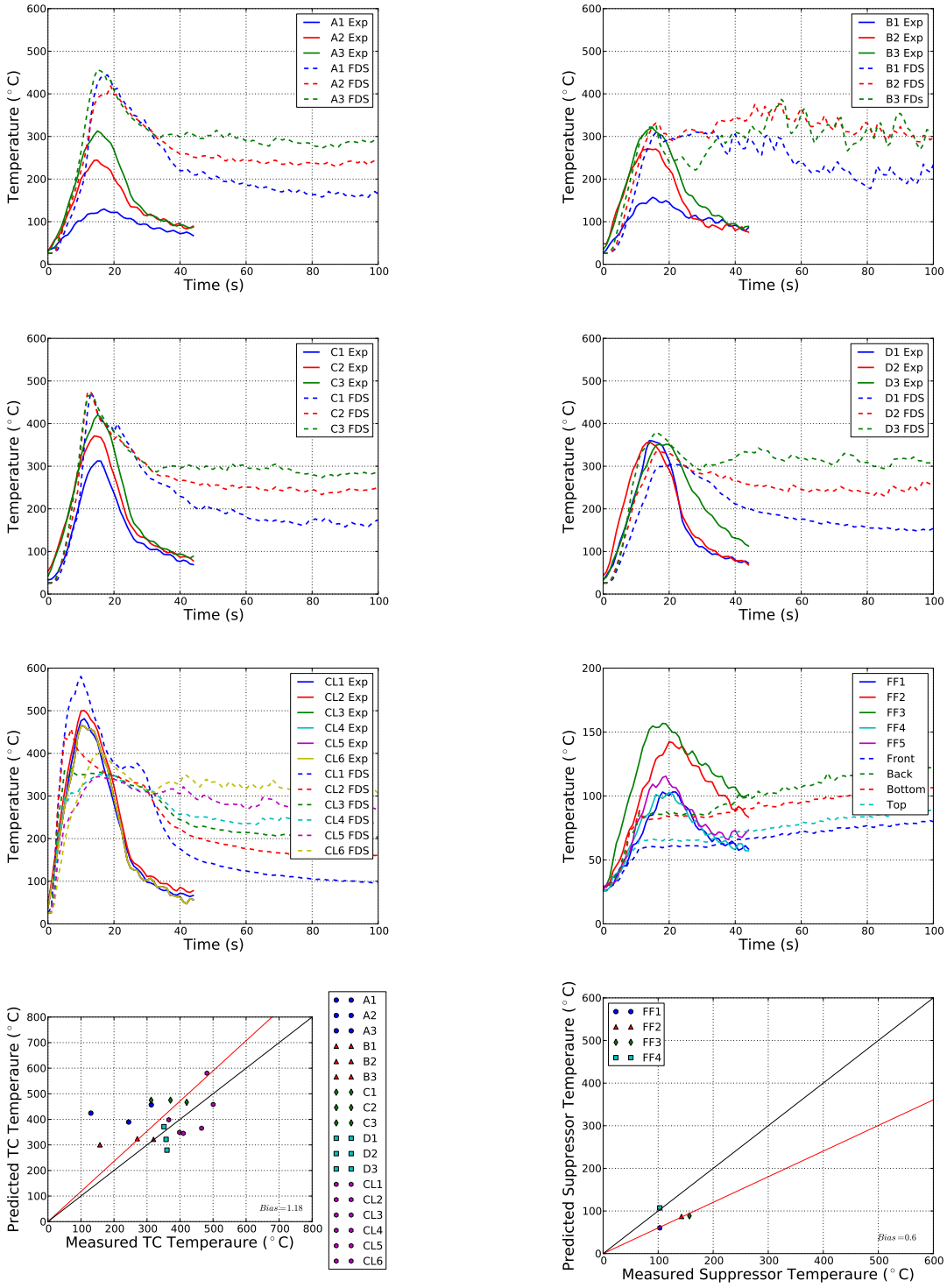

Figure 2.21: Temperatures for Fire Foe^{TM} activation tests, 50 kW test 3

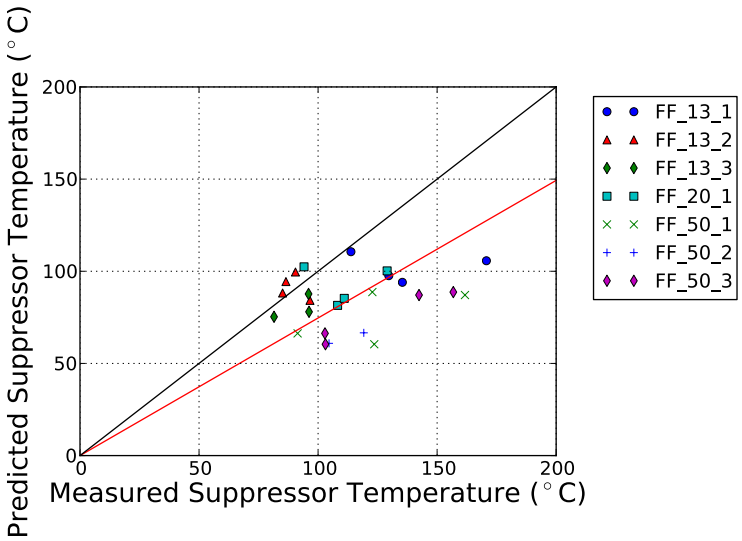

Figure 2.22: Fire Foe^{TM} temperatures for all tests

The tube sub-model utilizes a constant net heat flux to the tube to account for heat transfer to the Fire Foe^{TM} tube wall and inner working fluid. Figure 2.23 shows the reasoning behind using a constant heat flux to the tube. For the majority of the simulation, the net heat transfer rate to the tube is relatively constant for the 13 kW, 20 kW, and 25 kW cases. To get the constant heat flux to the Fire Foe^{TM}, the net heat fluxes from FDS were time averaged until the mean activation time and also spatially averaged. The values presented in Table 2.5 were then run through the sub-model to obtain wall and inner fluid temperatures.

Table 2.5: Time and spatially averaged net heat flux to suppression system

Fire HRR (kW)	Net Heat Flux (kW/m^2)
13	2.26
20	2.88
25	3.4
50	5.95

Fire Foe^{TM} tube wall and fluid temperatures are shown in Figure 2.24 for the tube sub-model (solid) and spatially averaged experimental (dashed). The sharp decay in temperatures for the tube sub-model indicate a predicted activation event. Experimental wall temperatures for one of the 50 kW cases were omitted, and Fire Foe^{TM} wall temperatures for the 25 kW cases were not recorded. The temperature differences predicted by the tube sub-model and the temperatures recorded for all the 13 kW and the one 20 kW cases initially have a large discrepancy until sub-model activation. This phenomenon was explained at the beginning of the section, and is most likely due to the intial large fire sizes for all but the 50 kW cases.

Fire Foe^{TM} fluid pressures are shown in Figure 2.25 for the 13 kW, 20 kW, 25 kW, and 50 kW cases. For the 13 kW case (top left), the pressure reaches a

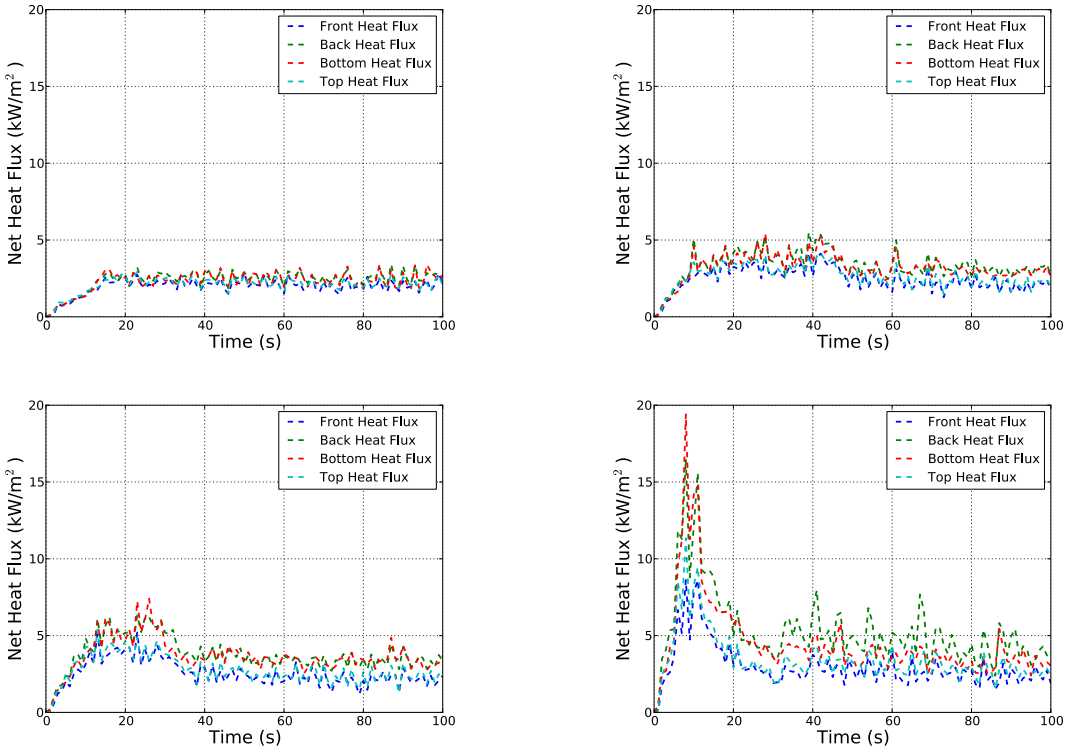

Figure 2.23: Net heat flux from FDS to the Fire Foe^{TM} tube for 13 kW (top left), 20 kW (top right), 25 kW (bottom left), and 50 kW (bottom right) cases

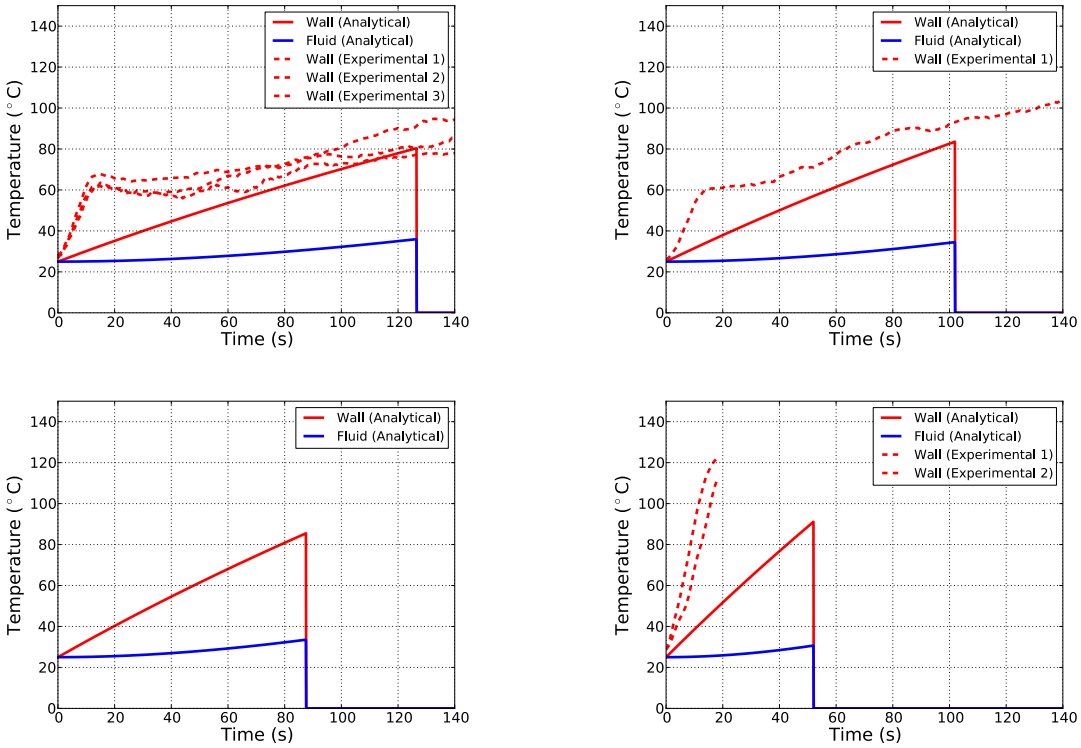

Figure 2.24: Sub-model Fire Foe^{TM} tube wall and fluid temperatures for 13 kW (top left), 20 kW (top right), 25 kW (bottom left), and 50 kW (bottom right) cases

maximum pressure of just over 1 MPa. For the 20 kW case (top right), the pressure within the tube just reaches roughly 1 MPa. For the 25 kW case (bottom left), the pressure within the Fire Foe^{TM} tube reaches just under 1 MPa. For the 50 kW case (bottom right), the peak pressure just before activation is at around 0.9 MPa.

The hoop stresses for the Fire Foe^{TM} tube wall, Figure 2.26, follows the pressure trends that were presented in Figure 2.25. The reduction in yield strength of the tube wall due to temperature increase is more pronounced in the higher heat flux cases with the 50 kW case having the greatest reduction in yield strength.

In the sub-model, the larger fire heat release rates did not necessarily mean higher fluid temperatures. Peak fluid temperatures were highest in the 13 kW case, second highest in the 20 kW case, third in the 25 kW case, and lowest in the 50 kW case. This accounted for lower hoop stresses in the tube wall with increasing fire heat release rate. On the other hand, peak tube wall temperatures did increase with increasing fire heat release rates. According to the sub-model, the failure mechanism in the tube is largely due to the thermal degradation, decreasing yield strength with temperature, of the nylon and not the stress increase due to fluid pressure increase.

A scatter plot of predicted activation times versus measured activation times is shown in Fig. 2.27. At higher heat release rates, shorter activation times, the model tends to overpredict activation time, at lower heat release rates, longer activation times, the model tends to underpredict activation times, and the model tends to overpredict activation time overall by 34%. Figure. 2.28 shows the measured activation time of the Fire Foe^{TM} tube to the experimental fire heat release rate for all 10 cases along with activation times from the models. Currently the sub-model contains a relatively simple model for tube failure and does not appear to capture the exponential behavior of the measured activation times. A greater understanding

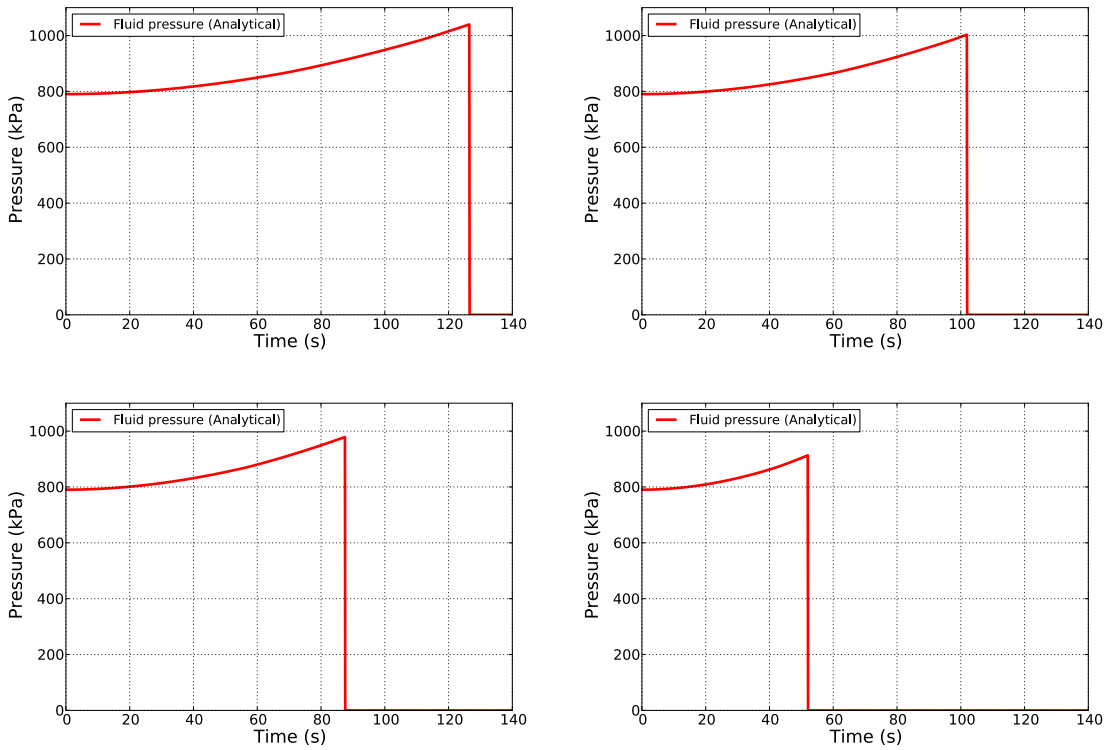

Figure 2.25: Sub-model fluid pressures for 13 kW (top left), 20 kW (top right), 25 kW (bottom left), and 50 kW (bottom right) cases

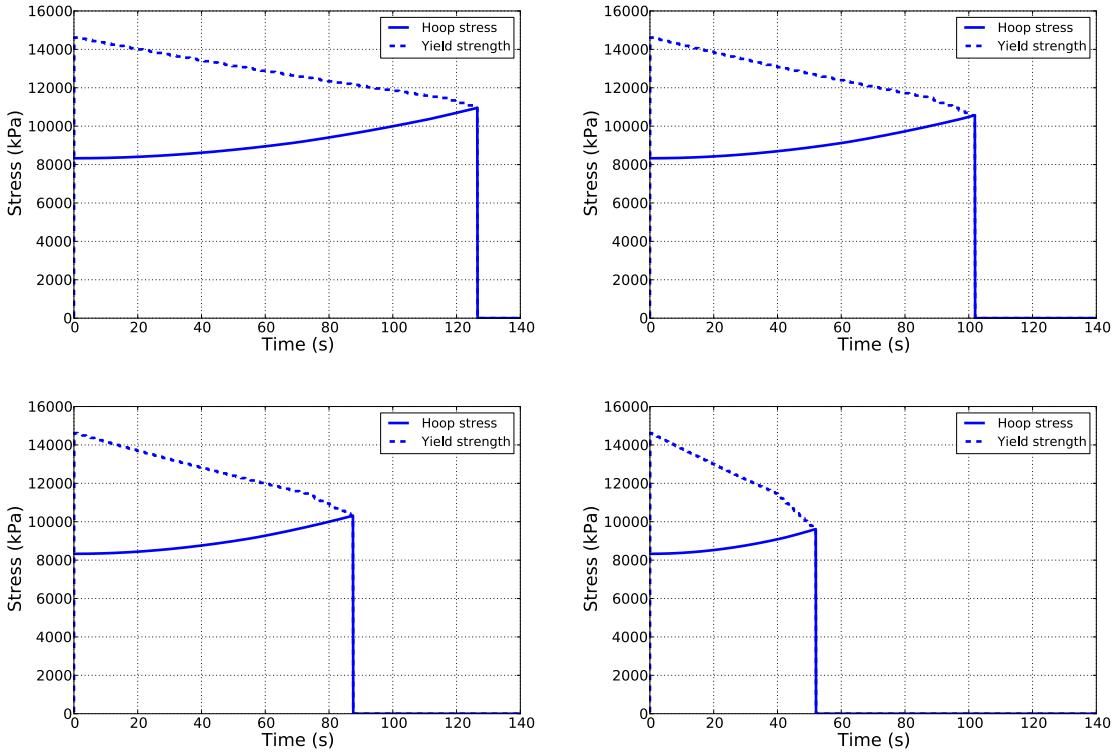

Figure 2.26: Sub-model hoop (solid) and yield (dashed) stresses for 13 kW (top left), 20 kW (top right), 25 kW (bottom left), and 50 kW (bottom right) cases

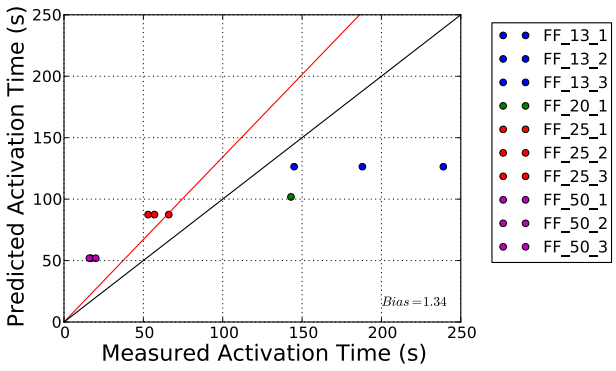

Figure 2.27: Fire Foe^{TM} activation times.

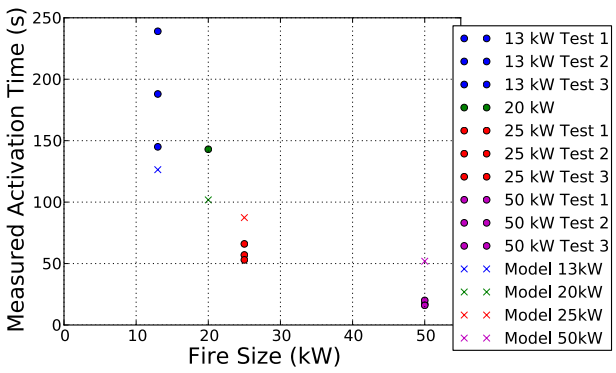

Figure 2.28: Experimental and Model Fire Foe^{TM} activations time vs. fire size

of material failure under high pressures and temperatures is required to understand the physics leading up to Fire Foe^{TM} activation.

2.2.7 Fire Foe Bayesian Parameter Inference

It was shown that the sub-model tube wall temperatures did not agree well with the experimental temperatures, see Figure 2.24. Because of this large discrepancy in temperatures, it was decided that a more robust model was to be used to find tube wall temperature. HGL temperatures from FDS were passed to this model instead of using a constant heat flux to the tube wall. Figure 2.29 shows the spatially averaged top thermocouples from FDS and experimentation (i.e. thermocouples A3, B3, C3, D3). HGL temperatures of the 13 kW and 50 kW agree well, however the 20 kW test shows temperature differences at approximately 100 °C. The net heat transfer the tube wall is now due to convective and radiative heat transfer

$$q''_{net} = q''_{conv} + q''_{rad} \tag{2.8}$$

where $q"_{conv}$ and $q"_{rad}$ are the convective and radiative heat flux per unit area. The convective heat transfer to the tube is described as

$$q''_{conv} = h_{out}(T_{HGL,t} - T_{wall,t}) \tag{2.9}$$

where h_{out} is the heat transfer coefficient on the outside of the tube, $T_{HGL,t}$ is the FDS HGL temperature with time, and $T_{wall,t}$ is the tube wall temperature with time. The radiation heat transfer to the tube is then described by the following

$$q''_{rad} = \epsilon_{flame}\sigma F_{12}(T^4_{flame} - T^4_{wall,t}) - \epsilon_{wall}\sigma(1 - F_{12})(T^4_{wall,t} - T^4_{sur}) \tag{2.10}$$

The first term on the right hand side represents heat transfer to the tube wall where ϵ_{flame} is the emissivity of the flame, σ is the Boltzmann constant, F_{12} is the view factor between the tube wall and the flame, and T_{flame} and T_{wall} are the flame and wall temperatures respectively. The second term on the right hand side represents radiative losses from the tube where ϵ_{wall} is the emissivity of the tube and T_{sur} is the temperature of the surroundings.

The tube sub-model was run with two different heat transfer models to the working fluid for the 13 kW, 20 kW, and 50 kW cases. In the first heat transfer model, heat transfer to the fluid is assumed to be convective and the change in fluid temperature was described previously by Equation 2.5. The second heat transfer model assumes that heat transfer to the fluid is conductive with an adiabatic boundary condition at $r = 0$. Ignoring axial and tangential conduction, conduction into the tube is described by

$$\frac{\partial T_{fluid}}{\partial t} = \frac{k_{fluid}}{\rho_{fluid} c_{fluid}} \frac{\partial^2 T_{fluid}}{\partial r^2} \tag{2.11}$$

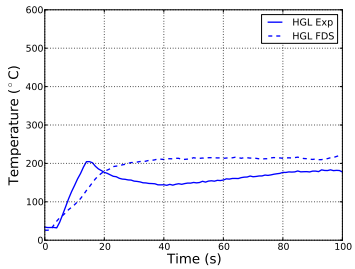

(a) 13kW case

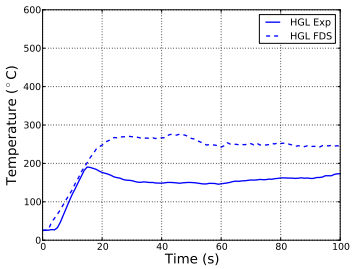

(b) 20kW case

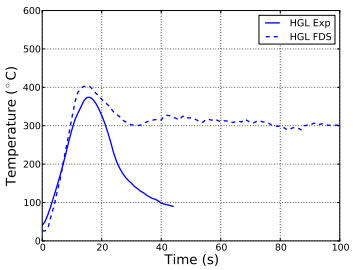

(c) 50kW case

Figure 2.29: Spatially averaged top thermocouple temperatures from experiment and FDS

where ρ_{fluid} and c_{fluid} are the density and specific heat respectively, and k_{fluid} is thermal conductivity of the fluid presented in Subsection 2.2.5.1. An implicit finite volume method is used to solve for the conductive heat transfer radially into the tube. A Bayesian parameter inference was used to propagate the input distributions shown in Table 2.6 and Table 2.7 through the sub-model in order to find the best values of h_{out}, F_{12}, and h_{in} given the experimental data. Ten thousand realizations were ran of which the first seven thousand were burned. For more information on Bayesian parameter inference, Overholt presents a complete discussion in his dissertation on *Forward and Inverse Modeling of Fire Physics Towards Fire Scene Reconstructions* [37].

The values from the Bayesian parameter inference for the convection case is shown in Table 2.6. The mean values for h_{out}, h_{in}, and F_{12} for the 13 kW case are 3 W/m^2-K, 5 W/m^2-K, and 0.008 respectively. For the 20 kW case, the mean values

Table 2.6: Convection model calibration inputs

Parameter	Distribution	Lower Value	Upper Value
Outside Heat Transfer Coefficient (W/m^2-k)	Uniform	0	200
Inside Heat Transfer Coefficient (W/m^2-k)	Uniform	0	100
View Factor	Uniform	0	1

Table 2.7: Conduction model calibration inputs

Parameter	Distribution	Lower Value	Upper Value
Outside Heat Transfer Coefficient (W/m^2-k)	Uniform	0	200
View Factor	Uniform	0	1

for h_{out}, h_{in}, and F_{12} are 2 W/m^2-K, 78 W/m^2-K, and 0.025 respectively. The mean values for h_{out}, h_{in}, and F_{12} for the 50 kW case are 13 W/m^2-K, 52 W/m^2-K, and 0.204 respectively. As a means for comparison typical natural convection values for the heat transfer coefficient range between 5 W/m^2 and 25 W/m^2.

The values from the Bayesian parameter inference for the conduction case is shown in Table 2.7. The mean values for h_{out} and F_{12} for the 13 kW case are 8 W/m^2-K and 0.004 respectively. For the 20 kW case, the mean values for h_{out} and F_{12} are 14 W/m^2-K and 0.005 respectively. The mean values for h_{out} and F_{12} for the 50 kW case are 23 W/m^2-K and 0.394 respectively.

Table 2.10 shows the two different heat transfer models run using the Bayesian inference scheme. The first column represents the convection cases with experimental and sub-model tube wall temperatures along with fluid temperatures (in blue). The

Table 2.8: Bayesian parameter inference results for the outside heat transfer coefficient, inside heat transfer coefficient, and view factor for the convection cases

Fire HRR (kW)	h_{out} (W/m^2-K)	Standard deviation (W/m^2-K)	h_{in} (W/m^2-K)	Standard deviation (W/m^2-K)	F_{12}	Standard deviation
13	3	1	5	4	0.008	0.001
20	2	2	78	17	0.025	0.005
50	13	8	52	28	0.204	0.013

Table 2.9: Bayesian parameter inference results for the outside heat transfer coefficient and view factor for the conduction cases

Fire HRR (kW)	h_{out} (W/m^2-K)	Standard deviation (W/m^2-K)	F_{12}	Standard deviation
13	8	3	0.008	0.005
20	14	2	0.005	0.005
50	23	16	0.394	0.026

second column shows the conduction case experimental and sub-model tube wall temperatures. The temperature increase of the fluid for the 20 kW convection case is more pronounced than the other two cases. While the Bayesian inference approach is able to match sub-model temperatures to experimental temperatures, some non-physical results occurred. It would be expected that outside heat transfer coefficients should be higher than what the sub-model was predicting. For both the 13 kW convection and conduction cases, unrealistically low heat transfer coefficients and view factors were observed. This was also the case for the outside heat transfer coefficient for the 20 kW convection case. The 20 kW conduction case view factor was also very low. Large standard deviations for the inside heat transfer coefficient for all the

convection cases was observed. Different distributions for the inverted parameters or a uniform distribution with tighter bounds could be propagated through the sub-model to obtain more realistic results for the heat transfer coefficients and view factors.

Table 2.10: Model Results

Fire HRR	Convection	Radial Conduction
13 (kW/m^2)	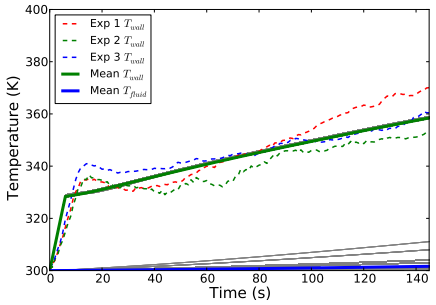	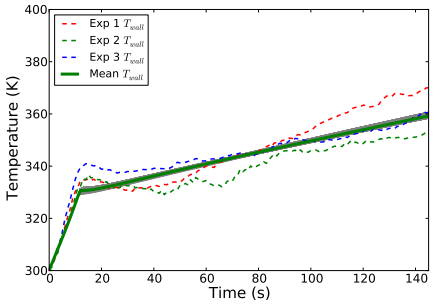
20 (kW/m^2)	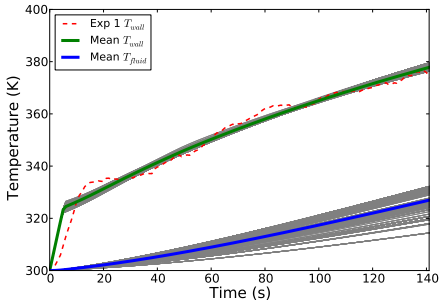	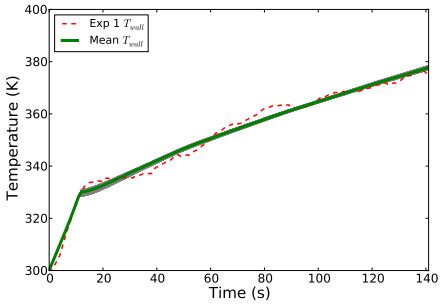
50 (kW/m^2)	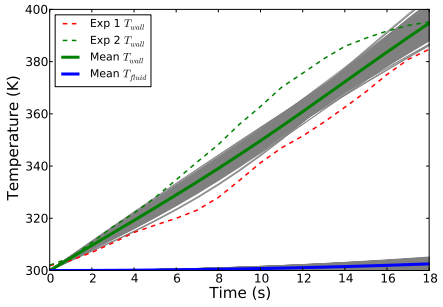	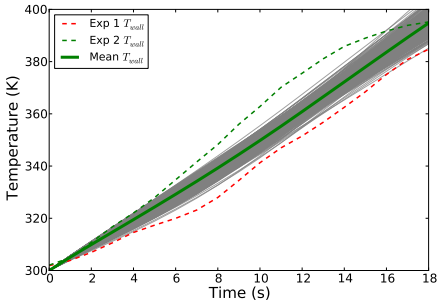

2.3 Glove Experiments

It is useful to develop simple models to approximate complex multi physics problems. Standardized testing of materials have been used for some time now and simple models have been developed to address events such as ignition time for a given external heat flux, heat release rate of a given material, etc. LANL wanted to ensure that the Fire Foe™ fire suppression system would activate before the glovebox could be breached by degradation of of the glovebox gloves. In this section, bench scale tests of thermal degradation of Hypalon® Glovebox Gloves by North provided by LANL are discussed. Hypalon® is the trade name of chlorosulfonated polyethylene, an elastomer developed by DuPont. Micro combustion calorimetry (MCC) was used to determine heat of combustion of the material, and time to ignition tests were run to find ignition time versus incident heat flux. Using standard ignition time models, effective model parameters were calibrated.

2.3.1 Experimentation

2.3.1.1 Micro Combustion Calorimetry

Micro combustion calorimetry (MCC) is one of many bench scale tests to assess some of a materials thermal and fire properties. Three different samples were prepared for the MCC tests. The sample masses were 7.0 mg, 5.9 mg, and 7.6 mg for each of the three samples respectively. MCC tests were run to determine the peak heat release rate (HRR), the heat release (HR) capacity or the ratio of the peak heat release rate normalized by the heating rate, and the total heat released (HR) [38]. A microscale combustion calorimeter Model MCC 2, Govmark Organization, Inc. was used to obtain peak HRR and other data for the MCC samples. There was no variation in test parameters for the MCC tests. Results of the MCC tests are in the results section.

2.3.1.2 Time to Ignition

Time to ignition tests were conducted on a total of six 100 mm by 100 mm glove samples at different heat fluxes. Kaowool insulation was used as backing during testing. A single K-type thermocouple was placed between the sample and backing material to measure the sample temperature at ignition. Details of the details are shown in Table 2.11. In Fig. 2.30 three of the samples are shown. The first sample is a sample before testing. The second sample was tested in the mass loss calorimeter at 60 kW and was not ignited. The third sample shows a test specimen tested at 60 kW with ignition after testing of the material.

Table 2.11: Test matrix and sample properties for time to ignition tests

Test No.	Coil Temperature (K)	Heat Flux (kW)	Specimen Width/Length (mm)	Specimen Thickness (mm)	Mass (g)
1	1014	60	100	0.76	9.51
2	1014	60	100	0.76	9.4
3	969	50	100	0.75	9.02
4	969	50	100	0.80	10.15
5	852	40	100	0.83	9.85
6	852	40	100	0.79	9.98

A mass loss calorimeter, Fig. 2.31 adhering to the ASTM E1345 standard for construction/assembly was used to get time to ignition data for the glovebox glove samples [39]. The mass loss calorimeter consisted of an Omega CN 8240 temperature controller to control the temperature of the heating coil, a heating coil provided by ASB heating, and a FIT Loadcell by HBM [31]. A Samsung Galaxy SII was used as a stopwatch to keep track of experimental time and a pilot flame was placed near the sample during testing. The temperature of the coil to obtain the necessary heat flux

Figure 2.30: Ignition test samples. From top to bottom: untested, 60 kW no ignition, 60 kW after ignition

was approximated by

$$T_{coil} = [\frac{Q}{\epsilon\sigma}]^{1/4} \tag{2.12}$$

where T_{coil} is the temperature of the coil, Q is the sought after heat flux to the sample, ϵ is the emissivity (assumed one in this case), and σ is Boltzmann constant.

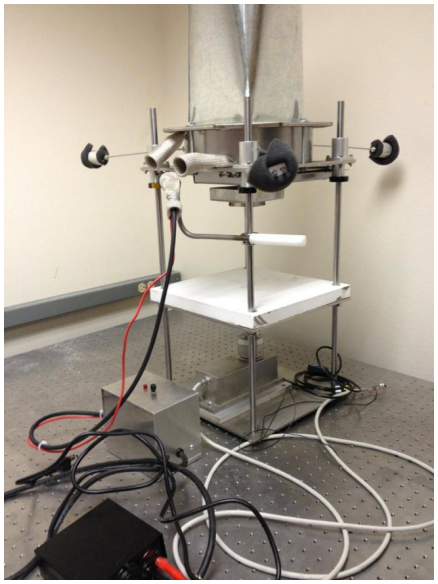

Figure 2.31: UTFRG Mass loss calorimeter

2.3.2 Ignition Model

2.3.2.1 Model Equations

Two different ignition models were considered: thin ignition model that models the ignition of a material assuming thin behavior and a thick ignition model that models the ignition of a material assuming thick behavior. Thin behavior suggests that there is no temperature gradient across the sample, the backing is assumed to be adiabatic, and losses via convection are ignored [1]. A material is assumed thin when the Biot number is small. Thin ignition is modeled as

$$t_{ign,thin} = \rho c_p d \frac{T_{ign} - T_0}{q"_{ext}} \tag{2.13}$$

where $t_{ign,thin}$ is the ignition time for a specified $q"_{ext}$ of the mass loss calorimeter heating coil, ρ, c_p, and d are the density, specific heat, and thickness of the sample respectively. T_{ign} is the ignition of the surface at $t_{ign,thin}$, and T_0 is the ambient

temperature.

Thick behavior suggests that the solid is infinitely thick, i.e. the thermal wave does not completely penetrate the solid. Losses due to convection are again ignored [1]. Thick ignition is modeled as

$$t_{ign,thick} = \frac{\pi}{4} k\rho c_p [\frac{T_{ign} - T_0}{q"_{ext}}]^2 \tag{2.14}$$

where $t_{ign,thick}$ is the ignition time for a specified $q"_{ext}$ of the mass loss calorimeter heating coil, k is the thermal conductivity, ρ is the density, and c_p is the specific heat. T_{ign} is the ignition of the surface at $t_{ign,thick}$ and T_0 is the ambient temperature.

2.3.3 Results

2.3.3.1 Micro Combustion Calorimetry

The results of the MCC tests are shown in table 2.12 of the Hypalon® glove material. The total heat release average was 16.66 kJ/g. Lin, et. al. reports for various non-halogenated thermoplastics total heat releases between 12.3 kJ/g and 20.9 kJ/g [40]. The heat capacity is about 229 J/g-k. The heat capacity for polyethylene is between 183 and 230 J/g-k [41].

Table 2.12: Micro combustion calorimetry tests and results

Test No.	Sample mass (mg)	Heat Release Capacity (J/g-k)	Peak HRR (W/g)	Total HR (kJ/g)
1	7.0	229	232.2	17.2
2	5.9	234	233.7	15.8
3	7.6	226	229.6	17.0

2.3.3.2 Time to ignition

Measured time to ignition and temperature of ignition values are reported in Table 2.13. During testing of the first 60 kW test thermocouple under the sample fell out, therefore that value of T_{ign} is not presented. Ignition was originally thought to be thin but after analysis of the data, thick behavior was observed. It is believed that the insulating material beneath the samples is not acting as a good insulator. Conduction heat transfer may be continuing from the sample to the insulation underneath. For this reason calibration of the parameters in Eq. 2.13 was ignored and calibration of the parameters in Eq. 2.14 were considered. More information on model calibration is presented in the next section.

Table 2.13: Ignition test results

Test No.	Heat Flux (kW)	t_{ign} (s)	T_{ign} (°C)	T_{amb} (°C)
1	60	151		23
2	60	174	327	23
3	50	253	324	23
4	50	233	355	23
5	40	315	305	23
6	40	458	302	23

2.3.3.3 Thick Ignition Model Calibration

Model calibration of the parameters in the Eq. 2.14 was not done in the conventional fashion of creating a polynomial curve fit and choosing the most likely k, ρ, c_p, and T_{ign} for the material and testing conditions such that the polynomial lines up with the data. Instead simple distributions, bounds are shown in Table 2.14, were used to represent values of k, ρ, c_p, and T_{ign}. A Bayesian parameter inference was used to propagate the distributions through the thick ignition model in order to find

the best values of k, ρ, c_p, and T_{ign} given the experimental data and thick ignition model [42]. One hundred thousand realizations were ran of which twenty thousand were burned.

Table 2.14: Model calibration inputs

Parameter	Distribution	Lower Value	Upper Value
Thermal Conductivity (W/m-K)	Uniform	0.7	7
Density (kg/m^3)	Uniform	500	1500
Specific Heat (J/kg-K)	Uniform	500	1300
Ignition Temperature (°C)	Uniform	250	700

The results of the model calibration process are shown in Table 2.15 and plotted in Fig. 2.32. The blue squares in Fig. 2.32 are the experimental data, the bold green line in the figure represents the thick ignition model, Eq. 2.14, evaluated at the mean values of k, ρ, c_p, and T_{ign}, Table 2.15. The gray bands surrounding the curve represent 95% credible intervals. Given the data and the thick ignition model with the values of k, ρ, c_p, T_{ign}, and $q"_{ext}$ one can predict t_{ign} with 95% confidence [42]. As a point of reference to the values presented in Table 2.15, values for k, ρ, c_p, and T_{ign} of polyethylene are 4.2 W/m-k, 940 kg/m^3, 215 J/kg-k, and 443 °C respectively [41]. The values in Table 2.15 are not too close, especially the specific heat, to the values of polyethylene because they do not exactly represent the material properties of the Hypalon® glove material alone. The best fit values represent the effective k, ρ, c_p, and T_{ign} of the experimental setup and conditions.

2.4 Conclusions

Fire Foe™ activation tests were conducted within an instrumented glovebox. FDS was used to simulate the thermal environment around the suppression system.

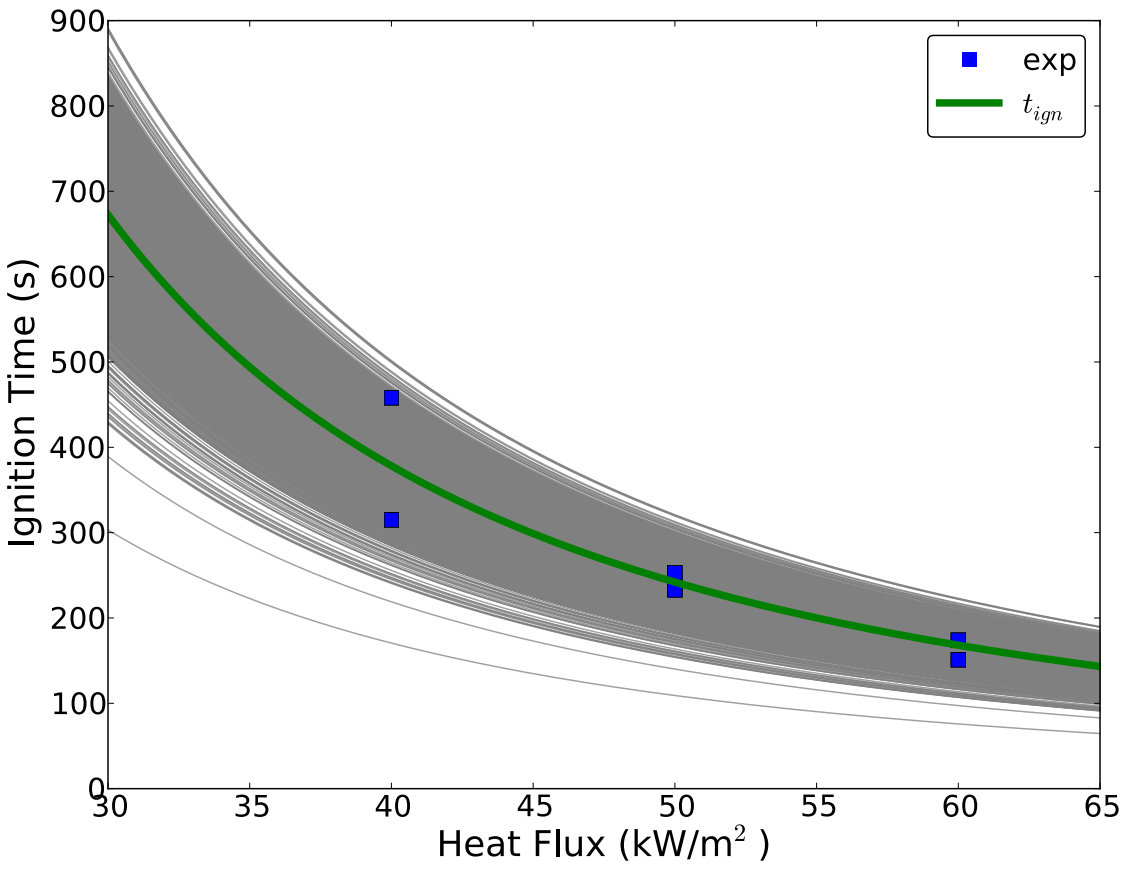

Figure 2.32: Best fit to thick ignition for data observed

FDS tended to overpredict gas temperatures overall for the 13 kW, 20 kW, and 50 kW tests with an average of 10%, 32%, and 20% respectively. Gas temperatures for the 25 kW tests were underpredicted with an average of 14%. More stratification in the experimental temperatures was also observed when compared to the FDS gas temperatures. This may be attributed to higher gas phase mixing in the FDS model than what actually occurred in experimentation. For the 13 kW, 20 kW, and 50 kW tests, FDS tended to underpredict Fire Foe^{TM} wall temperatures overall. The semi-empirical sub-model that was coupled to FDS tends to overpredict activation time

Table 2.15: Model calibration results

Parameter	Mean	Standard Deviation
Thermal Conductivity (W/m-K)	4.627	1.522
Density (kg/m^3)	1031.3	281.0
Specific Heat (J/kg-K)	903.8	232.6
Ignition Temperature (°C)	486.1	104.6

at higher heat release rates, shorter activation times, and underpredict at lower heat release rates, longer activation times and tended to overpredict activation time overall by 34%. The current sub-model does not capture the physics of Fire Foe^{TM} well. A greater understanding of material failure under high pressures and temperatures is required to understand the physics leading up to Fire Foe^{TM} activation. A Bayesian parameter inference was applied to two different models with unrealistic results at the 13 kW and 20 kW cases.

Thermal characterization of the glove material showed that the heat of combustion found from MCC was within the range of heats of combustion for other non-halogenated materials found in the literature. Time to ignition tests showed that the glove material was behaving thickly. This was most likely due to experimental setup. The Bayesian parameter inference yielded thermo-physical properties for the coupled glove material degradation experimental setup which do not necessarily represent the true thermo-physical properties of the glove material.

Chapter 3

Dry Water: Delivery for Fire Suppression

3.1 Introduction

This chapter describes prototype development and testing of a dry water delivery system. Following the discussion on dry water delivery, prototype development focused on the development of a continuous dry water production system will be discussed. For all cases dry water was made using one part by mass *Aerosil ® R812S* hydrophobic fumed silica of nominal particle size of 7 nm and nineteen parts by mass water. The dry water could not be flowed easily to make a simple comparison to water mist systems, see Appendix A. Attempts to flow premade dry water resulted in water release. The next section outlines attempts to flow dry water continuously for fire suppression applications.

3.2 Dry Water Delivery Prototypes

As a first trial run for delivering dry water, a syringe was loaded and depressed into a small pan to test if dry water could be easily dispensed, shown in Figure 3.1. Upon further investigation of the delivered dry water, it was noticed that water had been released from the dry water particles. In the dish that the dry water was depressed into, small liquid marbles (macroscopic droplets of water surrounded in hydrophobic silica) were observed. It was believed that as the dry water passed through the small opening at the end of the plunger, the high shear stresses caused by a high flow rate through a small orifice caused the water to to be released forming

these liquid marbles.

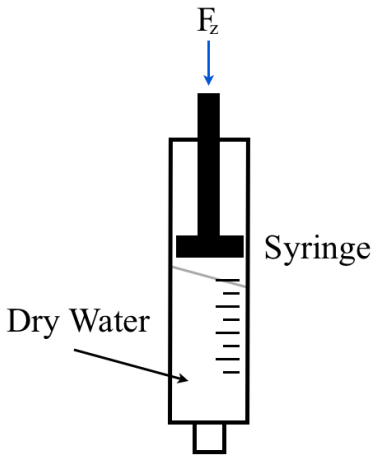

Figure 3.1: A syringe was first used to attempt to flow dry water.

Another idea that was tested was assembling a plunger setup (see Figure 3.2). Because it was assumed that forcing the dry water through a small orifice caused water release, a large diameter plunger with a breakable membrane was used. For the trial case a thin sheet of Kimtech Kimwipes was used as the membrane. A 3.8 cm diameter PVC pipe was used as the housing, and a cardboard cutout was used as the actual plunger. A force into the plunger was used to create the force necessary to compress the dry water, break the membrane, and deliver the dry water. Upon depression of the plunger, however, the dry water was not delivered as expected. Much of the water within the dry water had absorbed into the Kimwipe and the cardboard cutout. It was therefore concluded that the dry water could readily be transported out of the encapsulations and into a porous median.

Because high normal and shear stresses cause the water release in the dry water, other means of delivering the dry water had to be developed. Figure 3.3 shows a schematic of using dry water placed atop a mesh screen. Attached to the apparatus

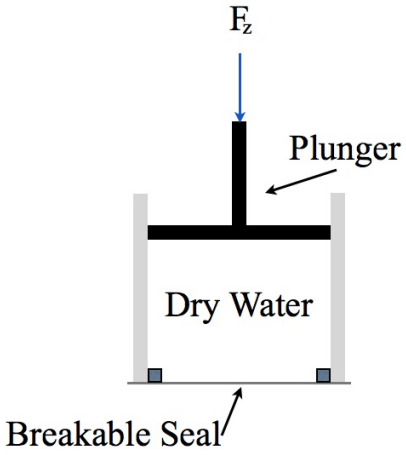

Figure 3.2: Schematic of a plunger used to attempt to deliver dry water

is a vibrating motor meant to agitate the dry water. A prototype was constructed and tested, however, the oscillations were too small to effectively deliver the dry water.

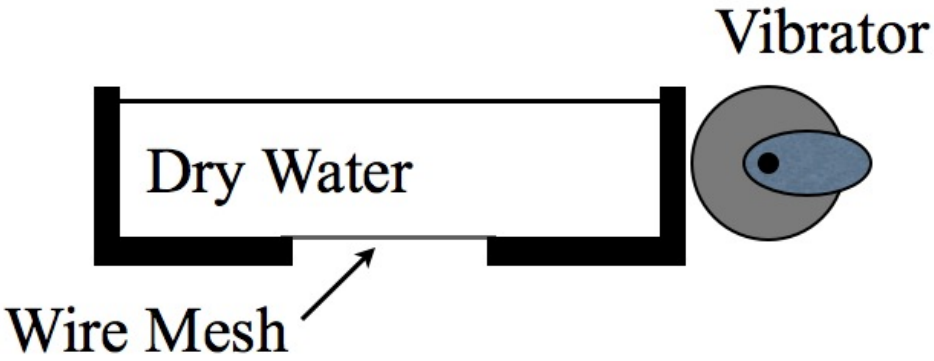

Figure 3.3: Schematic of using a vibrating motor to deliver dry water

Taking inspiration from the previous idea, a different kind of agitator was proposed, Figure 3.4. A wire mesh cage was used to store the dry water until it needed to be dispensed. At the time of dispensing, a motor would activate causing

the cylindrical wire mesh cage to rotate. The dry water would tumble and flow through the small openings in the wire mesh. While this idea had some promise, it proved to be an ineffective way to deliver the dry water. The spread and the flow of dry water were random and discontinuous.

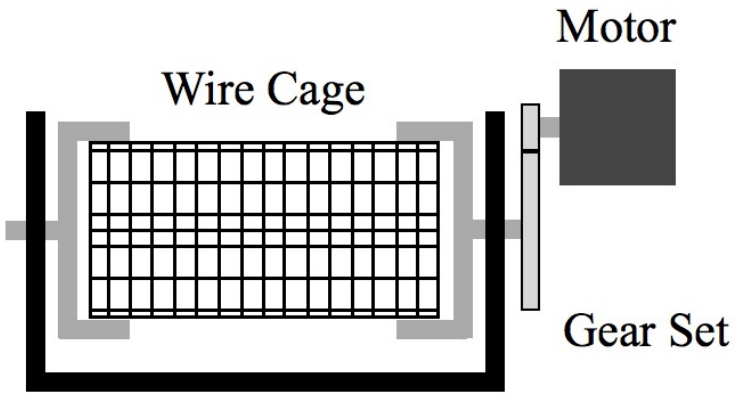

Figure 3.4: Schematic of a rolling, agitating cage used to deliver dry water

Figure 3.5 shows another of the ideas attempted to fluidize and deliver the dry water. For this, a small amount of dry water is placed near the inlet of the air stream. The incoming air is meant to fluidize the dry water and the shape of the apparatus is meant to induce swirl in the flow. The dry water was meant to flow out akin to precipitation. However the amount of dry water that was able to be flowed was too little to put out even a small pool fire. For this reason the idea was abandoned.

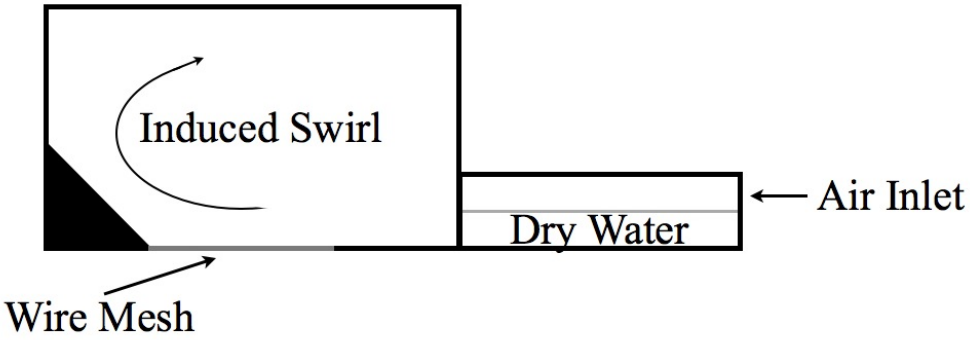

Figure 3.5: Schematic of an apparatus used to fluidize dry water

In order to attempt to flow the dry water through a nozzle without inducing large stresses on the dry water, another idea was formulated. Figure 3.6 shows a schematic of this idea. The dry water was placed into a rigid polystyrene cylindrical container of 4.8 cm inside diameter and a height of 9.4 cm. Shop air was flowed into the rigid container at pressures less than 5 psi to get the dry water flowing. A nozzle with orifice 1.778 mm was placed at the bottom of the container to spread the flow of the dry water, similar to water mist/sprinkler nozzles. While this seemed promising at first, when the air was flowed into the container, a phenomenon known as the *ratholing effect* caused only a small amount of the dry water to flow, Figure 3.7.

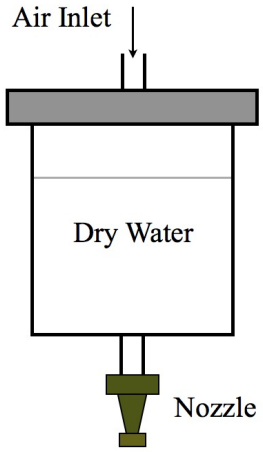

Figure 3.6: Schematic of dry water delivery mechanism using a rigid container

To avoid ratholing, inspiration was taken from baby bottles with bottle liners to isolate the air flow and the dry water. As shown in Figure 3.8, a rigid container is pressurized such that there is a constant pressure on the flexible membrane that is greater than atmospheric and would cause the dry water to flow through the nozzle as the membrane deforms. However this idea also proved to be ineffective. The dry water did not flow as expected.

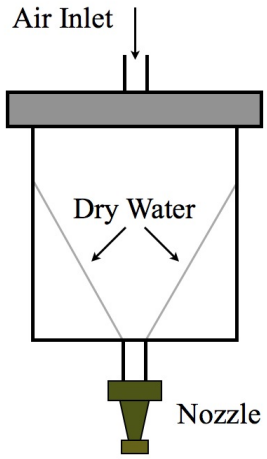

Figure 3.7: The ratholing effect causes the air flow to short circuit

In another effort to avoid ratholing, small diameter tubing of inner diameter 0.635 cm was used to store the dry water. Spheres of diameter 0.48 cm were placed atop the dry water and this network of tubes was connected as shown in Figure 3.9. The tubes with the lowest resistance would empty first. Upon emptying the beads would block the flow of air ensuring that a short circuit does not occur. This greatly increases the flow resistance in the local tube to a value much higher than that of tubes that have yet to empty. This ensures that the other tubes that may have had higher resistances empty. The setup was connected to a nozzle of orifice diameter 1.778 cm. This apparatus showed great promise in delivering dry water.

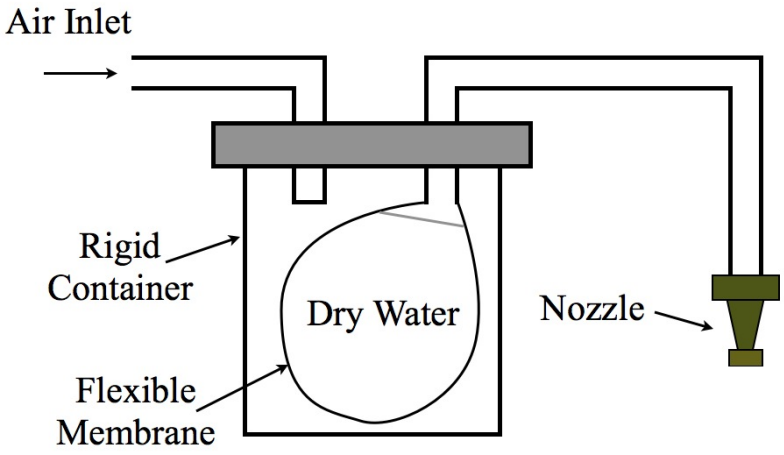

Figure 3.8: Schematic of the attempt to flow dry water using a flexible membrane

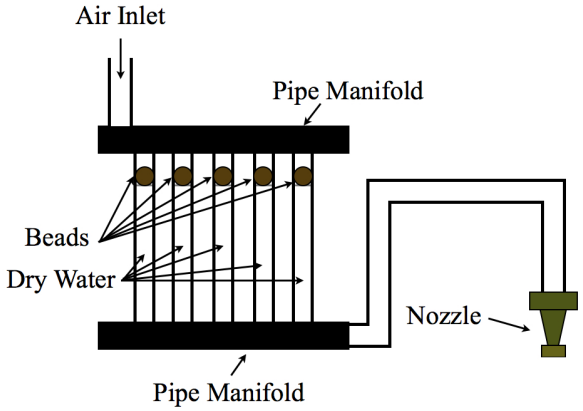

Figure 3.9: Schematic of a successful dry water delivery mechanism

3.3 Development of a Continuous Dry Water Production System

Generally, dry water is made in a batch process, as mentioned in Chapter 1. While dry water is stable when stored in the high humidity confines of a container, when left exposed to dry air, the water will readily evaporate out of the silica encapsulations. It was decided that creating a continuous production system would help mitigate the potential for water to destabilize. The development of a continuous system is outlined below.

3.3.1 Components and component characterization

We first explored flowing dry water directly out of the blender during operation. Two holes were drilled on opposite sides of the blender container and two quarter inch outer diameter pipe fittings were attached to the blender container, Figure 3.10. One side of the blender was connected to shop air through an SMC regulator, and the other side was connected to a nozzle. A single normal batch of dry water was made in the blender with no airflow. At 30 s when the blender would normally be turned off, the blender was allowed to continue operation and shop air was introduced to the blender. Observing the outgoing stream indicated that the ratio of dry water to air was low and needed to be measured.

To measure the ratio of dry water to air the previous configuration was maintained except that the outgoing stream was connected to an evacuated plastic bag. The plastic bag had a known fully expanded volume of 946 cm^3. The dry water was created as before and the air/dry water mixture was flowed into the plastic bag until it was completely full, Figure 3.11. The bag was sealed and weighed on a load cell to find the final mass. The mass of the air was neglected in calculating the mass of the dry water. The dry water mass was found by subtracting the final mass of the

Figure 3.10: Blender with quarter inch outer diameter pipe fittings

bag from the initial, empty mass of the bag. The mass of the dry water deposited in the bag was found to be 1.2 g. In calculating the mass of the air, the full volume of 946 cm^3 was used and multiplied by the density of air at room temperature, 0.012 g/cm^3. The volume of the dry water in the bag was neglected because it accounted for only about 0.3 % of the total volume. The mass of air in the bag was found to be 11.3 g and the ratio of dry water to air was found to be about 10 %. Because of the low dry water to air ratio a means to separate the dry water from the air needed to be developed.

In looking for a way to separate the air and dry water, a cyclone separator was investigated. Gas cyclone separators have been used in industry for many years to separate particles from an air stream. Patents for the cyclone separators can date back to the early 20th century [43]. Figure 3.12, shows a schematic of the type of cyclone used to separate the air from the dry water. The cyclone was constructed out of a polystyrene cylindrical jar and a polyethylene truncated cone. Dimensions of the cyclone separator are shown schematically in Figure 3.13 and Table 3.1. Pipe

Figure 3.11: Bag used to measure the ratio of air to dry water

fittings were attached to the separator as shown in Figure 3.14. Dry water flow from the cyclone was tangential.

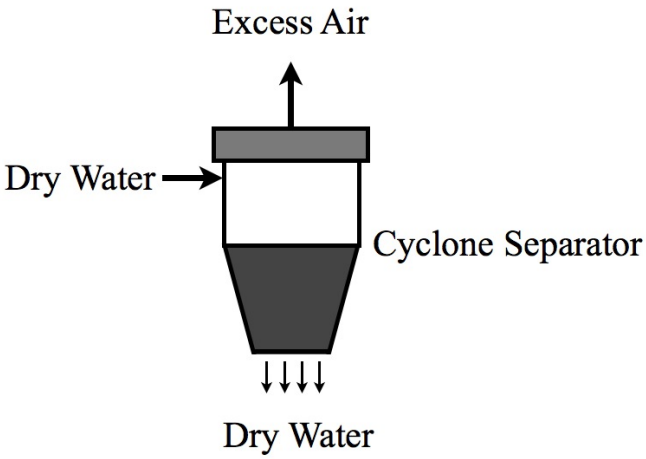

Figure 3.12: Schematic of cyclone separator

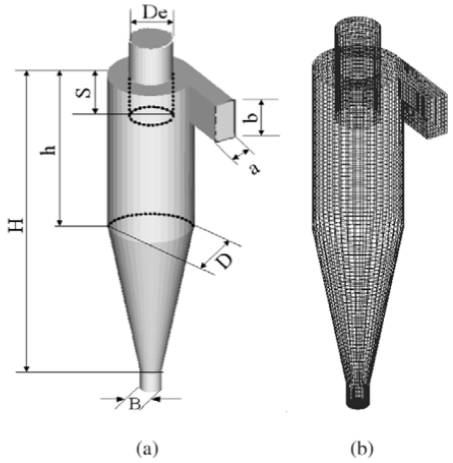

Figure 3.13: Cyclone geometry, taken from [2]

Table 3.1: Geometry of cyclone separator of D=5 cm

a/D	b/D	De/D	S/D	h/D	H/D	B/D
0.13	0.13	0.13	0.2	0.9	1.6	0.6

Figure 3.14: Pipe fittings for cyclone separator

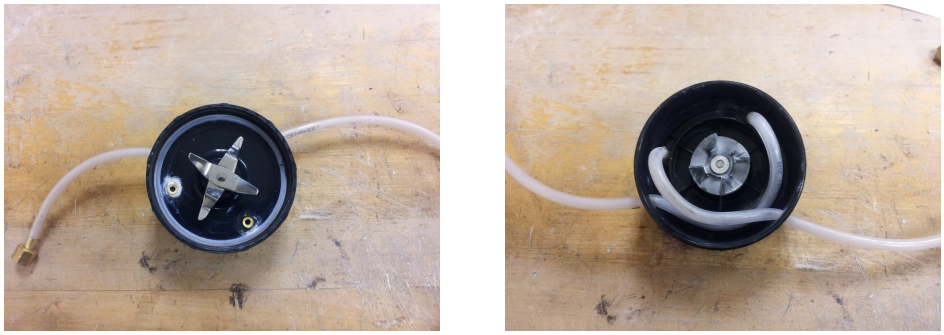

Figure 3.15: Modified blender which allows water and silica to flow into it

The blender used for producing dry water was also modified to allow flow of water and silica in through the bottom, Figure 3.15. To flow water into the blender, a small reservoir was made and the water flow rate was controlled using a Keys Instrument rotameter, Figure 3.16. To flow the silica into the blender bottom a number of ways were attempted. The first, Figure 3.17, involved using a syringe to flow the silica in to the blender bottom. However, the silica particles coated the rubber flange in the syringe making it too difficult to depress. The idea was abandoned and it was decided that the silica was to be fluidized before entering the blender.

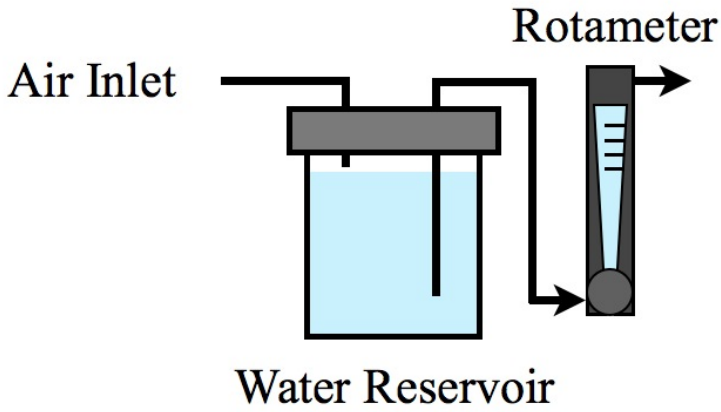

Figure 3.16: Schematic of water reservoir used to flow water into the blender

Figure 3.17: A syringe was first proposed as a means to deliver silica to the blender.

An agitating seeder was first proposed as a means to fluidize the silica, Figure 3.18. Silica was stored in the top portion of the seeder and a brush of diameter 3.8 cm was used as the agitator. The brush center was offset by 0.3 cm and the brush was rotated using a Crafstman Industrial 4.5 amp electric drill connected to a variable transformer. The housing for the seeder was created out of acrylic and held together with epoxy. Pipe fittings were attached to either end of the seeder such that it could be connected to the lab air line. Figure 3.19 shows the seeder, water reservoir, and cyclone connected to the blender. Characterization of the agitating seeder was attempted by varying the air flow into the seeder and the rotational speed of the brush. The agitating seeder concept, however, did not perform consistently and was abandoned.

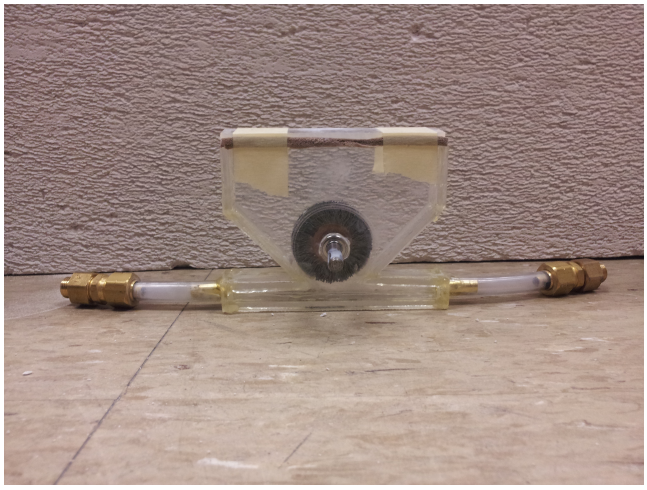

Figure 3.18: A rotating circular brush was originally used to fluidize silica.

Figure 3.19: Continuous dry water setup with the agitating seeder

To fluidize the silica, a percolating seeder was constructed, Figure 3.20. A hole of roughly one quarter inch was made in the bottom of a polystyrene container of diameter 4.8 cm and height 9.4 cm. One end of of the quarter inch outer diameter tubing was sealed with epoxy and a number small holes of diameter 0.16 cm were made in the tubing at a spacing of roughly a quarter inch. The tubing was run through the hole in the polystyrene container and bent to conform to the curvature of the container. The tubing was held in place with more epoxy ensuring that the small holes were not obstructed. The lid of the container was also fitted so that it could be connected to the blender.

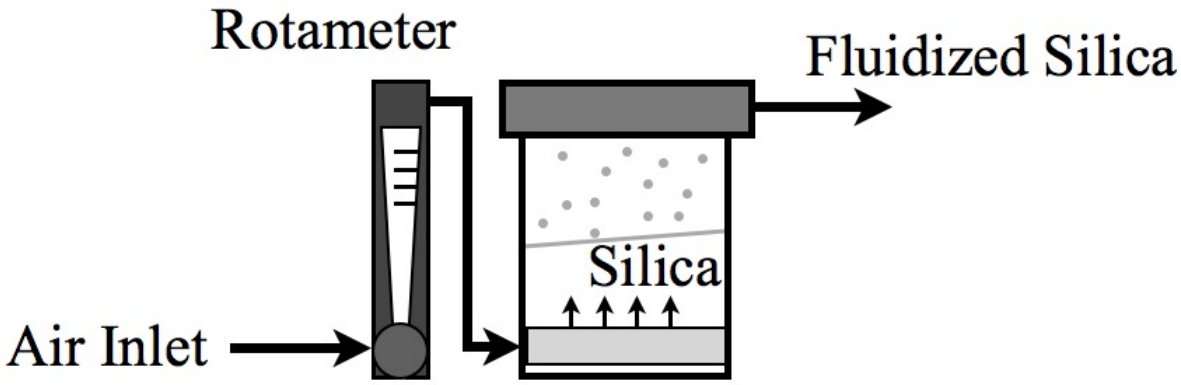

Figure 3.20: Schematic of a percolating seeder where air flows into a bed of silica for fluidization

To characterize the seeder, a Keys Instrument rotameter was used to control air flow into the seeder. To measure the flow rate of silica out of the seeder, 2 g of silica was transfered to the seeder, the seeder was closed and turned on at a specific air flow rate, $\dot{Q}_{air}$ for a set amount of time, Δt. The air was turned off, the remaining silica was emptied from the seeder and weighed. The mass flow rate of the silica from the seeder was therefore

$$\dot{m}_{SiO_2} = \frac{m_i - m_f}{\Delta t} \tag{3.1}$$

For each air flow rate, a total of 5 tests were conducted. Figure 3.21 shows how the silica mass flow rate varies with increasing air flow rate through the seeder for various air flow rates. It also shows the operation point of the seeder used for flow of 1 mL/s of water into the blender. The points indicate the average flow rate for the specified test and the error bars indicate the variation in the data and uncertainty in the air flow rate. At the highest flow rate, the variation in the mass flow rate of silica was about 40 times higher than the variation at the lowest flow rate.

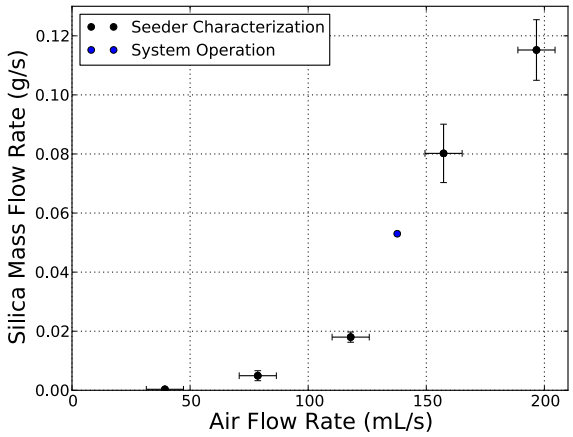

Figure 3.21: Seeder characterization

Carter et al. stated that the particle size of the dry water would vary with the blender blade rotational speed [18]. To characterize the rotational speed of the blender, it was connected to a variable transformer in series, Figure 3.22. Before characterization, the blender blades were removed, personal protective equipment was donned, and finally the safety mechanism on the blender was bypassed. A General Radio 1531-AB Strobotac strobe was used to characterize the rotational speed of the

blender as a function of the variable transformer setting, Figure 3.24.

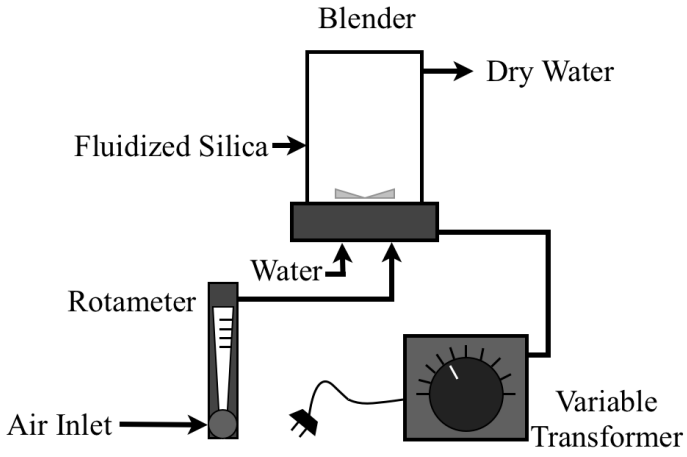

Figure 3.22: Schematic of blender with variable transformer

To obtain the rotational speed of the blender at a specific variable transformer setting, the strobe was adjusted until only a mark made on the blender appeared to stand still. To ensure that the actual rotational speed of the blender was being captured by the strobe and not a multiple of the rotational speed, the strobe speed was doubled and if two marks were observed on the blender, the previous measured rotational speed was correct. Figure 3.23 shows this schematically. The top two subfigures represent how the mark would look if the strobe were accurately recording the rotational speed. The bottom two subfigures show the doubled strobe speed and therefore the appearance of two marks on the blender.

With the components characterized, the continuous dry water system was assembled, Figure 3.25. An extra rotamter was attached to the blender to adjust the overall air flow into the blender. This ensured that the airflow through the cyclone was sufficient such that separation of the dry water occurred. A single air line was split and ran to the silica seeder, the water reservoir, and the excess air rotameter.

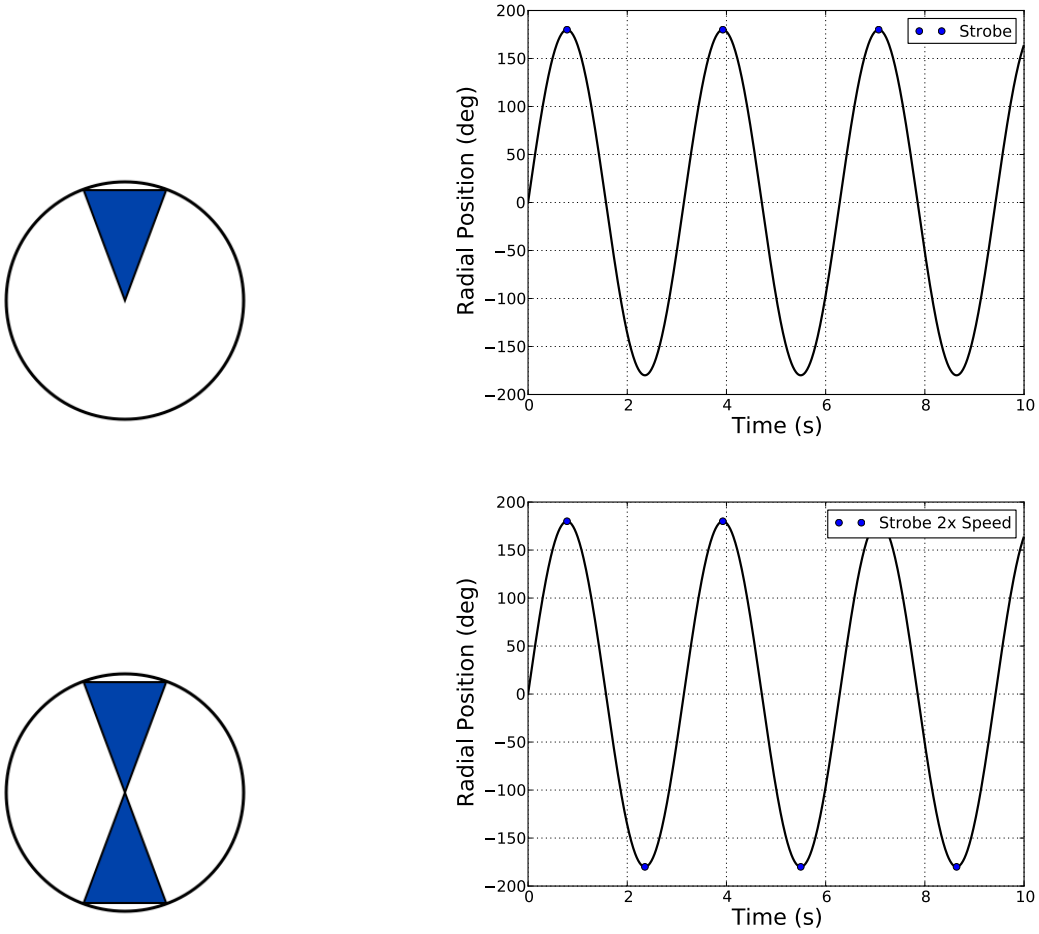

Figure 3.23: Rotational position of blender and strobe frequency

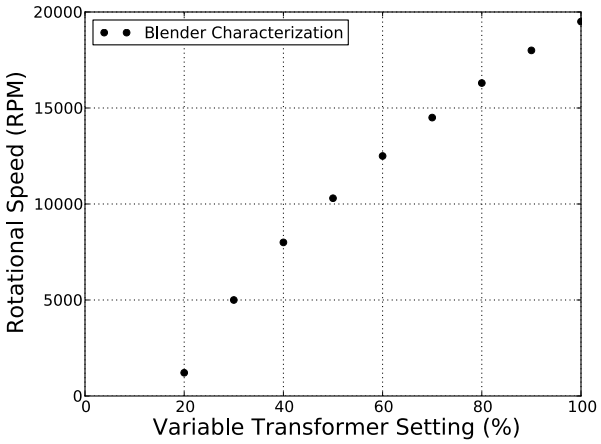

Figure 3.24: Rotational speed of blender plotted versus the setting on the variable transformer

These three components were then connected to the blender housing and the blender was connected to the variable transformer. The cyclone separator was also connected to the blender housing. The entire system was activated, the air supply was turned on at 10 psi and the blender turned on. The rotameters for the silica seeder, water reservoir, and excess air were then adjusted to the correct settings: 0.053 g/s, 1 mL/s, and 15 CFH respectively. Because this process took some time, the entire system was shut off, the water reservoir and the seeder were refilled, and the collected product from the cyclone was removed. The entire setup was once again turned on, and the settings of the rotameters were again verified. A characterization framework was setup to characterize the continuous and the batch dry water. The next section describes this framework in more detail.

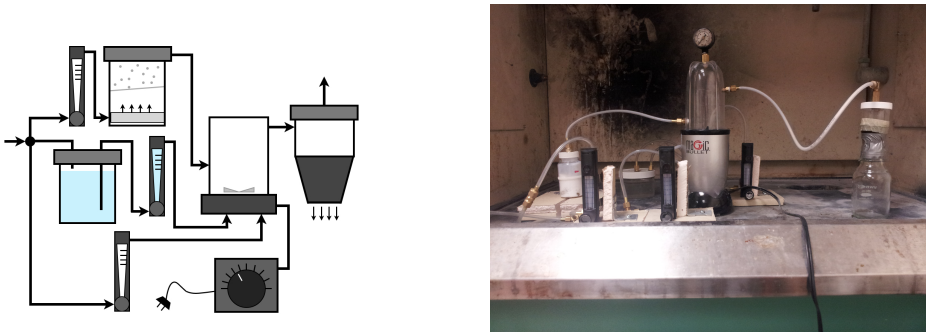

(a) Schematic (b) Experimental setup

Figure 3.25: Continuous dry water setup

3.4 A Framework for Dry Water Characterization

This section describes the methods used or could be used for characterization of dry water. First, macroscopic properties of the dry water will be analyzed. This includes density and mass loss of water. Second, micrographs and particle size distributions of the dry water will be presented. These properties were analyzed for the batch and continuous cases at different blender speeds.

3.4.1 Physical Characterization of the Dry Water

The density of the dry water for both the batch and continuous methods were measured by measuring the mass of a known volume of dry water blended at different rotational speeds. A set volume was marked off in an empty vial. The empty vial was weighed and it's mass was recorded. The vial was then filled with dry water up to the mark and then weighed again. The mass of the dry water was obtained by subtracting the empty vial mass from the filled vial mass. The density was then found by dividing the dry water mass from the measured volume. The procedure was confirmed by measuring the mass of a known volume of water and obtaining a density of 1 g/cm^3. The average densities are shown in Table 3.2. Binks and Murakami report densities of the dry water ranging from less than 0.3 g/cm^3 to 0.6 g/cm^3 [19].

Table 3.2: Dry water densities for various testing conditions

Batch or Continuous	Rotational Speed (RPM)	Density (g/cm^3)
Batch	12,500	0.40
Batch	16,300	0.45
Batch	19,500	0.53

Forny et al. used gravimetric analysis to gauge the quality of the dry water produced. It was expected that the mass of water going into the making the dry

Figure 3.26: Cyclone setup for collecting dry water via a laboratory filter for the batch (left) and continuous (right) cases

water should be similar to the mass of water evaporated from the dry water [17]. Similarly, mass loading of a filter was used to measure the characteristics of the dry water exiting the cyclone separator at a ratio of 19 parts by mass water, one part by mass silica. The filter setup was constructed of mainly PVC components, Figure 3.26. The cyclone separator was placed on top of the filter chamber and secured using duct tape. Directly below the separator a flange of 8.9 cm in diameter was used to house a Millipore 1 µm FA 8.9 cm laboratory filter. A piece of wire mesh was used to ensure that the filter did not deform greatly because of the pressure drop across it. The bottom of the filter setup was connected to a vacuum to ensure collection of the dry water particles.

To collect dry water for the batch cases, first an unloaded filter's mass,$m_{unloaded}$, was recorded before testing using a Denver Instruments TP-323 balance. The filter was then loaded into the filter setup, and then the dry water was allowed to blend at 19,500 RPM for 30 s. After 30 s had elapsed, a rotameter was used to flow 15 CFH of 10 psi air through the blender while it was operating for 10 s. At this time, the vacuum was also activated. The shop air and the vacuum were turned off simultaneously after 10 s had elapsed. The blender was powered off after a total of 45 s had elapsed. The filter was removed from the setup and its mass,m_{loaded}, was measured

again. The filter was allowed to dry and the final dried filter mass was measured, m_{net,DH_2O}. To find the net mass of dry water on the filter the following equation was used

$$m_{net,DH_2O} = m_{loaded} - m_{unloaded} \tag{3.2}$$

where m_{net,DH_2O} is the net mass of dry water collected, m_{loaded} is the mass of the loaded filter, and $m_{unloaded}$ is the mass of the unloaded filter pre-experiment. To find the net dried mass the following was used

$$m_{SiO_2} = m_{driedfilter} - m_{unloaded} \tag{3.3}$$

where m_{SiO_2} is the mass of silica left behind, $m_{driedfilter}$ is the mass of the dried filter, $m_{unloaded}$ is again the mass of the unloaded filter pre-experiment. To find the percentage of water loss from the loaded filter, the following equation was used

$$\%Water = \frac{m_{net,DH_2O} - m_{SiO_2}}{m_{net,DH_2O}} \cdot 100\% \tag{3.4}$$

The average percentage of water for the batch case was 93.1%.

For the continuous cases the flow of water to silica was held at 19:1 by mass. Water was flowed into the blender at 1 mL/s and silica at 0.053 g/s. The total amount of air flowing through the system was also maintained at around 15 CFH. The blender was first turned on and allowed to run empty for 5 s. The shop air and vacuum were activated simultaneously and allowed to run for a set amount of time before being deactivated. The filter was loaded and the mass loss of the water was measured in the same manner as that of the batch cases. Results from the tests are presented in Table 3.3.

Table 3.3: Filter loading mass loss for continuous case at 19,500 RPM

Test	Load Time (s)	% Water
1	10	1%
2		7%
3	30	85.0%
4		88.8%
5	60	95.1%
6		88.9%

From the filter loading cases, it was observed that water did not start flowing into the blender until roughly 10 s after shop air activation. This explains the approximately 1% water in the first mass loading experiment. As the system continuous to run, it was expected that the percentage of water would reach a roughly constant value according to the ratio of water to silica flowed into the system. This turned out to be the case and is shown in the tests 5 and 6 of the filter mass loading cases, Table 3.3.

3.4.2 Micrographs

To get micrographs of the dry water, the dry water had to be captured on top of a glass slide. For the batch process, the excess air rotameter and the cyclone were connected to the housing of the blender. The dry water was made normally with a 30 s blending time and a 19:1 ratio of water to silica. After 30 s had elapsed, air was flowed through the rotamter at 7.1 LPM. The air/dry water mixture was allowed to flow for 10 s before a slide was placed under the cyclone separator. Dry water at blending speeds of 12,500, 14,500, 16,300, 18,000, and 19,500 RPM was captured for both deionized water and tap water. At blending speeds below 12,000 RPM dry water cannot be formed. This appears in the literature and was also confirmed

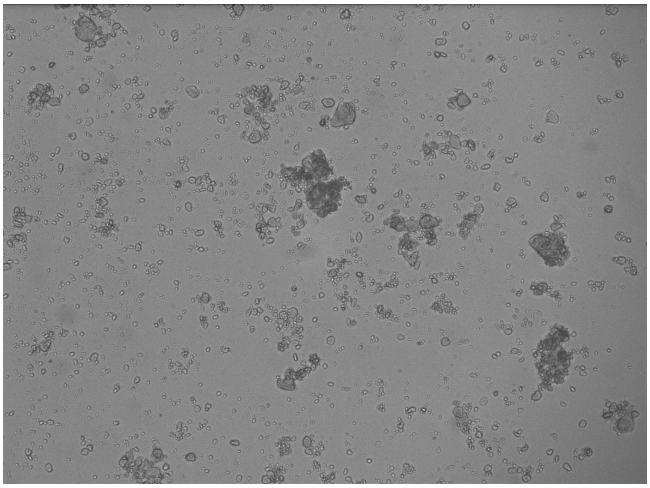

Figure 3.27: Silica aglomerates at 4x magnification

experimentally in our work [17]. A Nikon LV100 microscope was used to image the particles collected from the setup.

To differentiate between what could possibly be silica agglomerates in the dry water, a micrograph of unblended silica was taken (see Figure 3.27). Qualitatively, the silica agglomerates appear to obfuscate the microscope light less than the dry water, Figure 3.28. This was taken into account when the particle sizes were measured. In Figure 3.28 micrographs at 4x magnification of batch dry water blended at 12,500 RPM and 19,500 RPM are presented. There appear to be larger aggregates of dry water at the lower RPM case.

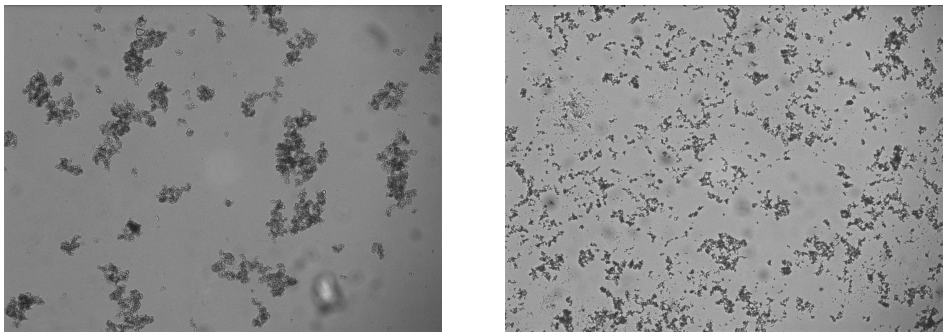

Figure 3.28: Batch dry water produced at a blender speed of (a) 12,500 RPM and (b) 19,500 RPM at 4x magnification

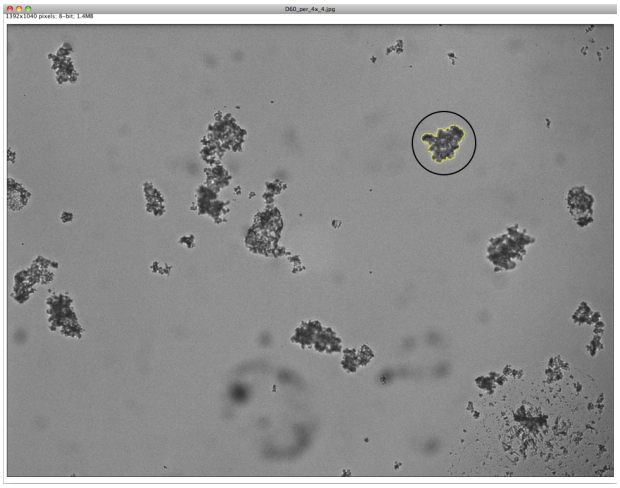

Figure 3.29: Traced particle, in yellow, for measuring purposes. Batch dry water made from tap water at 12,500 RPM

3.4.3 Histograms

Each dry water particle was encircled, Figure 3.29, and the area of the dry water particle in pixels was measured using ImageJ. Table 3.4 shows the conversion from pixels to micrometers at a given magnification specified by the supervisor of the Nikon LV100 microscope.

Measurements for particles sizes of the dry water was done after the water had already evaporated out of the encapsulations. This implies that actual particle sizes may have actually been larger because the collapsed clathrate sizes were measured. The dry water drying process was taken at 10 fps and is shown in the sequence of frames shown in Figure 3.30.

An equivalent diameter, d_{equiv}, was defined because the dry water particles were non-spherical. In solving for an equivalent diameter first the actual area of the particle in micrometers was found

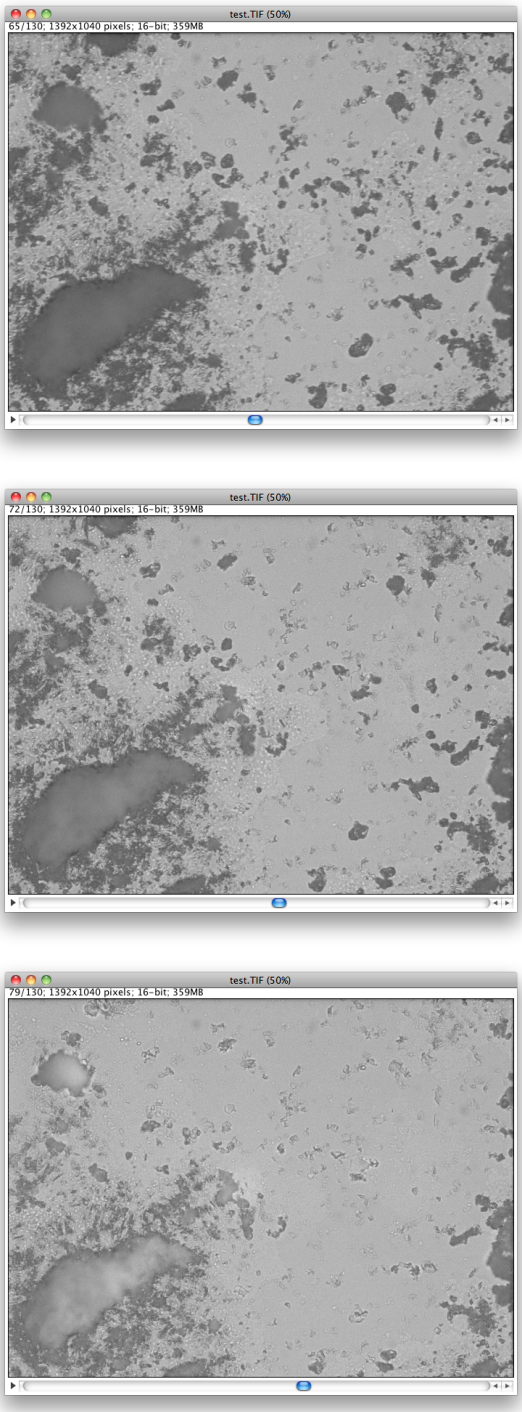

Figure 3.30: Evaporating dry water made at 19,500 RPM at 10x magnification, top at 0.0 s, middle at 0.7 s, bottom at 1.4 s.

Table 3.4: Conversion factors from pixels to micrometers

Magnification	µm/pixel
4x	1.613
10x	0.645
20x	0.322
40x	0.161

$$A_{part,\mu m} = A_{part,pixels} C^2 \tag{3.5}$$

where $A_{part,pixels}$ is the particle area measured from ImageJ and C is the conversion factor from Table 3.4. To solve for the equivalent diameter, the following equation was used

$$d_{equiv} = [(4/\pi) A_{part,\mu m}]^{1/2} \tag{3.6}$$

where $A_{part,\mu m}$ is the area of the particle found using equation 3.5. The programming language Python was used to reduce the data taken from ImageJ and histograms of the particle sizes were constructed. The data was divided into 75 equally spaced bins of range 0 to 300 µm and the particle size distributions for 12,500, 14,500, 16,300, 18,000, and 19,500 RPM are shown in Table 3.5. The particle size distribution of the silica agglomerates shown in Figure 3.27 are shown in Figure 3.31. The mode of the histograms are presented in Table 3.6. At 12,500 RPM, the dry water particle size mode is between 32 µm (deionized) and 48 µm (tap). At 19,500 RPM the modes for deionized and tap water are 28 µm and and 20 µm respectively. The mode of the silica agglomerates was found to be around 12 µm. Carter et al. reported particle sizes at 50 µm for blender rotational speeds at 19,000 RPM and also reported particles

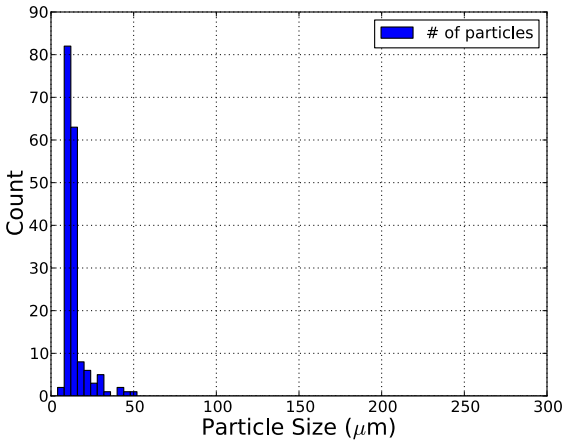

Figure 3.31: Particle size distribution of silica agglomerates

ranging in size from 25 µm to 50 µm depending on blender speed [18,44]. Forny et al. used laser diffraction to find particle size distributions with mean particle diameters on the order of 112 µm [17].

3.5 Conclusions

Dry water was produced in a batch process to be evaluated as a new fire suppressant. It was found that at low normal and shear stresses, the dry water encapsulations will separate and release the water held inside. Several delivery strategies were built and tested and a possible low shear delivery mechanism was discussed that avoids the ratholing effect. Development of a continuous dry water production system was also discussed. Filter loading tests were also conducted to determine the properties of the dry water collected from the batch and continuous cases. It was observed that the quality (the ratio of water to silica) for the continuous case reaches the batch value and is similar to results found in the literature. For the batch dry water, it was also observed that the particle size of the dried dry water encapsulations

do vary with rotational speed of the blender and is largely independent of the type of water used (tap or deionized).

Table 3.5: Dry water particle size distributions for deionized and tap water

Motor speed (RPM)	Deionized Water	Tap Water
12,500	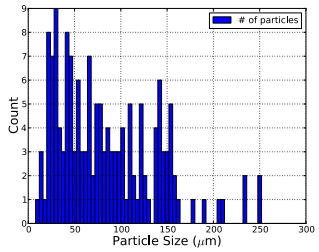	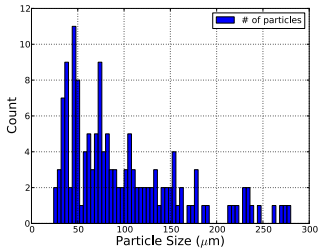
14,500	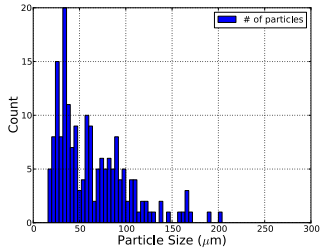	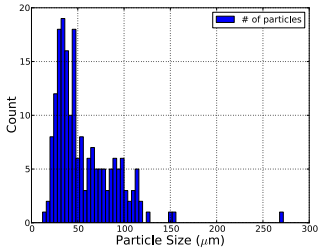
16,300	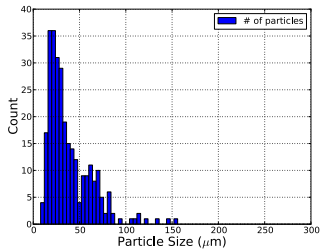	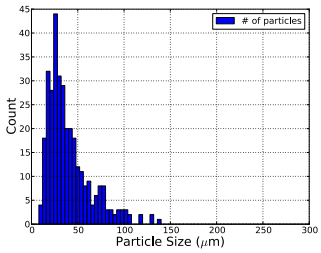
18,000	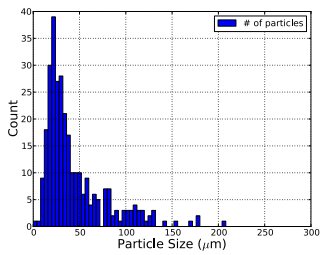	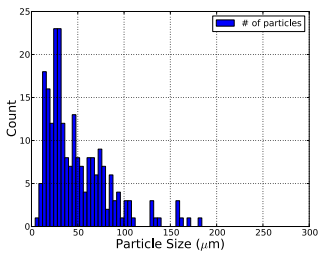
19,500	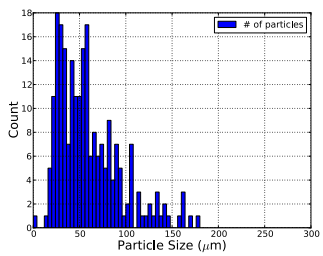	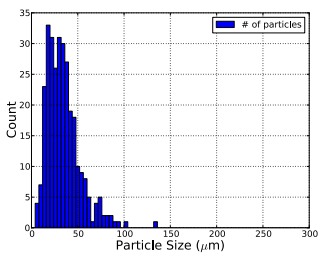

Table 3.6: Modes of the particle size distributions for deionized and tap water

Rotational Speed (RPM)	Deionized Water Mode (µm)	Tap Water Mode (µm)
12,500	32	48
14,500	36	36
16,300	20	28
18,000	24	28
19,500	28	20

Chapter 4

Conclusion and Future Work

The detailed results of 10 Fire Foe^{TM} activation tests were presented including gas phase temperatures, Fire Foe^{TM} wall temperatures for seven of the ten tests, and activation times for the fire suppression systems. Experimental and computational gas and Fire Foe^{TM} tube wall temperatures were compared to each other. The FDS results were then used to find the heat flux on a virtual Fire Foe^{TM} tube. This heat flux was then passed to a thermo-physical semi-empirical numerical model to predict activation times which were compared to experimental activation times. Overall, the measured temperatures within the glovebox showed more stratification in experimentation than the FDS predicted temperatures and Fire Foe^{TM} temperatures were generally being underpredicted. At higher heat release rates, shorter activation times, the sub-model tended to overpredict activation time, at lower heat release rates, longer activation times, the model tended to underpredict activation times, and the model tends to overpredict activation time overall. It was seen that the numerical model does not completely capture the behavior of observed activation times. For this reason, a Bayesian parameter inference was run on the sub-model. While the Bayesian inference approach is able to match sub-model temperatures to experimental temperatures, some non-physical results occurred at the lower HRR fires. Hypalon® glove material degradation tests were also conducted. The heat of combustion of the glove material matched well with what was observed in the literature. While thin ignition behavior of the material was expected, due to the experimental setup, thick ignition behavior

of the glove material was observed.

The development of a dry water delivery mechanism and a continuous dry water production apparatus was discussed. It was found that at low shear stresses, the dry water will release the water held inside which leads to the formation of liquid marbles. Serveral delivering strategies were built and tested, and a possible low shear delivery mechanism was discussed that avoids the ratholing effect. Future work for the suppression system involves accurately characterizing the flow of the dry water from the nozzle and to compare the suppression capabilities to similar water mist systems. For the continuous system, components were characterized such that dry water could be made with the same ratio of water to silica. Filter loading tests were also conducted to determine the quality of the dry water collected from the batch and continuous cases. It was observed that the the ratio of water to silica for the continuous case reaches the batch value. For the batch dry water, it was also observed that the particle size of the dried dry water silica encapsulations does vary with rotational speed of the blender and is largely independent of the type of water used (tap or deionized). Future work for the development of a continuous dry water production apparatus includes optimizing the system by reducing pressure losses in the system. Next steps may also include developing a control system to more accurately control the introduction of fumed silica and water into the mixing chamber.

Appendix A

Scoping Water Mist Tests

A.1 Water Mist

Water mist experiments were done using the experimental setup shown in Figure A.1. A small scale burn box was constructed out of fire resistant gypsum board of thickness 1.7 cm with inside dimensions 42.4 cm by 20.1 cm by 50.8 cm. A hole was made at the top of the burn box to allow a water misting nozzle to supply a fine mist to a heptane pool fire with a diameter of 7 cm. A square opening of 30 cm by 30 cm had been made in the front of the burn box initially for an earlier experiment. Thermocouples were spaced at 5 cm intervals and centered over the pool fire with the bottom-most thermocouple being 1.5 cm above the box floor. Lab air was used to pressurize a titanium pressure vessel partially filled with water. An SMC AR 20-N01E-Z pressure regulator was used to dial in the pressure for the water mist system. Water from the pressure vessel flowed through a Keys Instrument flowmeter, a USC pressure gauge with range 0-700 kPa (0-100 psi), and a misting nozzle of 0.254 mm orifice diameter at pressures of 480, 550, 620, and 700 kPa (70, 80, 90, and 100 psi).

To characterize the size of the fire to be suppressed, the burning rate without suppression of 6 g of heptane in the 7 cm diameter fuel pan was measured using a Denver Instruments TP-323 balance, shown in Figure A.2. The average burning rate was found to be around 0.103 g/s. With a heat of combustion for heptane of 44 kJ/g, the heat release rate of the fire was calculated to be approximately 4.5 kW.

For the experiments, the pressure vessel was first pressurized to the desired

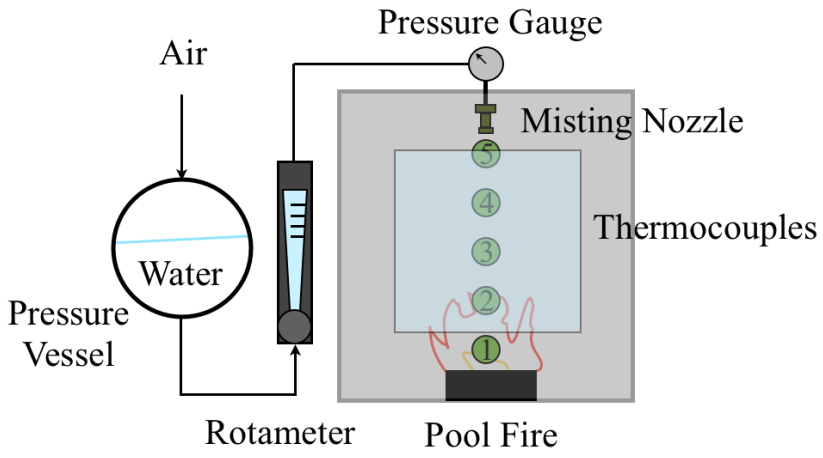

Figure A.1: Water mist setup

pressure. 6 g of heptane was poured in the pan and placed inside of the burn box. A National Instruments SCC 68 data acquisition system was used to take temperature measurements sampling at 10 Hz. The data acquisition system was started and 5 s of pretest was taken before the pool fire was ignited. The glass pane was quickly placed over the large opening in the front of the box and the fire was allowed to burn for a total of 60 s after ignition. At this point, a valve was used to allow high pressure flow of water at 0.8 g/s into the burn box. A total of 100 s worth of temperature data were taken for each test. Figure A.3 shows temperatures of the five thermocouples for a single test at 100 psi.

An average fire size of 4 MW requires that 4.7 kg/s of water mist be applied to suppress the fire [45]. Scaling down to the fire size of 4.5 kW, roughly 5 g/s of water would be needed to suppress the fire. It was shown through experimentation that a flow rate of 0.8 g/s was sufficient to extinguish an 4.5 kW fire. To see if the experimentation was close to other authors experimental conditions the Spray Heat Absorption Coefficient (SHAR) was used. The SHAR is defined as

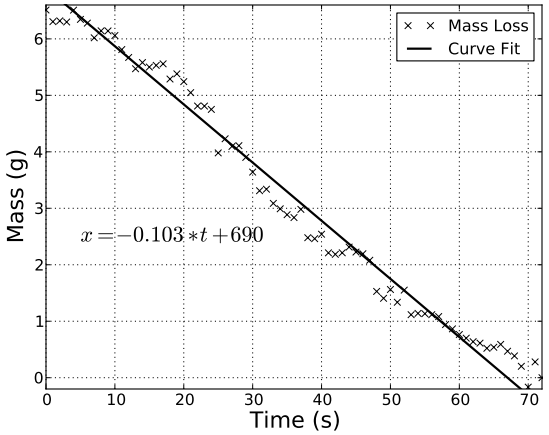

Figure A.2: Mass loss of 6 g of 7 cm diameter heptane pool fire burning freely

$$SHAR = \frac{Q_{water}}{Q_{fire}} \tag{A.1}$$

where Q_{water} is the heat absorbed by the water and Q_{fire} is the heat released by the fire. Under optimum conditions for an unconfined flame, the SHAR can be as low as 0.3. For real fire scenariou, however, the SHAR will be approximately 0.6 [46]. For a SHAR of 0.6 and a fire size of 4.5 kW, the necessary water application rate should be 1.2 g/s for a real fire scenario. With a SHAR of 0.3, the necessary water application rate of 0.6 g/s approaches that actually used in experimentation. It should be noted that the SHAR does not take into compartmental effects such as oxygen displacement due to the evaporation water [13].

Water mist tests were initially conducted as a basis for comparison of the suppression potential of dry water flowed at similar flow rates and spread patterns. The dry water could not be flowed easily to make a simple comparison to water mist systems. Attempts to flow premade dry water resulted in water release.

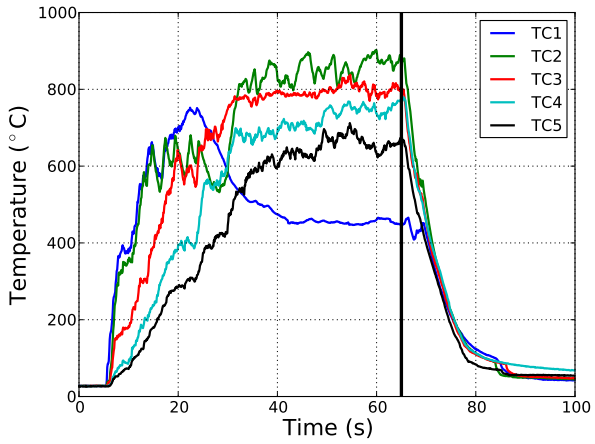

Figure A.3: Water mist experimental temperatures for 100 psi pressure. Vertical line indicates activation of water mist

Bibliography

[1] J. Quintiere, *Fundamentals of Fire Phenomena*. John Wiley, 2006.

[2] B. Wang, D. Xu, K. W. Chu, and A. B. Yu, "Numerical study of gas-solid flow in a cyclone separator," *Applied Mathematical Modeling*, pp. 1326–1342, April 2006.

[3] P. H. Thomas, "Fires and flashover in rooms - a simplified theory," *Fire Safety Journal*, vol. 3, pp. 67–76, 1980.

[4] P. H. Thomas, "Behavior of fires in enclosures - some recent progress," in *Fourteenth Symposium (International) on Combustion*, vol. 14, pp. 1007–1020, 1973.

[5] M. L. Bullen and P. H. Thomas, "Compartment fires with non-cellulosic fuels," in *Colloquium on fire and explosion*, pp. 1139–1147, Fire Research Station, 1979.

[6] "Nfpa 10 standard for portable fire extinguishers," tech. rep., National Fire Protection Association, 2012.

[7] D. Drysdale, *SFPE Handbook of Fire Protection Engineering*, ch. Thermochemistry. Quincy, Massachusetts: National Fire Protection Association, 4th ed., 2008.

[8] "The montreal protocol on substances that deplete the ozone." Final Act, 1984.

[9] "Nfpa 750 standard on water mist fire protection systems," tech. rep., National Fire Protection Association, 2000.

[10] J. R. Mawhinney, B. Z. Dlugogorski, and A. K. Kim, "A closer look at the extinguishing properties of water mist," Proceedings: International Association for Fire Safety Science Conference, 1994.

[11] T. S. Ravigururajan and M. R. Beltran, "A model for attenuation of fire radiation through water droplets," *Fire Safety Journal*, vol. 15, pp. 171–181, February 1989.

[12] A. Coppalle, "Fire protection: Water curtains," *Fire Safety Journal*, vol. 20, pp. 241–255, 1993.

[13] Z. Liu and A. K. Kim, "A review of water mist fire suppression systems - fundamental studies," *Journal of Fire Protection Engineering*, vol. 10, no. 3, pp. 32–50, 2000.

[14] K. Adiga, R. F. H. Jr, R. S. Sheinson, F. W. Williams, and S. Ayers, "A computational and experimental study of ultra fine water mist as a total flooding agent," *Fire Safety Journal*, vol. 42, pp. 150–160, 2007.

[15] M. V. Gross, L. T. Weinman, and B. G. V. Stratum, "Portable fire extinguishing apparatus and method." United States Patent, November 2010.

[16] B. D. Allan, "Dry water." United States Patent, 1977.

[17] L. Forny, I. Pezron, K. Saleh, P. Guigon, and L. Komunjer, "Storing water in powder form by self-assembling hydrophobic silica nanoparticles," *Powder Technology*, vol. 171, pp. 15–24, 2006.

[18] B. O. Carter, W. Wang, D. J. Adams, and A. I. Cooper, "Gas storage in "dry water" and "dry gel" clathrates," *Langmuir*, pp. 3186–3193, 2010.

[19] B. P. Binks and R. Murakami, "Phase inversion of particle-stabilized materials from foams to dry water," *Nature Materials*, vol. 6, pp. 865–869, 2006.

[20] O. Taylan and H. Berberoglu, "Thermal radiation transport in a cloud of dry water particles," in *Proceedings of the ASME 2012 Summer Heat Transfer Conference*, American Society of Mechanical Engineers, July 2012.

[21] C. Bartlett, "The glovebox evolution," *Enclosure*, vol. 21, no. 1, pp. 16–22, 2008.

[22] A. Hammami, N. Raymond, and M. Armand, "Lithium-ion batteries: runaway risk of forming toxic compounds," *Nature*, vol. 424, pp. 635–636, August 2003.

[23] M. B. Biles, "Glovebox fire safety: a guide for safe practices in design, protection, and operation," tech. rep., Factory Mutual, 1967.

[24] J. V. Panesko, "Mobility of plutonium compounds in simulated fire sprinkler spray," *Health and Safety*, October 1972.

[25] A. J. Hill, "Automatic fire extinguishing systems for glove boxes and shielded cells at the savannah river laboratory," June 1971.

[26] R. Banks, "Environmental aspects of fluorinated materials: Part 2. 'in kind' replacements for halon fire extinguishants; some recent candidates," *Fluorine Chemistry*, vol. 67, pp. 193–203, February 1994.

[27] W. Chow, E. Lee, F. Chau, and J. Dyke, "The necessity of studying chemical reactions on the clean agent heptaflouropropane in fire extinguishment," *Architectural Science Review*, vol. 47, pp. 223–228, 2004.

[28] M. W. Burkett, R. A. Martin, D. L. Fenton, and M. V. Gunaji, "Fire simulation in nuclear facilities, the firac code and supporting experiments," 18th DOE

Nuclear Airborne Waste Management and Air Cleaning Conference, (Baltimore, MD), August 1984.

[29] M. Rosenberger and J. Tsiagkouris, "Glovebox Fire Suppression - Fire Foe^{TM} Tubes."

[30] "Nuclear power plant fire modeling analysis guidlines," Tech. Rep. NUREG-1934, United States Nuclear Regulatory Commissison, November 2012.

[31] B. R. Kobe, D. I. Pineda, R. D. Purvis, and B. W. Stockberger, "Design and fabrication of a radiant heating and ignition apparatus for fire testing," tech. rep., The University of Texas at Austin, May 2012.

[32] K. McGrattan, S. Hostikka, J. Floyd, H. Baum, R. Rehm, W. Mell, and R. McDermott, "Fire Dynamics Simulator (Version 6) Technical Reference Guide," tech. rep., National Institute of Standards and Technology, 2012.

[33] K. McGrattan, R. McDermott, S. Hostikka, and J. Floyd, "Fire Dynamics Simulator (Version 6) User's Guide," tech. rep., National Institute of Standards and Technology, 2012.

[34] J. Wang, J. K. Carson, M. F. North, and D. J. Cleland, "A new approach to modelling the effective thermal conductivity of heterogeneous materials," *International Journal of Heat and Mass Transfer*, pp. 3075–3083, April 2006.

[35] "Dupont fe-36 fire extinguishing agent," 2007.

[36] M. Kohan, *Nylon Plastics Handbook*. Hanser Gardner Publications, 1995.

[37] K. J. Overholt, *Forward and Inverse Modeling of Fire Physics Towards Fire Scene Reconstruction*. PhD thesis, The University of Texas at Austin, May 2013.

[38] R. E. Lyon, "Heat release kinetics," *Fire and Materials*, vol. 24, pp. 179–186, April 2000.

[39] American Society for Testing and Materials, West Conshohocken, Pennsylvania, *ASTM E 1354-04a, Standard Test Method for Heat and Visible Smoke Release Rates for Materials and Products Using an Oxygen Combustion Calorimeter*, 2007.

[40] T. S. Lin, J. M. Cogen, and R. E. Lyon, "Correlations between microscale combustion calorimetry and conventional flammability tests for flame retardant wire and cable compounds," *International Wire & Cable Symposium*, 2007.

[41] R. Alpert, *SFPE Handbook of Fire Protection Engineering*, ch. Ceiling Jet Flows. Quincy, Massachusetts: National Fire Protection Association, 3rd ed., 2003.

[42] J. Besag, "Markov chain monte carlo for statistical inference." No. 9, April 2001.

[43] W. L. Snyder, "Separator." Patent: 960,725, June 1910.

[44] B. O. Carter, J. V. M. Weaver, W. Wang, D. G. Spiller, D. J. Adams, and A. I. Cooper, "Microencapsulation using an oil-in-water-in-air 'dry water emulsion'," *The Royal Society of Chemistry*, pp. 8253–8255, 2011.

[45] G. G. B. III, C. L. Beyler, and R. Hansen, "A quasi-steady-state model for predicting fire suppression in spaces protected by water mist systems," *Fire Safety Journal*, pp. 327–362, June 2000.

[46] R. Wighus, "Extinguishment of enclosed gas fires with water spray," tech. rep., SINTEF Norwegian Fire Research Laboratory, 1990.

Vita

Jan-Michael Cabrera was born in August of 1988 in Landstuhl, Germany. Thanks to his father's military service, Jan-Michael had the chance to experience growing up in El Paso, Texas, Bamburg, Germany, Watertown, New York, Rio Grande, Puerto Rico, and Schertz, Texas. He entered high school in 2002 at Roosevelt Roads Middle/High school in Puerto Rico and later moved to Schertz, Texas in 2003 where he graduated from Samuel Clemens High School in 2006. Jan-Michael received his B.S. in Mechanical Engineering in May of 2011 and his M.S in Mechanical Engineering Thermal/Fluid Systems in December of 2013 from The University of Texas at Austin.

Permanent contact information: janmichael.cabrera@gmail.com

This thesis was typed by Jan-Michael Cabrera-O'fray.